

Electronic Thesis and Dissertation Repository

12-15-2020 2:00 PM

Geo-structural Analysis of Integral Abutment Bridges

Biyi Li, *The University of Western Ontario*

Supervisor: Bartlett, Michael F., *The University of Western Ontario*

Co-Supervisor: Newson, Timothy, *The University of Western Ontario*

A thesis submitted in partial fulfillment of the requirements for the Master of Engineering Science degree in Civil and Environmental Engineering

© Biyi Li 2020

Follow this and additional works at: <https://ir.lib.uwo.ca/etd>



Part of the [Civil Engineering Commons](#), [Geotechnical Engineering Commons](#), and the [Structural Engineering Commons](#)

Recommended Citation

Li, Biyi, "Geo-structural Analysis of Integral Abutment Bridges" (2020). *Electronic Thesis and Dissertation Repository*. 7540.

<https://ir.lib.uwo.ca/etd/7540>

This Dissertation/Thesis is brought to you for free and open access by Scholarship@Western. It has been accepted for inclusion in Electronic Thesis and Dissertation Repository by an authorized administrator of Scholarship@Western. For more information, please contact wlsadmin@uwo.ca.

Abstract

Integral abutment bridges are jointless bridges where bridge decks and girders are integrated with abutments. The longitudinal displacements and rotations of the bridge are partially accommodated by the soil-pile system wherein the soil surrounding the piles generates active and reactive lateral forces when the piles deflect due to the movement of the superstructure. Since the soil stress-strain responses are inherently nonlinear, the pile deflection and the soil stiffness are interdependent. Consequently, evaluating soil-pile interactions requires a detailed geo-structural analysis. There are two common approaches used to idealize the soil-pile interactions for laterally loaded piles: the p-y and continuum mechanics approaches

This thesis first presents a critical review of the literature concerning integral abutment bridges and soil-pile interaction idealizations. Deformations of a specific free-ended single pile subjected to either a lateral force or moment at the pile head are idealized using the p-y and continuum mechanics approaches. Deformations and restraint force effects of a specific integral abutment subjected to thermally induced deformations or truck load is simulated with a 2-D finite element analysis with soil-pile interaction idealized using the two approaches. For both loading cases, influences of the two idealizations are compared and critically evaluated. A parametric study is conducted to investigate how the soil-pile interactions affect the response of bridges with various geometries, stiffnesses, and soil parameters. Further, this research presents a simplified model of an integral abutment and mechanics-based equations to quantify the deformations and restraint-induced load effects at the pile head and the end of the superstructure.

Keywords: Continuum mechanics approach; Integral abutment bridges; Laterally loaded piles; LPILE; P-y approach; Soil-pile interactions.

Summary for Lay Audience

Bridges expand and contract as temperature rises and drops. Conventionally these movements are accommodated by expansion joints at the end of the deck that are highly susceptible to corrosion and deterioration. To reduce or eliminate costly maintenance and expansion joint replacement costs, integral abutment designs have been developed to eliminate the expansion joints. As the deck of an integral abutment bridge expands or contracts, the bridge superstructure forces the foundations to move against the ground behind the abutments. It is challenging to create analytical models that accurately quantify the structural actions in the foundations and superstructure that are generated by restraint of this movement. The research reported in this thesis derives equations to predict the response of the integral abutment, and compares results obtained using two commonly adopted procedures for modelling the soil-structure interaction.

Acknowledgments

First and foremost, I would like to express my deepest appreciation to my advisors, Dr. F. Michael Bartlett and Dr. Timothy Newson. Their assistance and guidance sharpened my thinking and brought this research to a higher level and their unwavering enthusiasm for the structural and geotechnical engineering makes this journey enjoyable. Truly, it has been my privilege to have worked with them in the past two years.

I would also like to thank Dr. M. Hesham El Neggar for providing access to the LPILE analysis software which contributed a major part to this study.

Lastly, my deep gratitude goes to my parents, Liqun and Yiran, my boyfriend, Yifan, and my friends, Bo, Amer, Murad, Itzel, and M. Alwalan for their enduring and unconditional encouragement, love, support, and smiles. It has been a tough year for most of us to adapt our lives to deal with changes the pandemic is having on our works and homes. Even though we do not get to see each other often, every phone call and message we had constantly reminded me that I was not alone on this journey. This thesis would not have been possible without them.

Table of Contents

Abstract	ii
Summary for Lay Audience	iii
Acknowledgments	iv
Table of Contents	v
List of Tables	viii
List of Figures	xi
List of Appendices	xiii
Nomenclature	xv
Chapter 1	1
1 Introduction	1
1.1 Research Background	1
1.2 Objectives	3
1.3 Thesis Overview	4
Chapter 2	6
2 Literature Review.....	6
2.1 General Behavior of Integral Abutment Bridges	6
2.1.1 Introduction.....	6
2.1.2 Construction Sequence.....	8
2.1.3 Loads.....	10
2.2 Previous Studies of Integral Abutment Bridges.....	15
2.2.1 Introduction.....	15
2.2.2 Field Studies.....	15
2.2.3 Numerical Parametric Studies.....	19
2.3 Soil-Pile Interaction Idealizations.....	22
2.3.1 P-y Approach	22
2.3.2 Continuum Mechanics Approach	26
2.4 Application of P-y Approach in Integral Abutment Bridge Modelling.....	29
2.5 Summary and Conclusions	32
Chapter 3	35
3 Quantification of Soil-Structure Interaction in Laterally Loaded Piles	35
3.1 Objectives of Research Presented in this Chapter	35
3.2 Pile Geometry and Soil Conditions.....	36
3.3 Estimation of Soil Parameters.....	41
3.3.1 Biot's and Kishida's Relationships.....	44
3.3.2 Lashkaripour's Relationship	48

3.3.3	Input Soil Parameters for Basu Analyses.....	48
3.4	Effect of Soil Stiffness	51
3.5	Effect of Non-linear Soil Response	55
3.6	Normalized Pile Head Lateral Deflection.....	56
3.7	Summary and Conclusions	68
Chapter 4	71
4	Case Study of Integral Abutment Bridge.....	71
4.1	Objectives of Research Presented in this Chapter	71
4.2	Bridge Description	72
4.2.1	Bridge Geometry.....	73
4.2.2	Material Properties.....	75
4.3	Integrated Analytical Procedures	76
4.3.1	Iterative Procedure for SAP 2000-LPILE Analysis.....	76
4.3.2	Non-iterative Procedure for SAP 2000-Basu Analysis.....	78
4.4	Thermally Induced Deformations and Earth Pressures Analyses.....	82
4.4.1	Maximum Temperature Variations and Gradients	82
4.4.2	Earth Pressures.....	85
4.4.3	Load Combinations	86
4.4.4	Results.....	87
4.5	Truck Loading.....	95
4.5.1	Truck Tests (Lawver et al. 2000).....	95
4.5.2	Truck Loading.....	96
4.5.2	Results.....	97
4.6	Summary and Conclusions	99
Chapter 5	102
5	Parametric Study of Integral Abutment Bridges	102
5.1	Objectives of Research Presented in this Chapter	102
5.2	Mechanics-based Bridge Responses	103
5.2.1	Validation of Equations	106
5.3	Parameters Investigated in Parametric Study	108
5.4	Parametric Study Results	113
5.4.1	Effect of Bridge Length	113
5.4.2	Effect of Superstructure Stiffnesses.....	116
5.4.3	Effect of Abutment Height.....	117
5.4.4	Effect of Pile Stiffness	119
5.4.5	Effect of Pile Surface Area	121
5.4.6	Effect of Soil Conditions	123
5.4.7	Effect of Pile Sleeve Presence and Infill Soil State	124
5.5	Summary and Conclusions	126

Chapter 6	129
6 Research Summary, Limitations, Conclusions, and Future Work	129
6.1 Summary	129
6.2 Limitations and Assumptions	130
6.3 Conclusions	131
6.4 Recommendations for Future Work	134
References	136
Appendix A: API Relationship	144
Appendix B: Maximum Pile Head Lateral Deflection Calculation	145
Appendix C: Member Sizes	146
Appendix D: Calculation of Equivalent Loads of Temperature Gradient	147
Appendix E: Calculation of Earth Pressures	150
Appendix F: Sample Calculation of the Moments at Pile Head	154
Appendix G: An Illustration of Instrumentations of Bridge #55555	155
Appendix H: Bending Moment Diagrams of a Pile as Bridge Expands and Contracts	157
Appendix I: Validation of Equations 5-1 to 5-9b	158
Appendix J: Maximum Stresses at Pile Head	160
Appendix K: Soil Properties and Young's Moduli for Cases 8 and 9	161
Appendix L: Consideration of the Water Table	162
Appendix M: Soil Properties and Young's Moduli for Cases 10 and 11	165
Curriculum Vitae	166

List of Tables

Table 2-1: Deformations of a Multi-span Integral Abutment Bridge and Bending Moment Diagrams for a Continuous Bridge Deck.....	10
Table 2-2: Summary of Previous Field Studies	17
Table 2-3: Effects of Integral Abutment Bridge Design Configurations.....	20
Table 3-1(a): Pile Dimensions and Properties Adopted in Bridge #55555 and LPILE Analyses.....	37
Table 3-1(b):Equivalent Pile Dimensions and Properties Adopted in Basu Analyses	37
Table 3-2(a): Measured Soil Strengths and Properties for Bridge #55555 (after Huang et al. 2004)	39
Table 3-2(b): Soil Properties Adopted for Bridge #55555	41
Table 3-3: Typical Values of Poisson’s Ratio (Ameratunga et al. 2016).....	44
Table 3-4: Typical Values of E_{su} for Clays (Ameratunga et al. 2016).....	47
Table 3-5: Estimated Soil Poisson’s Ratios and Young’s moduli Based on Measured Soil Properties and Strengths	50
Table 3-6: ΔG_{seq-2}^* for Analyses based on B-, K-, and L-Relationships	64
Table 3-7:Regression Coefficients for Applied Lateral Force.....	66
Table 3-8: Regression Coefficients (F=0, M=40 kN.m).....	68
Table 4-1: Material Properties for the SAP 2000 Models (Huang et al. 2004)	75
Table 4-2: Displacement at the End of the Superstructure	88
Table 4-3: Bending Moments per Bridge at the End and Mid-point of the Exterior Spans	88
Table 4-4(a): Deformations and Forces at the Pile Head for Bridge Expansion	89
Table 4-4(b): Deformations and Forces at the Pile Head for Bridge Contraction	89
Table 4-5: Measured and Computed Moments for Interior Girder of Exterior Span	98
Table 5-1(a): Deformations at the Pile Head and the the End of the Superstructure for Case 1 (Fully Rigid Abutment).....	107
Table 5-1(b): Load Effects at the Pile Head and the End of the Superstructure for Case 1 (Fully Rigid Abutment).....	107
Table 5-2(a): Deformations at the Pile Head and the End of the Superstructure for Case 1 (Partially Rigid Abutment)	107
Table 5-2(b): Load Effects at the Pile Head and the End of the Superstructure for Case 1 (Partially Rigid Abutment)	108
Table 5-3: Variables and Cases for the Parametric Study	109

Table 5-4(a): Displacements at the Pile Head and the End of the Superstructure Obtained from SAP 2000 Analyses for Cases 1 and 2.....	113
Table 5-4(b): Rotations at the Pile Head and the End of the Superstructure Obtained from SAP 2000 Analyses for Cases 1 and 2.....	114
Table 5-5(a): Moments and Shear Forces at the Head of Each Pile Obtained from SAP 2000 for Cases 1 and 2.....	114
Table 5-5(b): Moments and Axial Force at the End of the Superstructure Obtained from SAP 2000 for Cases 1 and 2	114
Table 5-6: Maximum Pile Compressive Stresses at the Pile Head for Cases 1 and 2	116
Table 5-7(a): Displacements at the Pile Head and at the End of the Superstructure Obtained from SAP 2000 Analyses for Cases 1 and 3	116
Table 5-7(b): Rotations at the Pile Head and at the End of the Superstructure Obtained from SAP 2000 Analyses for Cases 1 and 3	116
Table 5-8(a): Moments and Shear Forces at the Head of Each Pile Obtained from SAP 2000 Analyses for Cases 1 and 3	117
Table 5-8(b): Moments and Axial Force at the End of the Superstructure Obtained from SAP 2000 Analyses for Cases 1 and 3.....	117
Table 5-9: Moments and Shear Forces at the Head of Each Pile Obtained from SAP 2000 Analyses for Cases 1, 4, and 5	118
Table 5-10: Moments and Axial Forces at the End of the Superstructure Obtained from SAP 2000 Analyses for Cases 1, 4, and 5.....	119
Table 5-11: Computed Moments at the End of the Superstructure Based on Results Obtained from SAP 2000 for Case 1, 4, and 5.....	119
Table 5-12(a): Displacements at the Pile Head and the End of the Superstructure Obtained from SAP 2000 Analyses for Cases 1 and 6	120
Table 5-12(b): Rotations at the Pile Head and the End of the Superstructure Obtained from SAP 2000 Analyses for Cases 1 and 6.....	120
Table 5-13(a): Moments and Shear Forces at the Head of Each Pile Obtained from SAP 2000 Analyses for Cases 1 and 6	121
Table 5-13(b): Moments and Axial Forces at the End of the Superstructure Obtained from SAP 2000 Analyses for Cases 1 and 6.....	121
Table 5-14(a): Displacements at the Pile Head and at the End of the Superstructure Obtained from SAP 2000 Analyses for Cases 6 and 7	121
Table 5-14(b): Rotations at the Pile Head and at the End of the Superstructure Obtained from SAP 2000 Analyses for Cases 6 and 7.....	122
Table 5-15(a): Total Moments and Shears of Piles from SAP 2000 for Cases 6 and 7...122	
Table 5-15(b): Moments and Axial at the End of the Superstructure from SAP 2000 for Cases 6 and 7	122
Table 5-16(a): Displacements at the Pile Head and at the End of the Superstructure Obtained from SAP 2000 Analyses for Cases 1, 8, and 9	123

Table 5-16(b): Rotations at the Pile Head and at the End of the Superstructure Obtained from SAP 2000 Analyses for Cases 1, 8, and 9	123
Table 5-17(a): Moments and Shear Forces at the Head of Each Pile Obtained from SAP 2000 Analyses for Cases 1, 8, and 9	124
Table 5-17(b): Moments and Axial Forces at the End of the Superstructure Obtained from SAP 2000 Analyses for Cases 1, 8, and 9	124
Table 5-18(a): Displacements at the Pile Head and at the End of the Superstructure Obtained from SAP 2000 Analyses for Cases 1, 10, and 11	125
Table 5-18(b): Rotations at the Pile Head and at the End of the Superstructure Obtained from SAP 2000 Analyses for Cases 1, 10, and 11	125
Table 5-19(a): Moments and Shear Forces at the Head of Each Pile Obtained from SAP 2000 for Cases 1, 10, and 11	125
Table 5-19(b): Moments and Axial Forces at the End of the Superstructure Obtained from SAP 2000 for Cases 1, 10, and 11	126

List of Figures

Figures 2-1: Conventional Bridge and Integral Abutment Bridge Structural Systems	6
Figure 2-2: Semi-integral Abutment Bridge Structural System	8
Figure 2-3: Typical Construction Sequence of Integral Abutment Bridges	9
Figure 2-4: Simplified Passive and Active Earth Pressure Distribution (after Burke 1993)	14
Figure 2-5: Illustration of Reduction of Pile Curvature due to Abutment Rotation (after Huang et al. 2004).....	21
Figures 2-6: Typical Soil-Pile Interaction Idealization Using the P-y Approach.....	23
Figure 2-7: Reese P-y Curve for Sand (after Reese et al. 1974).....	24
Figure 2-8: Comparison of Pile Resistance (p) and Normalized Pile Deflection y/D (D is the Pile Diameter) Curves Obtained from Experimental Tests and the Empirical Curves (Kim et al. 2004).....	25
Figure 2-9: Illustration of the Two Sources of Soil Stiffnesses: Soil Compressive Stiffness and Shear Stiffness (Basu et al. 2009)	26
Figure 2-10: 3D model for North Abutment and H-Piles (Faraji et al. 2001)	30
Figure 2-11: Numerical Model for Integral Abutment Study (Dicleli and Albhaisi 2003)	31
Figures 3-1: Actual and Idealized Soil Strata for Bridge #55555.....	39
Figures 3-2: Procedure for Estimating Input Soil Parameters	42
Figure 3-3: Soil-Pile Interaction Idealizations	45
Figure 3-4: Pile Lateral Deflection Profiles (F=40 kN, M=0)	52
Figure 3-5: Pile Lateral Deflection Profiles (F=0 kN, M=40 kN.m)	54
Figure 3-6: Variation of Pile Head Deflection with Lateral Force	56
Figure 3-7(a): Variation of Normalized Pile Lateral Head Deflection with Pile-Soil Stiffness Ratio for Pile Subjected to Lateral Force.....	60
Figure 3-7(b): Variation of Normalized Pile Lateral Head Deflection with Pile-Soil Stiffness Ratio for Pile Subjected to Moment.....	60
Figure 3-8(a): Curve Fitting for B-Relationship.....	62
Figure 3-8(b): Curve Fitting for K-Relationship	62
Figure 3-8(c): Curve Fitting for L-Relationship	63
Figure 3-9: Variation of Normalized Lateral Deflection of Pile Head with Pile-Soil Stiffness Ratio for Lateral Force ($L_p/r_{eq}=271$)	64
Figure 3-10: Variation of Normalized Lateral Deflection of Pile Head with Pile-Soil Stiffness Ratio for Applied Lateral Force ($L_p/r_{eq}=80$)	65
Figure 3-11: Normalized Pile Head Lateral Deflection versus Pile-Soil Stiffness Ratios for Moment ($L_p/r_{eq}=80$).....	67

Figure 4-1: Bridge #55555 Elevation (after Huang et al. 2004)	73
Figure 4-2: Cross-section of Superstructure (after Huang et al. 2004).....	74
Figure 4-3: Pier Connection Detail (after Huang et al. 2004).....	74
Figure 4-4: Abutment and Pile Details (after Huang et al. 2004).....	75
Figure 4-5: Integrated Analytical Procedure of SAP-LP Analyses	77
Figure 4-6: SAP 2000 Models in SAP-LP Analyses	78
Figure 4-7: Soil-pile Interaction Modelling in SAP-B Analyses.....	79
Figure 4-8: Integrated Analytical Procedure of SAP-B Analyses	81
Figure 4-9: SAP 2000 Models in SAP-B Analyses	81
Figures 4-10: Measured Positive Temperature Gradient (after Huang et al. 2004).....	82
Figure 4-11: Idealization of Positive Temperature Gradient in SAP 2000 Models.....	84
Figure 4-12: Earth Pressures in SAP 2000 Model Used with LPILE.....	86
Figure 4-13: Sign Convention.....	87
Figure 4-14: Calculation of Shear and Moment at Pile Head	91
Figure 4-15: Pile Curvatures (Huang et al. 2011).....	93
Figure 4-16: Truck Positions (after Lawver et al. 2000)	96
Figure 4-17: MnDOT Sand Truck (after Huang et al. 2004).....	97
Figure 5-1: Simplified Integral Abutment	103
Figure 5-2: Deformations and Free Body Diagram of the Simplified Model.....	105
Figure 5-3: Illustration of Piles in Cases 6 and 7	105
Figure 5-4: Lateral Deflection of Abutment and Pile	105

List of Appendices

Appendix A: API Relationship	144
Figure A-1: API Relationship (API 2010)	144
Appendix B: Maximum Pile Head Lateral Deflection Calculation	145
Figure A-2: Measured Superstructure Strains (Huang et al. 2011)	145
Appendix C: Member Sizes	146
Table A-1: Sizes of Structural Components in Bridge #55555	146
Appendix D: Calculation of Equivalent Loads of Temperature Gradient	147
Figure A-3: (a) Partial Cross-Section of Bridge Superstructure; (b) Positive Temperature Gradient and Equivalent Forces	147
Table A-2: Calculations of F_i for Segment i	148
Table A-3: Calculations of M_i for Segment i	149
Appendix E: Calculation of Earth Pressures	150
Figure A-4: Lateral Earth Pressure Coefficients (after CSA 2019)	151
Figure A-5: Illustration of Earth Pressure Idealization	152
Appendix F: Sample Calculation of the Moments at Pile Head	154
Appendix G: An Illustration of Instrumentations of Bridge #55555	155
Figure A-6: Locations of the instrumentation (Huang et al. 2011)	155
Figure A-7: Instrumentation Nomenclature System (Huang et al. 2011)	156
Appendix H: Bending Moment Diagrams of a Pile as Bridge Expands and Contracts	157
Figure A-8: Bending Moment Diagram of a Single Pile as Bridge Expands and Contracts	157
Appendix I: Numerical and Computed Bridge Responses	158
Table A-4(a): Comparison of Lateral Translations and Rotations for Cases 1 to 11	158

Table A-4(b): Comparison of Force Effects for Cases 1 to 11	159
Appendix J: Maximum Stresses at Pile Head	160
Table A-5: Maximum Stresses at Pile Head	160
Appendix K Soil Properties and Young's Moduli for Cases 8 and 9	161
Table A-6(a): Estimated Soil Poisson's Ratios and Young's moduli for Case 8 (Uniform Loose Sand)	161
Table A-6(b): Estimated Soil Poisson's Ratios and Young's moduli for Case 9 (Uniform Dense Sand)	161
Appendix L: Consideration of Water Table.....	162
Table A-7: Estimated Soil Poisson's Ratios and Young's moduli for Case 8b (Uniform Loose Sand with water table).....	162
Table A-8(a): Displacements at the Pile Head and the End of the Superstructure Obtained from SAP 2000 Analyses for Cases 8 and 8b	162
Table A-8(b): Rotations at the Pile Head and the End of the Superstructure Obtained from SAP 2000 Analyses for Cases 8 and 8b.....	163
Table A-9(a): Moments and Shears at the Head of Each Pile Head Obtained from SAP 2000 Analyses for Cases 8 and 8b	163
Table A-9(b): Axial Forces and Moments at the End of the Superstructure Obtained from SAP 2000 Analyses for Cases 8 and 8b.....	164
Appendix M: Soil Properties and Young's Moduli for Cases 10 and 11	165
Table A-10(a): Estimated Soil Poisson's Ratios and Young's moduli for Case 10 (Sleeve Filled with Loose Sand)	165
Table A-10(b): Estimated Soil Poisson's Ratios and Young's moduli for Case 11 (Sleeve Filled with Dense Sand).....	165

Nomenclature

A	Area of pile cross-section
A_s	Area of the superstructure cross section
A_w	Area of the web of H-pile
B	Width of the Euler-Bernoulli beam adapted in the Biot's and Vesic's Relationships
b	Width of pile cross section
b_{abut}	Width of the abutment
b_s	Width of the superstructure cross section
c_u	Soil undrained cohesion
d	Depth of pile cross section
E_b	Young's modulus of the Euler-Bernoulli beam adapted in the Biot's and Vesic's Relationships
E_c	Young's modulus of the concrete superstructure
E_p	Young's modulus of pile
E_s	Young's modulus of soil
E_{su}	Young's modulus of undrained soil
E_s'	Young's modulus of drained soil
e_a	Vertical distance from the neutral axis of the superstructure to the line of action of the active pressure resultant P'_a
e_p	Vertical distance from the neutral axis of the superstructure to the line of action of the passive pressure resultant P'_p
F	Lateral force applied at a single pile head
F_y	Yield strength
F_h	Holding force applied to the superstructure to hold the cross-section in an initial zero-strain condition

G_s	Shear modulus of soil
G_s^*	Shear modulus of soil considering the effect of Poisson's ratio
G_{seq}^*	Equivalent shear modulus for layered soil
G_{seq-2}^*	Equivalent shear modulus for layered soil with two layers
G_{seq-4}^*	Equivalent shear modulus for layered soil with four layers
H	Height of the abutment
H_s	Depth of the superstructure
h	Vertical distance from the neutral axis of the superstructure to the abutment soffit
h_1	Vertical distance from the neutral axis of the superstructure of the top of the deck
I_b	Moment of inertia of the cross-section of the Euler-Bernoulli beam adapted in the Biot's and Vesic's Relationships
I_p	Moment of inertia of the pile cross section
I_s	Moment of inertia of the superstructure
K_a	Coefficient of active earth pressure
K_G	Empirical modulus coefficient
K_p	Coefficient of passive earth pressure
K_s	Flexural stiffness of the superstructure
K_{yy}	Diagonal coefficient of soil-pile lateral stiffness
K_{zy} and K_{yz}	Off-diagonal coefficients of the soil-pile vertical and lateral responses
K_{zz}	Diagonal coefficient of soil-pile axial stiffness
$K_{z\theta}$ and $K_{\theta z}$	Off-diagonal coefficients of the soil-pile vertical and rotational responses
$K_{y\theta}$ and $K_{\theta y}$	Off-diagonal coefficients of the soil-pile lateral and rotational responses

$K_{\theta\theta}$	Diagonal coefficient of soil-pile rotational stiffness
K_0	Coefficient of earth pressure at rest
k	Subgrade reaction modulus of soil
k_s	Axial stiffness of the superstructure
$[K]$	Soil-pile stiffness matrix
L_s	Length of superstructure
L_{es}	Length of superstructure end span
L_p	Length of pile
M or M_p	Moment at the pile head
M_h	Holding moment applied to the superstructure to hold the cross-section in an initial zero-strain condition
M_i	Initial estimate of pile head moment
ΣM_p	Total pile-head moment at one abutment
M_s	Moment at the end of the superstructure
N_s	Axial force in the superstructure
p_a	Reference soil stress
P'_a	Force resultant of active earth pressure
P'_p	Force resultant of passive earth pressure
p	Soil lateral resistance force per unit length of a pile
p_{ult}	Ultimate soil resistance for the clay layer
r	Radius of circular piles
r_{eq}	Equivalent radius of non-circular piles
t_f	Thickness of pile flange
t_i	Soil thickness of Layer i

t_w	Thickness of pile web
u_y	Pile lateral displacement defined in the continuum mechanics approach
V_i	Initial estimate of pile-head shear
V_p	Shear force at the pile head
ΣV_p	Total moment at the heads of piles on each side of the bridge
y	lateral deflection of pile
y_i	Initial estimate of lateral deflection of pile head
y_M	Lateral deflection at pile head due to applied moment M_i
y_v	Lateral deflection at pile head due to applied shear V_i
z	Depth of pile
\bar{z}_t	Vertical distance from neutral axis to soffit of the superstructure
α	Coefficient of thermal expansion
γ	Soil unit weight
γ'	Effective soil unit weight
ΔT	Temperature change
Δ or Δ_p	Lateral displacement of pile head
Δ_s	Lateral displacement of end of the superstructure
Δ_{st}	Lateral displacement of end of the superstructure induced by the temperature variation and temperature gradient assuming the superstructure moves freely
ε_{50}	Soil strain factor
ε_{pq}	Strain tensor in the soil
θ	Rotation of pile head
θ_M	Rotation at the pile head due to applied moment M_i

θ_a	Rotation of abutment
θ_v	Rotation of pile head due to applied shear V_i
θ_p	Rotation of pile head
θ_s	Rotation of end of the superstructure
θ_{st}	Rotation of end of the superstructure induced by the temperature variation and temperature gradient assuming the superstructure moves freely
κ	Pile curvature
λ_s	Lame's constant for soil
ν_s'	Poisson's ratio for drained soil
Π	Potential energy of the soil-pile system
σ_{pq}	Stress tensor in the soil
ϕ_x	Dimensionless displacement function varying along the transverse direction, x
ϕ_y	Dimensionless displacement function varying along the lateral direction, y
ϕ_s	Resistance factor for steel
φ	Friction angle of soil
φ_{eq}	Equivalent friction angle of layered soil
φ_i	Friction angle for Layer i
φ'	Effective friction angle of soil

Chapter 1

1 Introduction

1.1 Research Background

Expansion joints and bearings are conventionally installed in bridges to accommodate the movement of the bridge superstructure due to thermal expansion and contraction, creep strain of concrete under sustained load and shrinkage of concrete with aging. Field investigations have indicated, however, that corrosion and deterioration cause expansion joints to perform poorly, leading to high maintenance and replacement costs. (e.g., Johnson and McAndrew 1993). Consequently, “integral abutment bridges” have been designed and constructed to eliminate these components and connect the superstructure, comprising the deck and girders, directly to the abutments. This structural system effectively reduces construction and maintenance costs (Hu and Wu 2014). Given these enormous benefits, over the years, integral abutment bridges have been extensively constructed in different countries, especially in Europe, the United States, and Canada (Huang et al. 2011).

Different structural systems have been developed for integral abutment bridges, including tall abutments on shallow foundations and short abutments on deep foundations. Semi-integral abutment bridges eliminate the expansion joints at the ends of the superstructure and partially accommodate the superstructure movements at the approach slabs and the soils behind the abutment or at a “shield” cap at the end of the girders (Card and Carder, 1993). Most of the integral abutment bridges in the United States and Canada are supported on the concrete abutments and on steel H-Piles (White 2007). Other pile types, such as prestressed concrete piles and steel pipe piles, are also occasionally used (Springman et al. 1996). Typically, the top 3 m of the pile foundations are encased by a sleeve, filled with loose sand, that is intended to allow the top of the pile to flex laterally as the abutment moves.

Although the concept of integral abutment bridges simplifies the construction and maintenance procedures, it brings complications to the structural and geotechnical analyses necessary for design. One of the biggest challenges is the idealization of the soil-pile interactions (Faraji et al. 2001). Since the connections between the bridge superstructure, abutments, and piles are rigid, superstructure movements must be accommodated by rotation and lateral deflection of the abutments and piles. Consequently, the lateral stiffness of the soil affects the magnitudes of the force effects generated in the piles and superstructure. If the movements are large, the soil response may be nonlinear, so the idealization of the soil-pile interaction usually requires an iterative analysis to determine the soil reactions and the corresponding pile deformations (Faraji et al. 2001). The design of integral abutment bridges therefore represents a complex coupled problem of indeterminate structural analysis and nonlinear geotechnical engineering.

There are two common approaches used to idealize the soil-pile interactions for laterally loaded piles: the p-y and continuum mechanics approaches. The p-y approach idealizes the interactions using a series of lateral springs distributed vertically over the depth of the pile. The spring stiffnesses are defined by p-y curves, or the relationship between the soil resistance per unit length of the pile (p) and the lateral deflection of the pile (y). In reality, this is a simplistic idealization that is really a very poor analogy to soil stress-strain responses: the idealized springs cannot be considered either "spring constants" or intrinsic properties of the soil.

The continuum mechanics approach, on the other hand, is more rational than the p-y approach because it considers the soil as a continuous medium by applying detailed mathematical calculations and finite element or finite difference analysis, that can more precisely model linear or non-linear materials. However, typical finite element analyses, such as those performed using PLAXIS (PLAXIS BV. 2013) and ABAQUS (SIMULIA 2010), normally requires considerable effort to construct the model, so they have been rarely adopted for the design purposes in the industry (Basu and Salgado 2008). Basu and Salgado (2008) developed a new framework based on the continuum mechanics approach for analyzing the responses of piles subjected to static or cyclic lateral forces. This

framework provides similar results to finite element analyses but requires less time for model construction and computations. However, this framework neglects soil plasticity, so when the soil is subjected to large deformations and rotations that induce non-linear behavior, the analysis overestimates the soil stiffness.

Extensive numerical parametric studies have been conducted by others to investigate the influence of different design variables, such as bridge length, span length, girder depth, connection fixity, soil conditions, pile orientation, pile size, and pile sleeve presence and infill soil state on the force effects generated in the superstructure, abutments, and piles by superstructure movements (e.g. Quinn and Civjan 2017; Baptiste et al. 2011; Huang, et al. 2008). These numerical studies are ineffective, however, at providing insight on the fundamental relationship between the various design parameters and bridge responses, so their effectiveness to explain the influence of these variables is limited.

It is therefore necessary to evaluate the influence of these different approaches to idealize soil-pile interactions on the deformations and restraint load effects of a single laterally loaded pile and an integral abutment bridge system. It is also beneficial to develop mechanics-based equations, using equilibrium and compatibility principles, to quantify the responses of integral abutment bridges and so enhance the understanding of the behavior of these systems.

1.2 Objectives

The primary objectives of the research reported in this thesis are as follows:

1. Critically evaluate the influence of the current p-y and continuum mechanics approaches on the responses of a specific single free-ended pile and a specific integral abutment bridge.
2. Investigate how the soil-pile interaction idealizations influence the deformations and restraint force effects on bridges with various geometries, stiffnesses, and soil parameters by conducting a parametric study.

3. Develop and validate a simplified model and associated mechanics-based equations, using principles of force equilibrium and compatibility, to analyze the response of the integral abutment and so quantify the deformations and restraint-induced load effects in the superstructure, abutment and piles due to thermally induced deformations of the superstructure.

1.3 Thesis Overview

Chapter 2 presents a literature review of the typical structural systems, construction sequences, applied loads of integral abutment bridges. The chapter summarizes analytical and experimental studies by others to quantify the behavior. It also describes and critically reviews different approaches to idealize the soil-pile interaction and the integration of these approaches into the structural analysis.

Chapter 3 investigates the influence of the soil-pile idealization on the lateral deflection of a single free-ended pile subjected to a lateral load or a moment applied at the pile head. Although the actual pile head is essentially fixed-ended, due to the rigid connection with the abutment, as a first step in this study a free-ended pile is investigated. The lateral and rotational stiffnesses of the soil-pile system are determined using the p-y approach and the continuum mechanics approach adapted by Basu and Salgado (2008) for cases where the soil response is linear-elastic or nonlinear. The chapter also presents a generalization of the linear-elastic response of the pile, specifically developing relationships to describe the variation of the normalized lateral deflection at the pile head with respect to the relative stiffness of the soil and pile.

Chapter 4 investigates the influence of the soil-pile idealization on the overall response of the integral abutment bridge system. Using the p-y approach and the continuum mechanics approach adapted by Basu and Salgado (2008) to quantify the lateral stiffness of the soil-pile system, the movements and restraint-induced force effects are determined for a specific integral abutment bridge subjected to either thermally induced deformations or truck loading. Differences between the predicted responses for these two approaches are quantified and critical evaluated.

Chapter 5 presents a simplified model of an integral abutment region. Using the model, mechanics-based equations are derived based on the principles of equilibrium and compatibility to quantify the deformations and restraint-induced load effects at the pile head and the end of the superstructure. The equations are validated by independent finite element analyses. The chapter also presents a parametric study that investigates the influence of soil-pile interactions on the response of integral abutment bridges with various design features and soil conditions.

Chapter 6 presents a summary and the conclusions of the research and makes recommendations for future research.

Chapter 2

2 Literature Review

Thermal expansion and contraction of bridge superstructures, comprising the bridge deck and girders, are conventionally accommodated using expansion joints. However, field investigations have clearly indicated that such expansion joints require regular and costly maintenance due to corrosion and deterioration (e.g. Johnson and McAndrew 1993). Runoff water and road salt seepage often pass through leaking expansion joints to attack the girders, bearings, and concrete abutments. Transportation agencies spend millions of dollars annually to maintain, rehabilitate, and replace bridge expansion joints (Hassiotis et al. 2006). In 2015, the direct cost of a bridge expansion joint replacement project was estimated to approach US \$285,000 (Tabrizi et al. 2016). Integral abutment bridges eliminate bearings and expansion joints and accommodate the thermally induced movements of the superstructure through displacements of the abutment and the soil-pile system. Such designs reduce the construction and maintenance costs (e.g. Hu and Wu 2014). Given these potential benefits, integral abutment bridges have been widely constructed over the past 40 years.

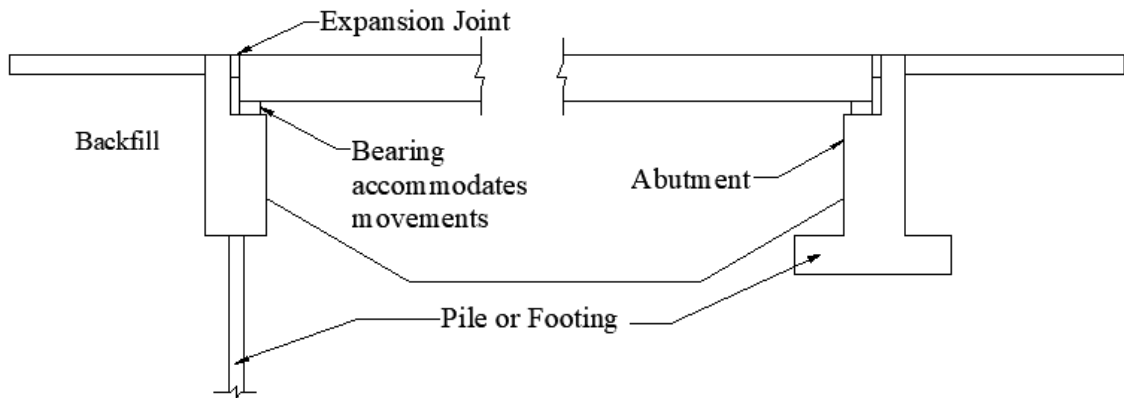
This chapter reviews previous studies that address the behavior of integral abutment bridges in relation to their structural system, construction sequence, and applied loads. It also describes the advantages and disadvantages of available design and analysis techniques to idealize soil-pile interaction. This provides a comprehensive review of the current state-of-art of the design and construction of integral abutment bridges and aids the identification of gaps in our knowledge of this technology.

2.1 General Behavior of Integral Abutment Bridges

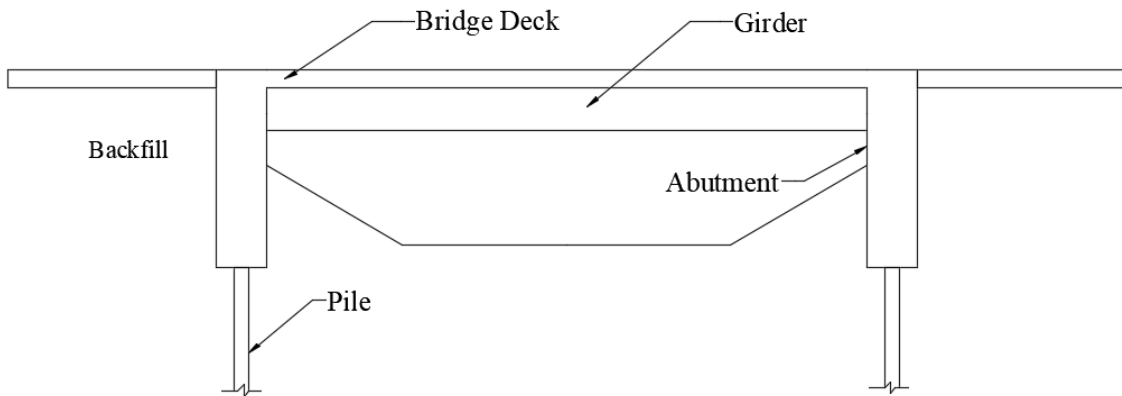
2.1.1 Introduction

Figures 2-1 (a) and (b) illustrate two common structural systems for conventional bridges with bearings and integral abutment bridges, respectively. Depending on the soil conditions, conventional bridges are typically supported on shallow foundations (e.g.,

spread footings) or deep foundations (e.g., piles). The movements of the superstructure induced by temperature variations are normally accommodated through expansion joints and bearings that do not restrain the longitudinal expansion or contraction of the bridge superstructure. In contrast to conventional bridges, integral abutment bridges eliminate the bearings and the expansion joints by integrating the bridge superstructure with the abutments. Thermally induced movements of the superstructure are accommodated by the deformations of the supporting piles.



(a) Conventional Bridge with Bearings



(b) Integral Abutment Bridge

Figures 2-1: Conventional Bridge and Integral Abutment Bridge Structural Systems

Figure 2-2 shows the structural system of a semi-integral abutment bridge, which is commonly used to retrofit existing conventional bridges. If the existing bridge has a shallow foundation, it is not practical to transform it into an integral abutment bridge since this requires disassembling the shallow foundation to install the flexible piles. The expansion joints at the end of the bridge deck are eliminated, but the superstructure is supported on new sliding bearings on, but not integrated with, the abutments. When the bridge expands or contracts, it simply slides over the abutment and the movement is accommodated by expansion joints located at the abutment/approach slab connection. New large transverse grade beams are cast behind the abutment to support the approach slab, provide a lateral force reaction surface, and separate the abutment backfill and salt water seepage from the foundation and bearing location.

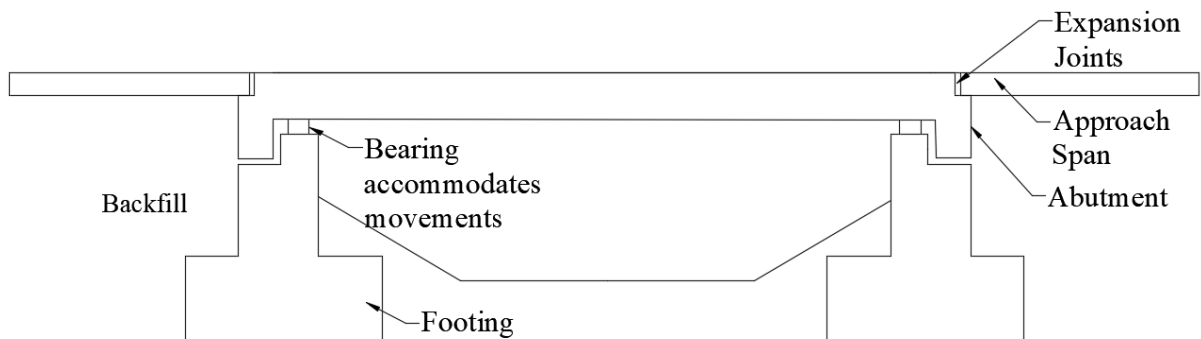


Figure 2-2: Semi-integral Abutment Bridge Structural System

2.1.2 Construction Sequence

The elimination of expansion joints introduces axial and flexural stresses into the bridge superstructure as well as flexural and shear stresses into the abutments and piles. These stresses are dependent on construction sequence. For example, the bridge performance can be enhanced if the construction sequence allows free rotation of the girder due to its own weight, and the weight of the deck slab, before the abutment concrete is placed. This construction sequence can reduce undesired stresses on fresh concrete decks, girders and abutments (Pétursson et al. 2011).

Figure 2-3 illustrates a typical construction sequence. First, (a) a hole is drilled into the ground and lined with a thin steel sleeve to stabilize the sides. Then, (b) piles are driven through the holes. The space between the piles and the sleeve is filled with loose material such as loose sand (New York State Department of Transportation 2015) or polystyrene beads to prevent direct contact between the pile and the surrounding soil, (c). Next, (d) the abutments are cast to the required bridge seat elevation, the girders are placed (e), and the bridge deck is cast (f). Then, the remainder of the abutment concrete is cast (g), making it fully integral with the bridge superstructure. Finally, (h) the void behind the abutments is backfilled and compacted.

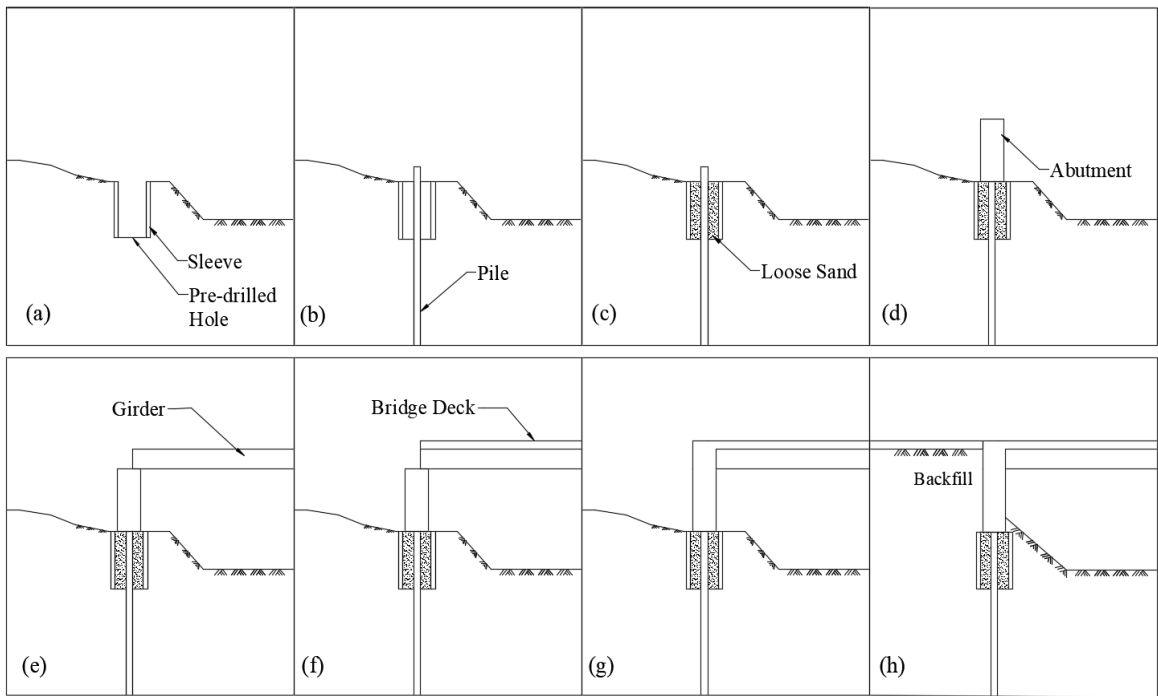


Figure 2-3: Typical Construction Sequence of Integral Abutment Bridges

In this manner, the bridge end rotations caused by the dead loads of girder and concrete deck are not constrained and so no moments are transferred into the abutments and piles. Also, since the backfill material is not added until the end of the construction process, the bridge deck is not subjected to axial compression due to earth pressure until the concrete gains sufficient strength (Pétursson et al. 2011).

2.1.3 Loads

Gravity loads, including dead load and live load, must be considered in the design of integral abutment bridges. During construction, only the vertical dead load reactions from the bridge girders and deck are transferred. At this stage, the bridge superstructure is not rigidly connected to the abutments, so the supports are normally idealized as pins or rollers.

After stage (g) in Figure 2-3, bridge deck rotations induced by the superimposed dead and live loads are restrained and cause moments, axial forces, and shear forces, at the bridge end. These load effects are then transferred to the abutments through the rigid connection between the bridge superstructure and abutments.

Table 2-1 summarizes the load effects on integral abutment bridges for various types of applied load. For each load type, the second column shows the idealization and deformed shape of the left half of a three-span bridge that is symmetric about the centerline of the middle span. The third column shows bending moment diagrams drawn for the left half of the bridge. When subjected to superimposed dead and live loads, the abutment rotates with minimal lateral translation that induces negative moment at the abutments and piers and positive moment at the mid-span.

Table 2-1: Deformations of a Multi-span Integral Abutment Bridge and Bending Moment Diagrams for a Continuous Bridge Deck

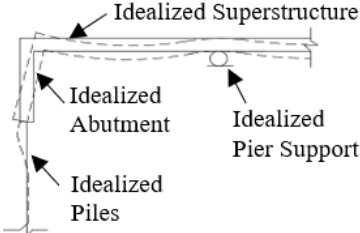
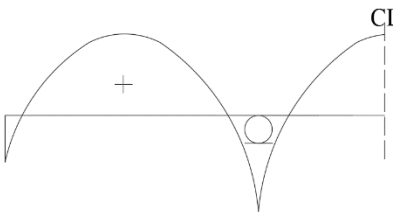
Load Type	Bridge Deformations	Bridge Deck Bending Moment Diagrams or Envelopes
Superimposed Dead Load		

Table 2-2 (Continued)

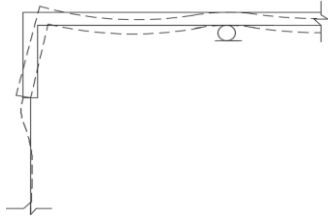
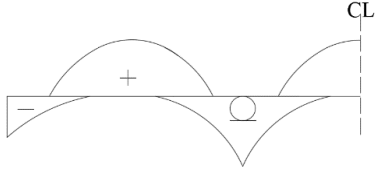
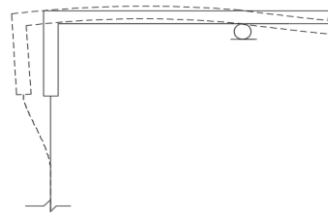
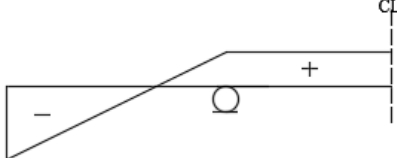
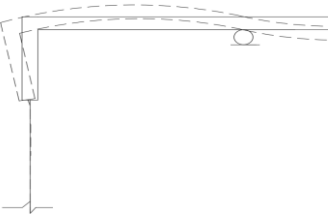
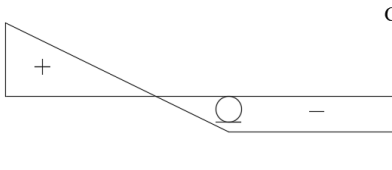
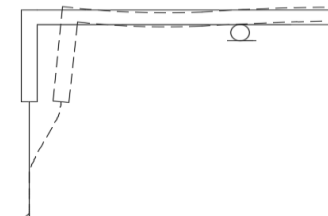
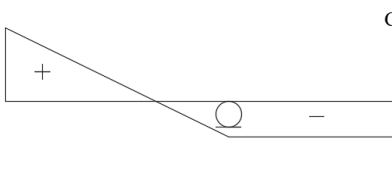
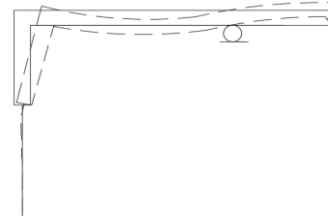
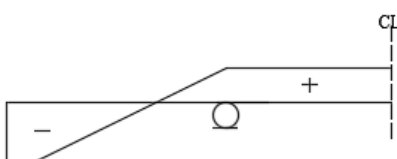
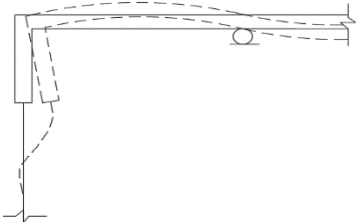
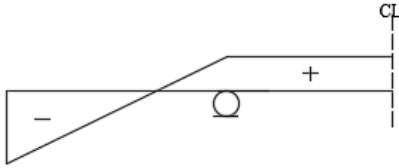
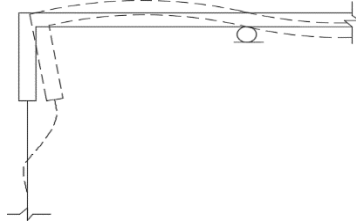
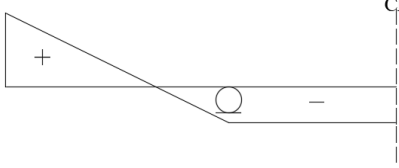
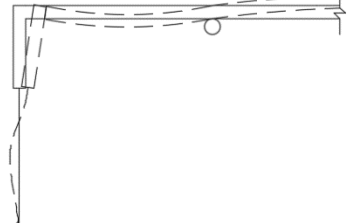
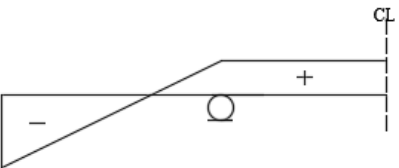
Load Type	Bridge Deformations	Bridge Deck Bending Moment Diagrams or Envelopes
<p>Live Load</p>		
<p>Temperature Rise</p>		
<p>Positive Temperature Gradient</p>		
<p>Temperature Drop</p>		
<p>Negative Temperature Gradient</p>		

Table 2-1 (Concluded)

Load Type	Bridge Deformations	Bridge Deck Bending Moment Diagrams or Envelopes
<p>Earth Pressures</p>		
<p>Creep of Prestressed Concrete Girder</p>		
<p>Shrinkage of Concrete Deck</p>		

Load effects induced by temperature variations, temperature gradients, earth pressures, creep of prestressed concrete girders, and shrinkage of concrete deck, also cause lateral movements and rotations at the bridge ends. Restraint of these lateral movements and rotations creates force effects in the abutment region, as shown in Table 2-1. Careful modelling and idealization are necessary to quantify these effects (Burke 1993).

The term ‘temperature variation’ refers to changes in the average superstructure temperature that cause a uniform strain throughout its depth. These impose cyclic longitudinal translations of the superstructure with minimal rotations at the abutment. These movements are restrained by the backfill behind the abutment and the pile-soil stiffness, accounting for soil-pile interaction, and so cause moment and axial force in the

superstructure. For example, when the temperature increases, restraint of the expansion at the abutment creates axial compression in the superstructure, and the restraint of the associated rotation induces negative moments (Table 2-1). Moments and shear forces transferred to the piles cause lateral deflections along the pile depth. As the pile deforms, the surrounding soil is further mobilized to restrain the expansion.

The term 'vertical temperature gradient' refers to a variation of temperature, often assumed to be linear, over the thickness of the deck and the height of the girder that causes an internal strain gradient over the depth of the superstructure. During the summer, the deck is warmer than the girders which results in a positive thermal gradient, whereas a negative gradient develops on winter nights when the top surface is cooler than the girders. The curvatures induced by thermal gradients cause rotation of the superstructure and abutments. The associated expansion or contraction is small because the temperature change at the neutral axis of the superstructure is typically small. Additional continuity bending moments and shear forces develop in continuous and integral abutment bridges where these end rotations are restrained (Table 2-1) by the flexural stiffness of the piles, the soil-pile interaction, and the axial stiffness of the backfill.

As integral abutment bridges expand and contract, the backfill develops earth pressures to resist these movements. The magnitude of the earth pressure depends on the ratio of translation to the abutment height. This value will lie between the passive earth pressure, when the bridge expands and the backfill approaches the point of soil failure in compression, and the active earth pressure, when the bridge contracts and the backfill approaches the point of soil failure in expansion (Craig 1983). The earth pressures can be idealized as reactions in response to the abutment movements but, as illustrated in Figure 2-4, they also can be represented as external pressures distributed linearly along the height of the abutment (Burke 1993). As shown in the figure, the earth pressure is statically equivalent to a compressive axial force and negative moment acting along the neutral axis of the bridge superstructure. Hence, as shown in Table 2-1, it causes shortening of the bridge superstructure and rotation of the abutments and so generates negative bending

moment at the abutments. It is equilibrated, as shown schematically in Figure 2-4, by the moments, shears, and axial forces in the superstructure and pile.

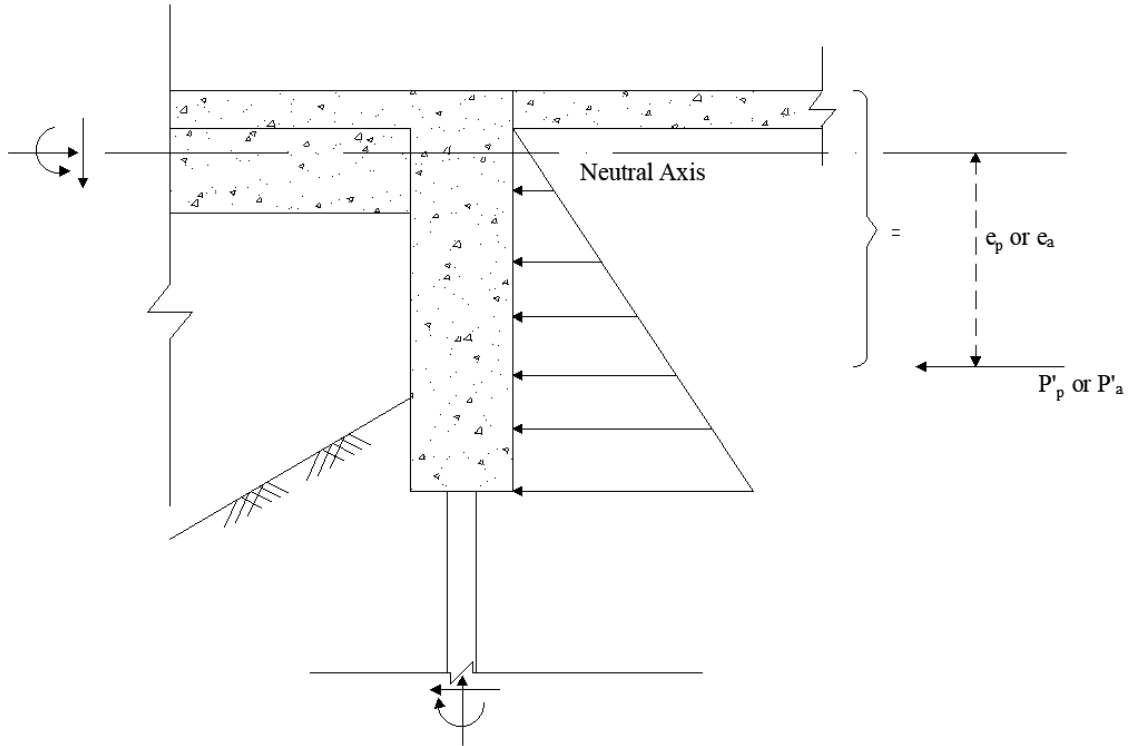


**Figure 2-4: Simplified Passive and Active Earth Pressure Distribution
(after Burke 1993)**

As the concrete deck cures, it loses moisture and shrinks. The girder restrains this shrinkage, causing compression in the girder and tension in the deck, which further causes the top of the abutment to rotate towards the span, generating the bending moments in the superstructure illustrated in Table 2-1. Restraint of these movements results in negative moment at the abutments and positive moment at the piers. These shrinkage-induced moments counteract moments due to a negative temperature variation, positive temperature gradient, and creep of the prestressed concrete girders.

Prestressed concrete girders are subjected to sustained compressive stresses that generate creep strains and deformations. If the moment induced by the eccentric compressive force exceeds the moment induced by the sustained load, as shown in Table 2-1, the

superstructure contracts and the abutment rotates away from the span, generating bending moments that are opposite to those due to shrinkage. Normally, the maximum shrinkage moments occur within 30 days after removal of the deck forms when the creep effect is minimal (Burke 1993). Subsequently, the moments induced by the creep of the concrete girders counteract the moments induced by the shrinkage of the concrete deck. The moments caused by the creep and shrinkage are typically balanced at approximately 7 to 8 months after the construction (Burke 1993).

2.2 Previous Studies of Integral Abutment Bridges

2.2.1 Introduction

Notwithstanding the wide application of integral abutment bridges, their behavior is not fully understood (e.g., Kong et al. 2016). Uncertainties exist in quantifying the influences of key design variables such as soil conditions, pile orientation, and pile sizes (David et al. 2014) when determining the maximum permissible span length or skew angle. Extensive field and numerical parametric studies have therefore been conducted to synthesize and analyze the behavior of integral abutment bridges for various bridge lengths, girder depths, foundation designs, load conditions, and soil conditions.

2.2.2 Field Studies

Table 2-2 lists instrumented integral abutment bridges to study the long- and short-term behavior induced by temperature variations and gradients. The maximum lateral pile head deflection in all the monitored bridges was less than 5% of the pile cross-sectional depth. This limit is the mean elastic limit for soil suggested by Shirato et al (2009) based on 37 field test data sets with different soil conditions and pile geometries. The coefficient of variation of the mean elastic limit is approximately 40-60%. Although Huang et al. (2011) do not report a maximum lateral pile head deflection, it can be estimated based on the reported temperature variation and bridge length. The maximum temperature change measured by Huang et al. (2004) is 40.6 °C. For a coefficient of thermal expansion of $10 \times 10^{-6} / ^\circ\text{C}$ and a total bridge length of 66 m, the translation at each end of the superstructure is approximately 13.2 mm. This is less than 5% of the pile cross-sectional

depth, (i.e., $0.05 \times 300 = 15$ mm). Since rotation of the abutment causes the deflection at the pile to be less than the bridge end translation, the pile head deflection would also have been less than 5% of the pile cross-sectional depth. This suggests that, as for the other three studies, the soil response is likely linear elastic.

As shown in Table 2-2, all of the monitored bridges are supported on H-piles bending about their weak-axes to minimize restraint, as is common American and Canadian practice (White 2007; Bloodworth et al. 2012).

Also, most of the piles were pre-drilled for their upper 3 m, Figure 2-3 (a) and the pre-drilled holes were filled with granular material, Figure 2-3 (c) after the pile installation. Typically, for bridges founded on stiff soils, pre-drilling is required before the pile installation to reduce the soil-pile stiffness. The pre-drilled hole is normally backfilled with loose material to reduce the soil restraint against the pile movements (Khodair and Hassiotis 2005; Dicleli 2000). Currently, there is no common specification regarding the backfill material. For example, Kansas, Michigan, Pennsylvania, and South Dakota require sand with no limitation to the density; California requires sand with maximum relative density of 95%; and Colorado and Iowa have used bentonite to reduce down drag on piles, but have not tried to reduce the lateral soil stiffness (Kunin and Alampalli 1999; Petursson 2015).

Table 2-2: Summary of Previous Field Studies

Case Study	Location	# of Spans	Total Length (m)	Skewness (°)	Girder	Pile	Ambient Temperature (°C)
(Huang et al. 2011)	Minnesota	3	67	0	Prestressed concrete girders	6-HP 310x79 weak-axis	max: 31, min: -38
(Civjan et al. 2013)	Vermont	3	82.3	0	Steel plate girders	5-HP 310x125 weak-axis	max: 35, min: -23
(Hassiotis and Xiong 2007)	New Jersey	2	90	15	Steel plate girders	19-HP 360x152 weak-axis	Not reported
(Fennem et al. 2005)	Pennsylvania	3	52.8	0	Prestressed concrete girders	8-HP 310x110 weak-axis	max: 22, min: -18

Table 2-2: Summary of Previous Field Studies (Continued)

Case Study	Pile Installation Method	Maximum Pile Deflection (mm)	Key Findings
(Huang et al. 2011)	Not reported	Not reported	<ol style="list-style-type: none"> 1. The measured pile strains indicated the pile flange yielded. 2. Increase in earth pressure over time was observed. 3. Long-term bridge shortening due to shrinkage of the deck, permanent abutment rotations away from the bridge spans due to creep of the girder and increase in average seasonal pile curvatures were observed.
(Civjan et al. 2013)	Pre drilled hole filled with pea stone	14	<ol style="list-style-type: none"> 1. The abutments underwent both translation and rotation when the bridge expanded or contracted.
(Hassiotis and Xiong 2007)	Pre drilled hole, sleeved, filled with sand	13.3	<ol style="list-style-type: none"> 1. The abutments experienced both translation and rotation when the bridge was subjected to thermal movements. 2. Translation at the bridge end was proportional to the temperature variation. 3. An increase in backfill earth pressure over time was observed.
(Fennema et al. 2005)	Pre drilled hole filled with loose sand	7.8	<ol style="list-style-type: none"> 1. The abutments primarily accommodated the bridge deck deformations through rotations. 2. The girder-abutment connection was not rigid. 3. Girder axial forces increased in magnitude with the increase of backfill stiffness.

The key findings from these field investigations primarily relate to the superstructure end displacement, abutment movement, abutment pile stresses, and earth pressure for known temperature variations and temperature gradients. Increased earth pressures have been observed in several field measurements (Huang et al. 2011; Breña et al. 2007; Hassiotis and Xiong 2007) with increasing cycles of temperature variation. When the bridge contracts, voids can open behind the abutment. Soil slumps into these voids and is recompacted during subsequent expansion cycles. Over the long term, the increase of earth pressures can lead to increases of abutment rotation for temperature rise and decrease of abutment rotation for temperature drop (Huang et al. 2011).

Abutments have been observed to accommodate bridge expansion and contraction through a combination of lateral translation and rotation (Civjan et al. 2013; Hassiotis and Xiong 2007; Fennema et al. 2005). The primary movement mode of the abutment depends on the soil stiffness, the earth pressures, and the height of the abutment. When the soil is stiff, the displacement at the bottom of the abutment is smaller than the displacement at the top of the abutment, causing the abutment to rotate. The earth pressure acting along the height of the abutment also causes rotation of the abutment. When the abutment is short, any induced rotation is typically insignificant, so the primary movement mode is translation.

2.2.3 Numerical Parametric Studies

Numerical parametric studies have been conducted to determine the influence of design variables on the flexural and axial stresses in the bridge superstructure, and the flexural and shear stresses in the bridge abutment and pile. The design variables considered include the end span length, bridge length, pile orientation, pile size, pile type, and type of surrounding soil

Based on previous parametric studies by others, Table 2-3 summarizes the effects of bridge length and the stiffness of the backfill, piles, and soil surrounding the piles on the stresses in the bridge superstructure, piles, and abutment. The high axial and bending rigidities of the superstructure typically cause its end translation and rotation to be insensitive to the degree of restraint provided by the backfill and piles. As the abutments or piles becomes

stiffer, however, the axial and flexural stresses in the superstructure increase (Huang et al. 2008; Baptiste et al. 2011). Therefore, design features such as short abutments, stiff piles (e.g., due to their bending about their strong axes), rigid abutment-pile connections, densely compacted backfill, and stiff soil surrounding the piles all lead to higher force effects in the bridge superstructure.

Table 2-3: Effects of Integral Abutment Bridge Design Configurations

Design Variations	Superstructure Stresses	Pile Stresses	Abutment Stresses
Increase in bridge length	↑	↑	↑
Increase in abutment height	↓	↓	-
Increase in backfill density	↑	↓	↑
Increase in pile stiffness	↑	↓	-
Increase in soil stiffness surrounding the piles	↑	↑	-

The flexural and shear stresses in the abutment are partially due to the earth pressures, which increase as the bridge total length or backfill compaction increases. Therefore, the abutment experiences higher flexural and shear stresses for longer bridges with denser backfill.

The pile moments and shear forces primarily depend on the lateral displacement at the pile head. For a given pile, abutment-pile connection, and surrounding soil, the pile stresses increase when the lateral displacement at the pile head is greater. Therefore, piles experience higher stresses in longer bridges. This also implies that greater abutment heights or backfill compaction cause decreased pile stresses because increased abutment rotation reduces the lateral displacement of the pile head, and so the pile moments and shear forces (Dicleli and Albhaisi 2003). Also, as illustrated in Figure 2-5, the abutment rotation relieves the pile restraint by introducing opposite force effects (or pile curvatures) to the pile head. This further reduces the moments along the piles (Civjan et al. 2013).

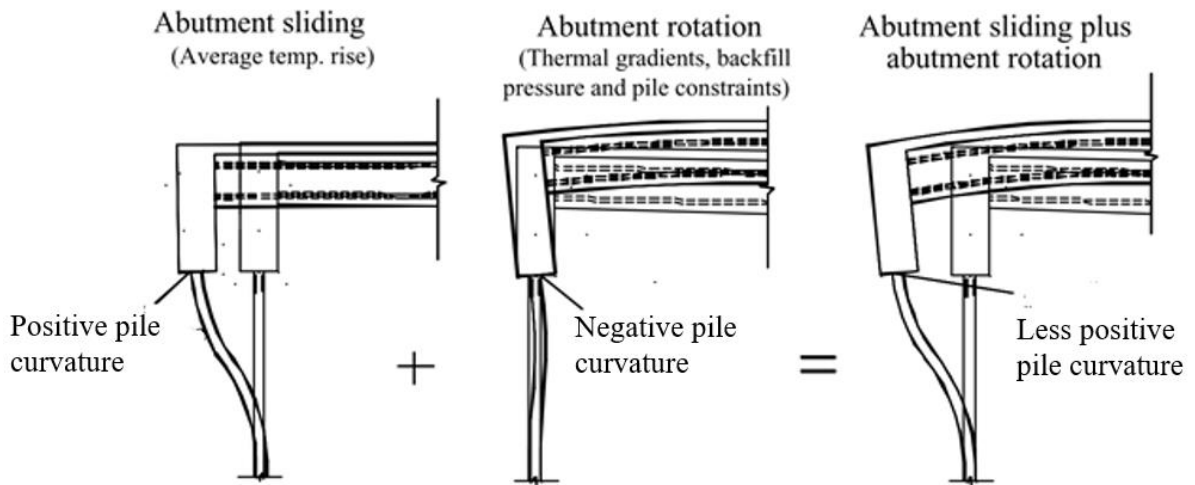


Figure 2-5: Illustration of Reduction of Pile Curvature due to Abutment Rotation (after Huang et al. 2004)

The flexural stress in the pile also depends on the relative stiffness between the pile and the surrounding soil. For a given pile head displacement, the pile flexural stresses decrease when the piles are stiffer and/or the surrounding soil is softer. For a relatively soft soil, a greater length of the pile can deform laterally, leading to reduced pile curvatures and reduced pile moments and flexural stresses (Kong et al. 2016; Huang et al. 2008; Arockiasamy et al. 2004). Therefore, for example, to reduce the pile flexural stresses, the piles are oriented to bend about the strong-axis and the stiff soil surrounding the upper regions of the piles is replaced with loose material (Arockiasamy et al. 2004). However, since an increased pile stiffness causes increased flexural and axial stresses in the bridge superstructure, there is a need to balance the stresses in piles with stresses in the superstructure when selecting the pile orientation, size, and type (Huang et al. 2008; Quinn and Civjan 2017).

Extensive numerical parametric studies have been conducted to study the influence of different design configurations on the responses of integral abutment bridges, but no study quantifies the bridge response using fundamental equations derived from the underlying mechanics, such as compatibility and force equilibrium of the structural system.

2.3 Soil-Pile Interaction Idealizations

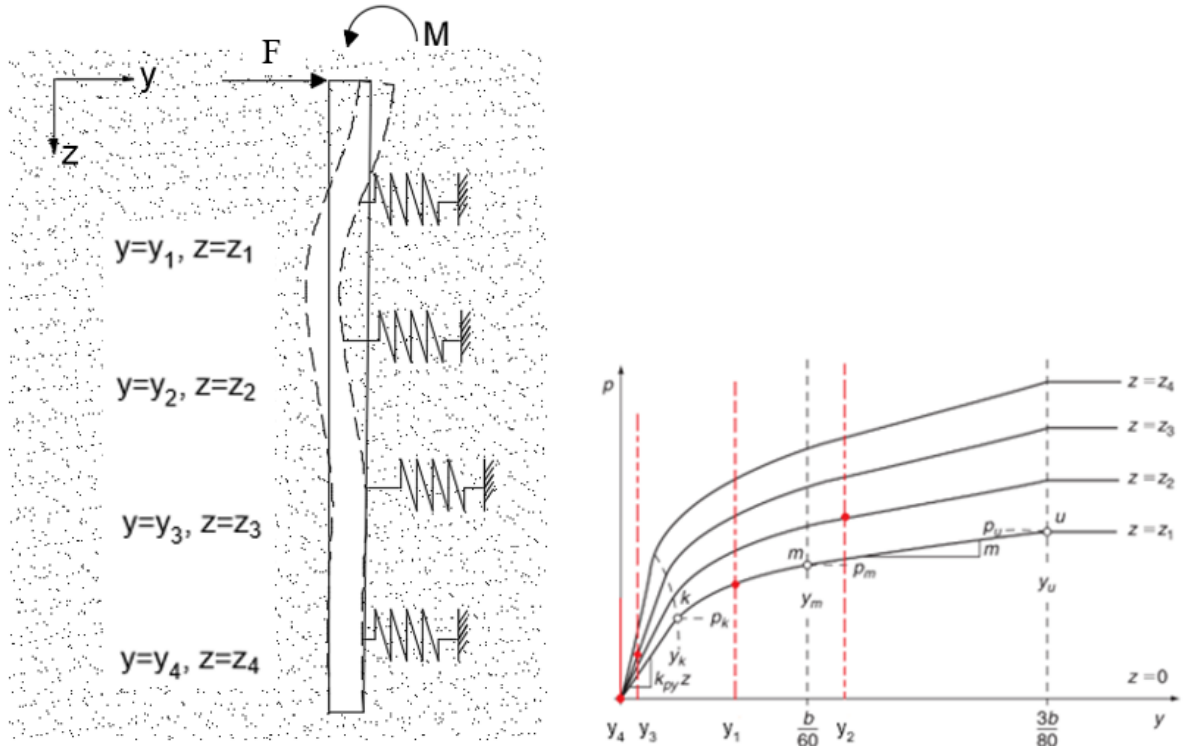
The constructional simplicity of integral abutment bridges unfortunately makes their idealization for modelling complex. In conventional bridges with bearings and expansion joints, translations and end rotation of the superstructure do not cause any appreciable force effects in the abutments, piles and the surrounding soil. The structural analysis can be conveniently conducted using independent geotechnical and structural analyses. However, in integral abutment bridges, the rigid connection between the superstructure, abutments, and piles requires a fully integrated (coupled) geo-structural analysis.

Idealization of the soil-pile interaction in the analysis of an integral abutment bridge has been found to be problematic (Faraji et al. 2001). The lateral soil reaction not only depends on the soil type, depth, and stiffness properties, but also on the lateral pile deflection. Should the soil behavior become nonlinear, the soil-pile interaction usually requires an iterative analysis to determine the soil reactions and the corresponding lateral pile deflections. Therefore, instead, two common approaches used to idealize the soil-pile interactions for laterally loaded piles are the p-y approach and the continuum mechanics approach.

2.3.1 P-y Approach

First proposed by McClelland and Focht in 1956 (Russell 2016), the p-y approach is popular for the analysis of laterally loaded piles (Faraji et al. 2001). Figures 2-6 (a) and (b) illustrated a typical soil-pile interaction idealization for a pile embedded in sand using the p-y approach. In Figure 2-6 (a), the pile is idealized as a laterally unsupported beam-column resting in a soil subgrade. The subgrade stiffness is represented by a series of independent lateral springs along the depth of the pile. When subjected to a lateral force (F) and a moment (M) at the pile head, the pile deflects laterally (y) along the pile depth (z). The p-y curves, given as input to the analysis, quantify the relationship between the unit soil lateral resistance per unit length of the pile (p) and the lateral deflection of the pile (y). As shown in Figure 2-6 (b), the curves vary along the pile depths ($z_1, z_2, z_3,$ and z_4).

Given a pile lateral deflection (y_1, y_2, y_3 , or y_4), the stiffness of each spring can be determined based on the p-y curve at the corresponding depth.



(a) Soil-Pile Interaction Idealization

(b) P-y Curves at Different Depths

Figures 2-6: Typical Soil-Pile Interaction Idealization Using the P-y Approach

The p-y curves can be determined based on field testing complex stress-strain, laboratory testing (Yang and Liang 2007; Bouafia and Garnier 1991) or finite element analysis (He et al. 2004; She 1983). Each of these methods requires time and resources that prohibit practitioners from using them in routine design.

Hence, in the majority of studies of laterally loaded piles, the p-y curves are determined empirically (e.g. Heidari et al. 2014; Dicleli and Albhaisi 2003; Faraji et al. 2001). The curve parameters, such as initial slope and ultimate capacity are empirically correlated to soil properties and strengths (Reese et al. 1974; Matlock 1970). For example, Meyer and Reese (1979) conducted 18 analyses on field tests of cyclic and static laterally loaded piles in 6 types of sand and proposed the relationship between the pile deflection and soil lateral

resistance shown in Figure 2-7. The p-y curve consists of four parts: three linear parts, labelled 1, 3, and 4, and one parabolic part, labelled 2. They proposed empirical equations to define the points of intersection, (y_k, p_k) , (y_m, p_m) , and (y_u, p_u) , based on the soil density, friction angle, coefficients of lateral earth pressure, pile diameter, and depth.

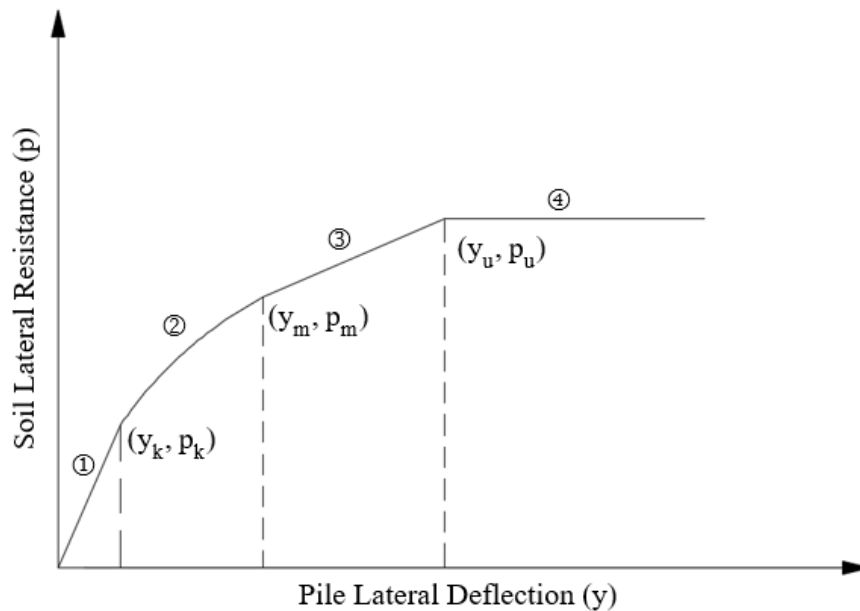


Figure 2-7: Reese P-y Curve for Sand (after Reese et al. 1974)

Notwithstanding the wide application of the p-y approach, there is evidence that it may overestimate or underestimate the pile response for different situations (Anderson et al. 2003; Russell 2016; Bustamante 2014; Kim et al. 2004). One possible reason is that the empirical p-y curves are determined based on a limited number of field tests, and so cannot accurately predict the actual soil-pile interactions for all field conditions. For example, Kim et al. (2004) conducted a geotechnical centrifuge test to determine the p-y curves for pipe piles embedded in Nak-Dong river sand. Piles were installed by driving the pile into the soil (driven pile) or by fixing the pile in place before placing the sand (pre-installed pile). During the test, the deformations at the pile head and the strains along the depth of the pile were measured and subsequently used to derive p-y curves based on Euler-Bernoulli beam theory. As shown in Figure 2-8, the derived p-y curves for the driven pile and pre-installed pile were compared with three existing p-y curves: two standardized empirical p-y curves

proposed by Reese et al. (1974) and API (2010), and a p-y curve derived based on measured data obtained from a centrifuge test for calcareous sand (Wesselink et al. 1988). The p-y curve for the pre-installed pile derived by Kim et al. (2004) was close to that obtained by Wesselink et al (1988) for a similar material, but Kim et al.'s curves are not close to the empirical relationships proposed by Reese et al and API. This example illustrates the potential problems of using the generic Reese et al (1974) and API (2010) p-y curves in producing reliable designs.

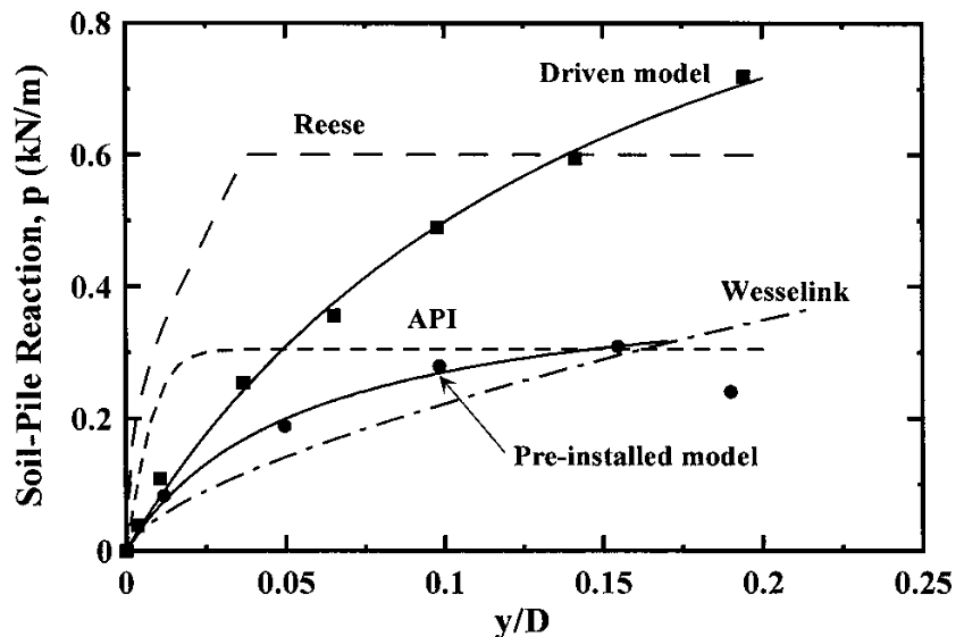


Figure 2-8: Comparison of Pile Resistance (p) and Normalized Pile Deflection y/D (D is the Pile Diameter) Curves Obtained from Experimental Tests and the Empirical Curves (Kim et al. 2004)

Moreover, even when p-y curves are determined by finite element analyses or testing for the particular field conditions, the pile-soil stiffness may be underestimated because any contribution of the shear deformation of soil to the pile-soil stiffness is not explicitly accounted for by this method. As illustrated in Figure 2-9, the lateral movement of the pile is constrained by the compressive (E_s) and shear stiffness (G_s) of the soil. When the pile deflects, causing different lateral movements of the soil at different levels, the pile deflection is constrained by the soil shear stiffness. However, in the p-y approach, the

springs representing the soil stiffness are assumed to behave independently, so its shear stiffness is not explicitly considered. Therefore, for a given displacement and rotation applied at the pile head, the p-y approach may underestimate soil stiffness as well as the moments and shear forces along the pile length, which can lead to unconservative pile design.

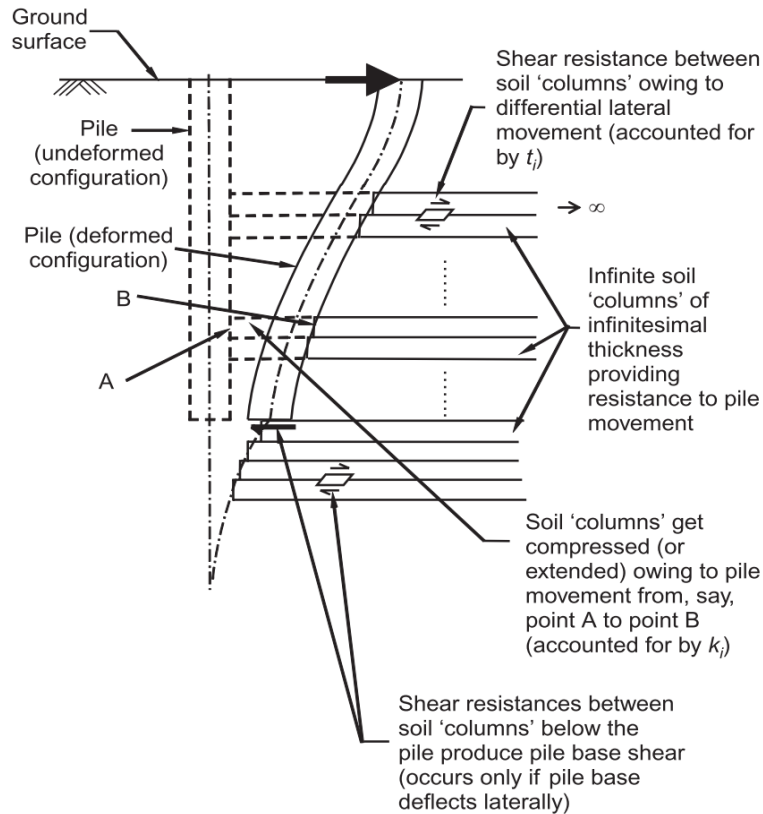


Figure 2-9: Illustration of the Two Sources of Soil Stiffnesses: Soil Compressive Stiffness and Shear Stiffness (Basu et al. 2009)

2.3.2 Continuum Mechanics Approach

As an alternative to the p-y approach, the continuum mechanics approach is more rational and versatile. It is usually based on finite-element or finite-difference numerical formulations (Gerolymos et al. 2009).

The finite-element method requires discretization of the pile and surrounding soil. The differential equations that quantify the behavior of the pile and soil are solved by minimizing the potential energy within the system:

$$\Pi = \frac{1}{2} E_P I_P \int_0^{L_P} \left(\frac{d^2 y}{dz^2} \right)^2 dz + \frac{1}{2} \int_{\Omega} \sigma_{pq} \varepsilon_{pq} d\Omega - Fw|_{z=0} + M \frac{dy}{dz} \Big|_{z=0} \quad (2-1)$$

where Π is the total potential energy in the system, $E_P I_P$ is the flexural rigidity of the pile, y is the lateral pile deflection, z is the pile depth, σ_{pq} and ε_{pq} are the stress and strain tensors in the soil, Ω represents the soil domain surrounding the pile, and F and M are the lateral force and moment applied at the pile head.

The finite element method can capture the most important features of the complex pile-soil interactions, but it is rarely used in design of laterally loaded structures owing to the high computation time required (Gerolymos et al. 2009; Kim et al. 2004).

Basu and Salgado (2008) developed a new framework based on the finite difference method for analyzing the responses of piles subjected to static or cyclic lateral forces. In their analysis framework, the pile is assumed to behave as an Euler-Bernoulli beam. The soil surrounding the pile is idealized as a linear elastic continuum. The pile is characterized by its cross-sectional dimensions, length, moment of inertia, and Young's modulus. The soil is characterized by the thickness, Poisson's ratio, and Young's modulus of each homogeneous layer.

A separable variable technique is adopted to define the displacement fields in soil. With this technique, the pile lateral deformation (u_y) is given by:

$$\mathbf{u}_y = \mathbf{y}(z) \boldsymbol{\phi}_y(\mathbf{y}) \boldsymbol{\phi}_x(\mathbf{x}) \quad (2-2)$$

where $y(z)$ is a displacement function (with a dimension of length) varying with depth z , and $\boldsymbol{\phi}_y(\mathbf{y})$ and $\boldsymbol{\phi}_x(\mathbf{x})$ are dimensionless displacement functions varying along the lateral direction (\mathbf{y}) and along the transverse direction (\mathbf{x}) respectively. The functions $\boldsymbol{\phi}_y(\mathbf{y})$ and $\boldsymbol{\phi}_x(\mathbf{x})$ describe how the soil lateral displacement decreases as the horizontal

distance from the pile increases. Substituting Equation 2-2 into Equation 2-1 and expressing the soil stresses in terms of the Lamé's constant (λ_s) and shear modulus (G_s) of the soil, Equation 2-1 can be rewritten as:

$$\begin{aligned} \Pi = & \frac{1}{2} E_p I_p \int_0^{L_p} \left(\frac{d^2 y}{dz^2} \right)^2 dz + \frac{1}{2} \int_{\Omega} \left[(\lambda_s + 2G_s) y^2 \right. \\ & \left. \left(\frac{d\phi_y}{dy} \right)^2 \phi_x^2 + G_s y^2 \phi_y^2 \left(\frac{d\phi_x}{dx} \right)^2 + G_s \left(\frac{dy}{dz} \right)^2 \phi_y^2 \phi_x^2 \right] d\Omega - Fy|_{z=0} + M \frac{dy}{dz} \Big|_{z=0} \end{aligned} \quad (2-3)$$

By applying the principle minimum potential energy, the governing differential equation is therefore:

$$\begin{aligned} & \int_0^{L_p} E_p I_p \frac{d^2 y}{dz^2} \delta \left(\frac{d^2 y}{dz^2} \right) dz + \int_{\Omega} [(\lambda_s + 2G_s) y \delta y \left(\frac{d\phi_y}{dy} \right)^2 \phi_x^2 + (\lambda_s + 2G_s) y^2 \left(\frac{d\phi_y}{dy} \right) \delta \left(\frac{d\phi_y}{dy} \right) \phi_x^2 \\ & + (\lambda_s + 2G_s) y^2 \left(\frac{d\phi_x}{dx} \right)^2 \phi_x \delta \phi_x + G_s y \delta w \phi_y^2 \left(\frac{d\phi_x}{dx} \right)^2 + G_s y^2 \phi_y \delta \phi_y \left(\frac{d\phi_x}{dx} \right)^2 \\ & + G_s y^2 \phi_y^2 \left(\frac{d\phi_x}{dx} \right) \delta \left(\frac{d\phi_x}{dx} \right) + G_s \left(\frac{dy}{dz} \right) \delta \left(\frac{dy}{dz} \right) \phi_y^2 \phi_x^2 + G_s \left(\frac{dy}{dz} \right)^2 \phi_y \delta \phi_y \phi_x^2 \\ & + G_s \left(\frac{dy}{dz} \right)^2 \phi_y^2 \phi_x \delta \phi_x] d\Omega - F \delta y|_{z=0} + M \delta \left(\frac{dy}{dz} \right) \Big|_{z=0} = 0 \end{aligned} \quad (2-4)$$

Equation 2-4 is solved by finding the optimal functions of $y(z)$, $\phi_y(y)$, and $\phi_x(x)$ such that $\delta\Pi=0$. This can be achieved using the finite difference method following an iterative algorithm. Although it has been only applied to determine the responses of generic single laterally loaded piles and group piles, it has been shown to provide results comparable to those obtained from finite element analysis and field data when the soil behavior is elastic (Basu, Salgado, and Prezzi 2008). However, when the soil is subjected to large deformations and rotations that induce non-linear behavior, the analysis overestimates the soil stiffness because the soil plasticity is neglected.

The soil input parameters required to use Basu and Salgado's (2008) approach, including Poisson's ratio and Young's modulus that corresponds to a 50% failure stress, can be either obtained from laboratory shear tests or computed from soil subgrade reaction modulus

using empirical relationships (e.g. Biot 1937; Vesic 1961; Kishida et al. 1985; Lashkaripour and Ajalloeian 2003). However, the relationships proposed by Biot (1937), Vesic (1961), and Kishida et al. (1985) were originally designed to predict the subgrade reaction modulus for shallow foundations. The application of these relationship in the estimation of horizontal Young's modulus based on subgrade reaction modulus and the corresponding influence on the prediction of lateral pile response is not well understood.

2.4 Application of P-y Approach in Integral Abutment Bridge Modelling

The process to determine the spring stiffness and structure response to analyze an integral abutment bridge using the p-y approach is iterative (David and Forth 2011). It normally requires two computational tools: (1) a soil-structure interaction analysis to generate the p-y curves and evaluate the soil stiffness, such as LPILE (Isenhower and Wang, S.T. 2013) or COM624P (Reese and Wang 1993); and, (2) a structural analysis to evaluate the structural responses, such as SAP2000 (Computers and Structures 2020). The spring stiffnesses in the first trial of the structural analysis are rough estimations based on the soil type and depth of each spring. Next, the lateral pile deflections obtained are input into the soil-structure interaction analysis program to determine the soil pressures or soil stiffnesses over the pile depth. Then the spring stiffnesses in the structural analysis program are updated to generate a new set of deflections for subsequent input to the soil-structure interaction analysis program. Iterations resume until the deflections and soil stiffnesses converge.

The p-y approach has been widely used in analytical studies and designs of integral abutment bridges (Greimann et al. 1987; Fennema et al. 2005; Baptiste et al. 2011; Faraji et al. 2001). For example, a three-dimensional (3D) finite element model was constructed by Faraji et al. (2001) to evaluate the influence of the backfill density on the integral abutment bridge behavior. Figure 2-10 illustrates the finite-element mesh for one of the abutments they studied. The bridge deck and the abutments were modeled using plate elements, while the steel girders and the piles were modeled using beam elements. The backfill-abutment interactions were idealized using non-linear springs attached to the

nodes of the finite-element mesh across the width and height of the abutment. The soil-pile interactions were modeled with 15 nonlinear lateral springs spaced equally over the length of each pile. The stiffness of each spring was defined by a p-y curve determined using recommendations (API 2011) that empirically relate the soil lateral resistance and pile lateral deflection at a given depth to the soil density, and soil angle of internal friction.

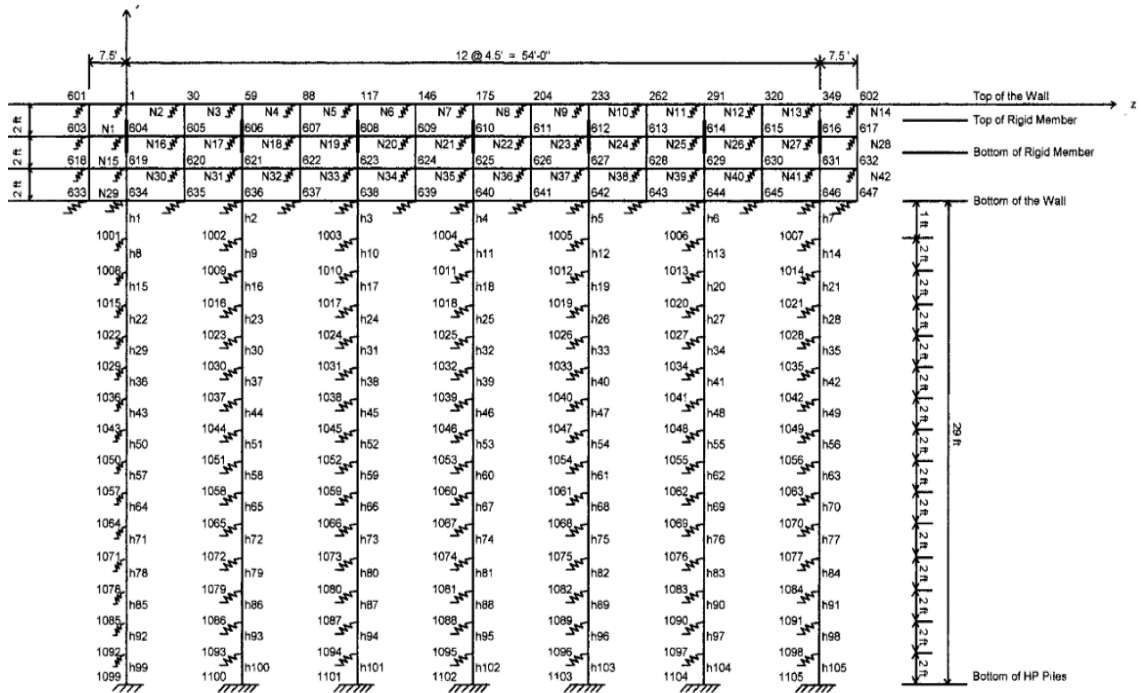


Figure 2-10: 3D model for North Abutment and H-Piles (Faraji et al. 2001)

When the bridge was subjected to temperature variations, the bridge with denser backfill experiences greater axial forces and moments in the superstructure. When the soil relative density was changed from loose to dense, the axial force and moment in the superstructure doubled, and the maximum pile moment almost doubled from 28 to 50 kN.m. Depending on the magnitude of the pile axial stress, the increase in the pile moment may lead to yielding of the pile cross-section.

Dicleli et al. (2003) created a simplified two dimensional (2D) finite element model using SAP2000 (Computers and Structures 2020) to determine the maximum length of integral abutment bridges supported on H-piles in sand. As shown in Figure 2-11, all the structural

members were conventional frame elements. Horizontal pin-ended truss elements were attached along the depth of the H-piles to represent the soil lateral stiffness. The spacing of these truss elements gradually increased along the length of the pile because the lateral soil reactions are normally concentrated within the top 5-10 pile diameters (FHWA 1986). The stiffness of each truss element was defined by a p-y curve, which was idealized as a simple bi-linear linear-elastic perfect-plastic relationships. As in Faraji's (2001) study, these bi-linear curves were determined using an empirical relationship that correlates the soil resistance to its active and at-rest earth pressure coefficients, density, coefficient of lateral subgrade reaction modulus, and angle of internal friction. Dicleli et al. (2003) found that the maximum length of the bridge is dependent upon the ability of H-piles to sustain thermal-induced cyclic deformations and the flexural capacity of the abutment. They recommended maximum lengths of 190 m and 240 m for concrete integral abutment bridges in cold and moderate climates, respectively.

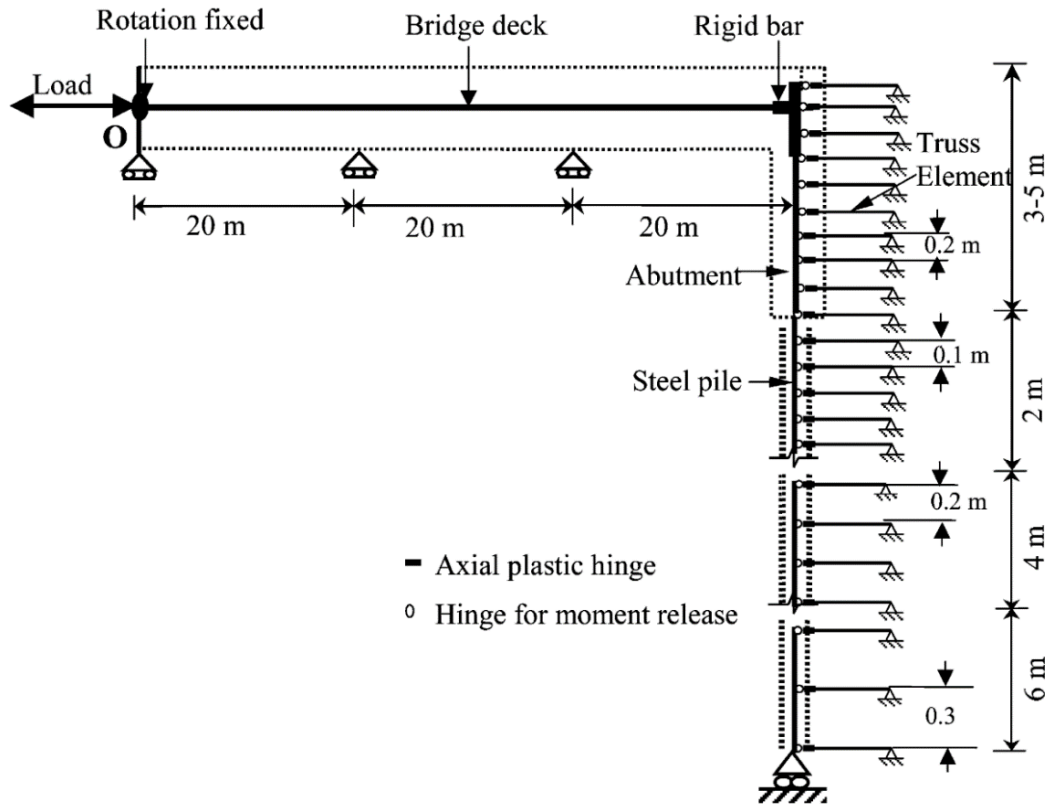


Figure 2-11: Numerical Model for Integral Abutment Study (Dicleli and Albhaisi 2003)

2.5 Summary and Conclusions

This chapter presented an overview of previous related field and numerical parametric studies related to integral abutment bridges in terms of their structural systems, construction sequence and applied loads. It also reviewed the advantages and disadvantages of available approaches to idealize the soil-pile interaction to predict the responses of laterally loaded piles.

Our current understanding of integral abutment bridges has been mainly based on field studies and numerical parametric studies. Different bridges have been instrumented to measure the variations of bridge end displacements, abutment movements, earth pressures, and abutment pile strains and stresses, whilst the bridges were subjected to dead load, live load, temperature changes, gradients, and long-term effects. Four of the most insightful field studies were described in this chapter. The key findings of these studies include:

- Following standard design practice, all of the H-piles in the instrumented bridges were orientated to bend about their weak axes, to minimize restraint of the superstructure movements. Three instrumented bridges have piles installed through pre-drilled holes and backfilled with loose material, to further reduce the restraint of the pile and superstructure bridge movements.
- Lateral earth pressures in the backfill tend to increase with time, likely because the cyclic deformations induced by the temperature variations cause the soil to slump into open voids behind the abutments when the bridge contracts that is cyclically recompacted when the bridge expands and contracts repeatedly.

In all four cases, the soil response was assumed to be in a linear-elastic, based on the soil-pile elastic limit proposed by Shirato et al. (2009).

In addition, this chapter summarized the results of previous numerical parametric studies that investigated the effect of various design features on the deflection and rotation of the abutment and the restraint force effects generated. The parameters investigated include the bridge length, abutment height, backfill compaction, pile stiffness, and the stiffness of soil surrounding the pile. The following conclusions were drawn:

- The translation at the end of the superstructure due to temperature variation is essentially independent of the stiffness of the piles or soil surrounding the piles, or of the earth pressure.
- The axial and flexural stresses in the superstructure increase with increases of the flexural stiffness of the abutment and pile, or the lateral stiffness of the backfill and soil surrounding the piles.
- The flexural and shear stresses in the pile depend on the lateral displacement at the pile head and the relative stiffness of the pile and soil. For a given temperature variation, increasing the bridge length increases these pile stresses. Increasing the abutment height or backfill compaction reduces the pile stress because the rotation of the abutment is increased in either case, and the associated displacement at the pile head is reduced. Also, increasing the pile stiffness decreases the pile stresses, but increasing the soil stiffness relative to the pile stiffness increases the pile stresses.
- The flexural and shear stresses in the abutment are partially due to the lateral earth pressures from the backfill. The abutment experiences higher stresses when the bridge length and/or the degree of backfill compaction increases.

Although extensive field and parametric studies have been conducted, the idealization of the soil-pile interaction remains challenging, particularly if the response becomes nonlinear. Two approaches available to analyze the soil-pile interaction of a single laterally loaded pile are the p-y approach and the continuum mechanics approach. The p-y approach idealizes the soil-pile interaction as a series of independent horizontal springs attached along the depth of the pile with lateral stiffness defined by empirically determined p-y curves. The continuum mechanics approach modified by Basu and Salgado (2008), on the other hand, treats the soil surrounding the pile as a continuous linear-elastic medium.

The p-y and Basu and Salgado (2008) approaches may have some limitations. The p-y approach typically characterizes the soil-pile interaction using empirical relationships derived from a limited number of tests and so may not apply to the all soil conditions. Also, it may underestimate the soil stiffness by neglecting the soil shear stiffness arising from

the differential deformations of adjacent soil layers at different depths. The Basu and Salgado (2008) approach ignores any reduction of soil stiffness that occurs when the soil behavior becomes nonlinear.

Based on this literature review, the following research gaps remain:

- The current literature concerning integral abutment bridges is mostly field studies and numerical analyses. There is no study that quantifies the bridge response using simple equations derived from the underlying mechanics, such as compatibility and force equilibrium of the structural system.
- Pile responses predicted using the continuum mechanics approach adapted by Basu and Salgado (2008), and using the p-y approach, have been compared to field data and finite element analysis results. No comparison has been made, however, of the pile responses predicted using the p-y and continuum mechanics approaches.
- Input soil parameters required to use continuum mechanics approach adapted by Basu and Salgado (2008), including Poisson's ratio and Young's modulus, can be computed from the subgrade reaction modulus using empirical relationships. Some of these relationships were originally intended to predict the subgrade reaction modulus using Poisson's ratio and Young's modulus that correspond to 50% failure stress, so the appropriateness of inverting them is uncertain.
- Basu and Salgado's (2008) approach has been used to predict the lateral deformations of generic laterally loaded piles and pile groups, but its application has not been extended to integral abutment bridges.

Chapter 3

3 Quantification of Soil-Structure Interaction in Laterally Loaded Piles

3.1 Objectives of Research Presented in this Chapter

The p-y and continuum mechanics approaches have been commonly adopted for analyzing the responses of laterally loaded piles. Chapter 2 compared the literature on the two approaches and outlined their advantages and limitations. In the p-y approach, the soil-pile interaction is modelled using independent parallel horizontal springs. The spring stiffnesses are often pre-defined by generic empirical relationships, such as the relationships proposed by Reese et al. (1974) for sand and by Matlock (1970) for soft clay. However, idealizing the soil-pile interaction as independent springs does not capture the nature of the soil as a continuum. Also, the relationships used to define the spring stiffness are developed based on a small number of field tests, so their application can be limited. Alternatively, Basu and Salgado (2008) proposed a finite-difference procedure that idealizes the soil as a linear-elastic continuum and computes the pile deflection, slope, moment, and shear force by solving differential equations to achieve the minimum potential energy. Although their approach is more rational than the p-y approach, it overestimates the stiffness because the soil behavior is non-linear. These two approaches have been adopted for a number of studies of laterally loaded piles, but their performance has not been compared and evaluated. Therefore, the objective of the research reported in the first part (Part I) of this chapter is to:

- Determine and critically evaluate any differences between the responses predicted using the two approaches for a single pile subjected to force effects that induce either a linear-elastic or nonlinear response of the surrounding soil.

To achieve this objective, numerical analyses were conducted using LPILE (ENSOFT 2005), a p-y-approach-based software, and Basu's software (Basu and Salgado 2008), a continuum-approach-based computer program created for rectangular piles. The piles and soil properties of a specific structure are used: Bridge #55555 in Minnesota (Huang et al.

2004), which is analyzed in more detail as a complete bridge structure in Chapter 4. To accommodate limitations of these programs, the H-pile cross-section is transformed into a rectangular cross-section and the seven layers of soil are idealized as four layers.

Higgins et al. (2013) defined elastic pile head lateral deflections as functions of the relative stiffness of pile and soil, and of the pile slenderness ratio. These relationships were developed by regression analyses of numerical results from a continuum-approach-based computer program created for circular piles (Basu et al. 2009). The analyses considered a single layer of soil with Young's modulus that was either constant or varied linearly with depth, and a two-layer soil with constant modulus within each layer. These pile shapes and soil conditions differ from those considered in Part 1, so the functions derived by Higgins et al (2013) are not applicable to the present study. Following their approach, however, the objectives of the research reported in the second part (Part II) of this chapter are to:

- Generalize the pile responses in Part I by quantifying the pile head lateral deflection as functions of the relative stiffness of pile and soil, for the site strata considered in Part I.
- Compare these relationships with those proposed by Higgins et al. and identify possible reasons any differences observed.

3.2 Pile Geometry and Soil Conditions

The abutment piles in Bridge #55555 are H-piles (HP) 310x79 (i.e., with a nominal depth of 310 mm and a mass of 79 kg/m). The piles are oriented to bend about their weak (y-y) axes. Table 3-1(a) summarizes the geometry and properties of the piles, which are adopted in the LPILE analyses.

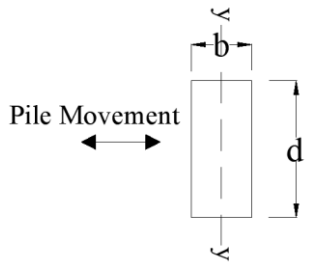
**Table 3-1(a): Pile Dimensions and Properties
Adopted in Bridge #55555 and LPILE Analyses**

Quantity	Value Adopted	Cross-Section
d (mm)	300	
b (mm)	305	
t_w (mm)	11	
t_r (mm)	11	
L_p (mm)	24400	
I_p or I_{yy} (mm⁴)	5.29E+07	
E_p (MPa)	2.00E+05	

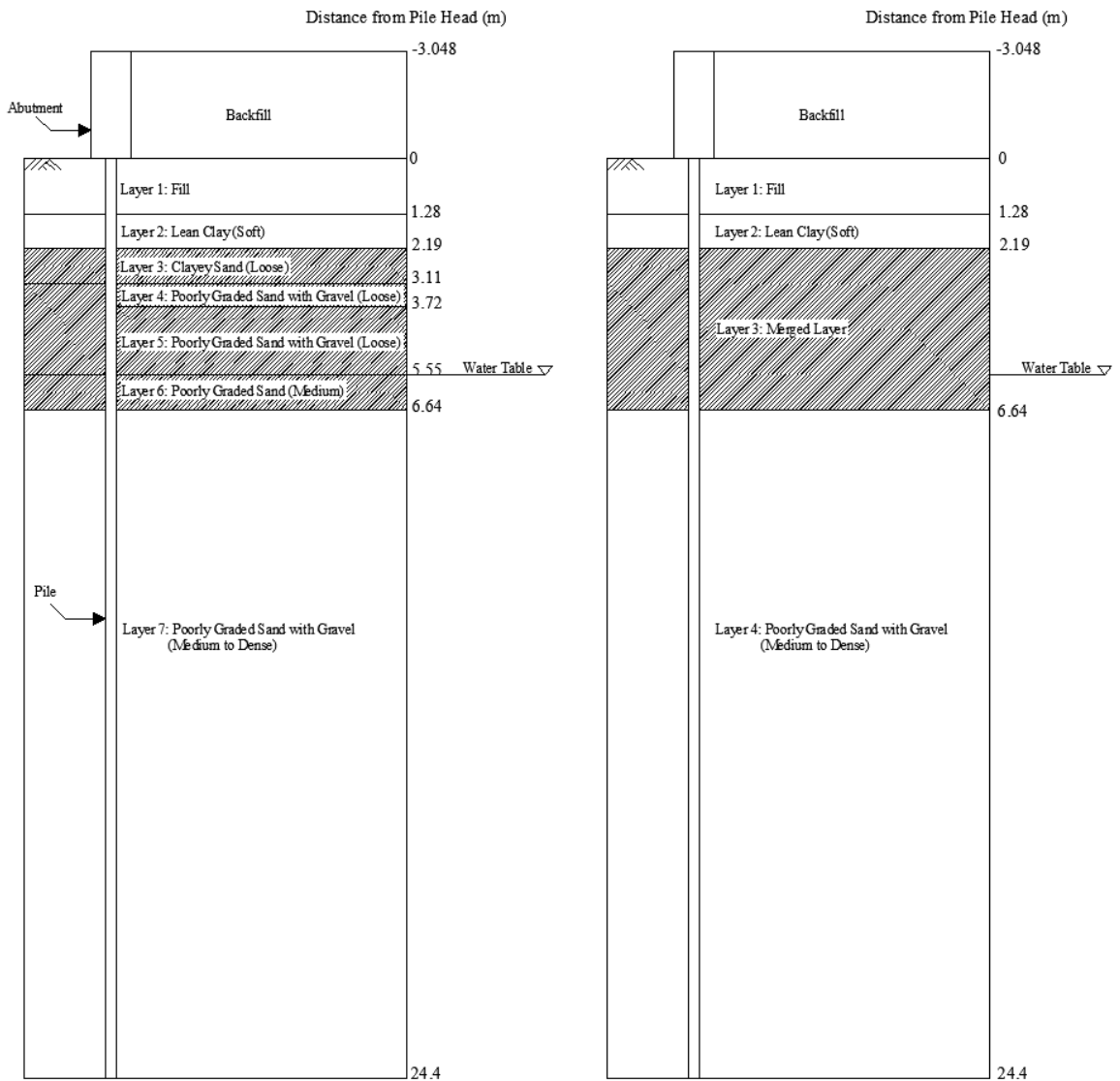
Since the p-y curves adopted in LPILE are developed from tests of circular piles, the curves are modified by a p-multiplier of 1.2 to account for the extra lateral resistance of H-piles. Previous research (Russell 2016; Bustamante 2014) has suggested that when subjected to the same lateral displacement, H-piles experience higher lateral resistance (p) than circular piles due to the increase in the side shear resistance. To study the influence of the pile shape on the lateral load resistance, Russell (2016) conducted a series of full-scale lateral load tests for both circular piles and H-piles. The test results indicated that the soil resistance of the H-piles is approximately 20% higher than that for circular piles. Therefore, the p-y curves used in the present study are increased by a p-multiplier of 1.2.

Table 3-1(b) summarizes the idealized geometry and properties adopted for the Basu analyses in the current study. Since the current version of Basu’s software only applies to piles with rectangular cross-sections, the H-pile cross-section was transformed into an equivalent rectangular cross-section. To ensure the H-pile and the rectangular pile have consistent lateral responses, the cross-sections have the same soil-pile contact area (dL_p) and flexural stiffness ($E_p I_p$) about their weak axes.

**Table 3-1(b): Equivalent Pile Dimensions and Properties
Adopted in Basu Analyses**

Quantity	Value Adopted	Cross-Section
d (mm)	300	
b (mm)	128	
L_p (mm)	24400	
I_p or I_{yy} (mm⁴)	5.29E+07	
E_p (MPa)	2.00E+05	

Figures 3-1(a) and (b) show schematically the actual soil strata under the north abutment of Bridge #55555, based on the borehole logs (Huang et al. 2004) and the merged strata adopted for the present study, respectively. As shown in Figure 3-1(a), the water table is located at the bottom surface of Layer 5, at 5.55 m below the pile head. Seven distinct soil strata are present at the north abutment, including sand and clay layers. However, Basu’s software only allows a maximum of four layers. Therefore, Layers 3-6, shown hatched in Figure 3-1(a), were merged into one layer (Layer 3), shown hatched in Figure 3-2(b), after recognizing that the merged layers have similar soil properties.



**(a) Original Soil Layers
(after Huang et al. 2004)**

(b) Merged Soil Layers

Figure 3-1: Actual and Idealized Soil Strata for Bridge #55555

In the present study, backfill is added above the pile head on both sides of the pile even though it is really only present on one side of the abutment. The soil layers added in LPILE and Basu's software must be identical on both sides of the pile. Therefore, in LPILE, the backfill was added as an extra layer on top of the pile head with the same properties as Layer 1. In Basu's software, the pile head must be aligned with the soil top surface so the

additional vertical stress due to the backfill was considered in the computation of input soil parameters for each layer.

Table 3-2(a) summarizes the thickness and properties of the seven soil layers shown in Figure 3-1(a) as obtained from the borehole results.

**Table 3-2(a): Measured Soil Strengths and Properties for Bridge #55555
(after Huang et al. 2004)**

Layer	Thickness (m)	Soil Type	Friction Angle, ϕ (Degree)	Undrained Cohesion, c_u (kN/m ²)	Strain Factor, ϵ_{50}	Unit Weight, γ (kN/m ³)
1	1.28	Sand	30	0	0	17.5
2	0.914	Lean clay	0	20.7	0.02	17.5
3	0.914	Clayey sand (loose)	30	0	0	17.5
4	0.610	Poorly graded sand with gravel	30	0	0	17.5
5	1.83	Poorly graded sand with gravel (loose)	30	0	0	17.5
6	0.914	Poorly graded sand (medium)	35	0	0	19.4
7	17.9	Poorly graded sand with gravel (medium to dense)	37	0	0	20.5

Table 3-2(b) summarizes the thickness and properties for each soil layer in the simplified profile shown in Figure 3-1(b). The friction angle, cohesion, strain factor, and unit weight of the merged layer are weighted averages, computed based on the thicknesses of Layers 3 through 6 in Figure 3-1(a). For example, the equivalent friction angle (ϕ_{eq}) of Layer 3 in Figure 3-1(b) was computed as:

$$\phi_{eq} = \frac{\sum_{i=3}^6 \phi_i t_i}{\sum_{i=3}^6 t_i} \quad (3-1)$$

where φ_i and t_i are the friction angles and the thickness respectively for Layer i in Fig. 3-1 (a).

Table 3-2(b): Soil Properties Adopted for Bridge #55555

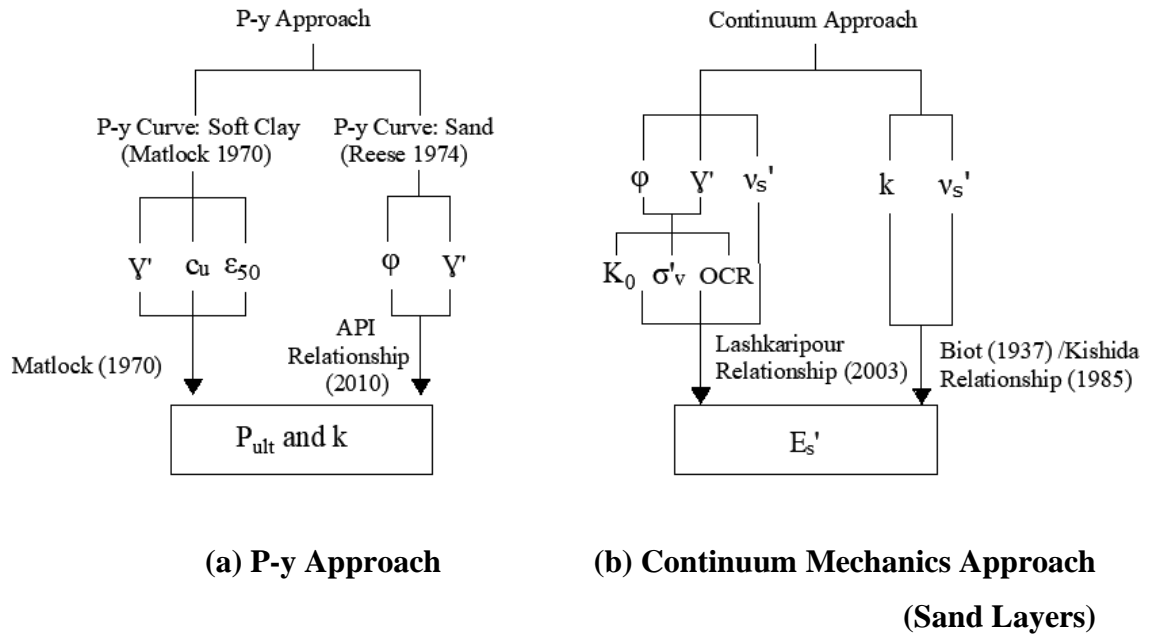
Layer	Thickness (m)	Soil Types	Friction Angle, φ (Degree)	Undrained Cohesion, c_u (kN/m ²)	Strain Factor, ϵ_{50}	Unit Weight, γ (kN/m ³)
1	1.28	Fill (sand)	30	0	0	17.5
2	0.914	Lean clay	0	20.7	0.02	17.5
3	4.27	Merged sand and gravel (loose)	31	0	0	17.9
4	17.9	Poorly graded sand with gravel (medium to dense)	37	0	0	20.5

These soil properties were input to determine the p-y curves in LPILE and to estimate the input parameters for Basu's software.

3.3 Estimation of Soil Parameters

Once the site soil properties are defined, it is necessary to quantify the soil parameters for input into the two analytical procedures. Figure 3-2(a) shows the steps taken for the estimation of input soil parameters of the p-y approach (LPILE). The p-y curve for soft clay proposed by Matlock (1970) and the p-y curve for sand proposed by Reese (1974) were used for the clay and sand layers, respectively. For the soft clay layer, the p-y curve at a given depth depends on the soil effective unit weight (γ'), undrained cohesion (c_u), and strain factor (ϵ_{50}). For the sand layers, the p-y curve at a given depth depends on the soil effective unit weight (γ') and friction angle (φ). These parameters were obtained from the borehole logs provided by Huang et al. (2004) and were used to define the p-y curves, including the upper limits (p_{ult}) for the clay layer and the slope of the straight-line portion for the sand layers. The slope of the linear portion of the p-y curves is also called the subgrade reaction modulus (k). For a certain depth, the LPILE software automatically

quantifies k based on Υ' and ϕ using an empirical relationship recommended by API (2010).



Figures 3-2: Procedure for Estimating Input Soil Parameters

Figure 3-2(b) shows the steps taken to estimate the drained Young's modulus (E_s') and Poisson's ratio (v_s') for the continuum mechanics approach (Basu's software). These can be determined directly from compression tests. However, E_s' or v_s' are not reported by Huang et al. (2004) for this site. Hence, to match the parameters between the analyses for different soil-pile idealizations, E_s' for the sand layers was deterministically estimated using three pre-established empirical relationships: Biot's relationship, (B-relationship) (1937) based on the k value obtained from the LPILE analyses; Kishida's relationship (K-relationship) (1985), also based on the LPILE k value; and Lashkaripour's relationship (L-relationship) (2003) based on the measured Υ' and ϕ . All are inherently broad approximations. The first two methods are dependent on k , and are therefore indirectly related to the p-y approach. The L-relationship is based on a soil mechanics approach that is independent of the p-y approach. It estimates E_s' based on the coefficient of earth pressure at rest, K_0 , and the effective vertical stress, σ_v' , which can be determined based on ϕ and Υ' respectively.

In the present study, the Young's modulus used for the continuum mechanics approach corresponds to the modulus at 50% failure stress. Combined with the subgrade reaction modulus, the Young's modulus is estimated and adopted in the present study as an indicator value for convenience within the analytical approaches. The values of these two parameters were estimated based on publications from the literature or selected from design manuals, so are not necessarily truly representative of the geo-mechanical stress-strain properties that may be more accurately determined with more sophisticated testing.

The backfill cannot be explicitly added into the soil model for the Basu-based analyses (continuum mechanics approach), so alternative methods were necessary to determine E_s' . For the Biot and Kishida relationships, adding the backfill above the soil strata will increase the relative depth and k values for the underlying strata. For the Lashkaripour relationship, the weight of the backfill was added as a stress increment, assumed to be constant with depth, which implies no dispersion of this stress to increasing areas with depth (likely to be a conservative assumption).

The remaining input soil parameters for the continuum mechanics approach, including v_s' for both sand and clay and E_s' for clay, were assumed based on previous results found in the literature for this soil type (Ameratunga et al. 2016).

The soil subgrade reaction modulus is not an intrinsic soil property that can be directly measured from laboratory tests. Typically, it is estimated from pre-established empirical relationships. Different relationships may yield different values of subgrade reaction modulus, hence may lead to difference in the pile response. In the present study, the subgrade reaction modulus was estimated through the empirical relationship proposed by API (2010). The applicability of this empirical relationship can be validated by comparing the pile responses obtained from the numerical analyses to responses obtained from laboratory tests conducted in the future.

The layers of different materials (i.e. sand and clay) present some challenges with respect to the drainage conditions assumed. Depending on the permeability of the soil layers, the strains of the pile, and the loading rate, the soil layers can be either in drained, undrained,

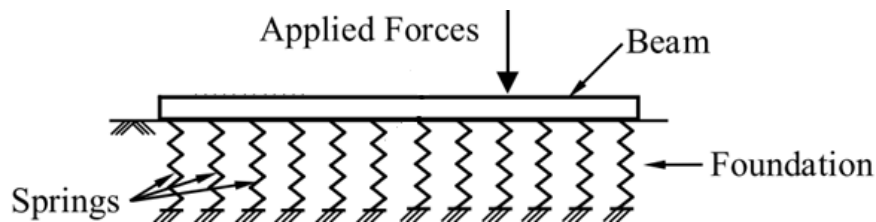
or intermediate drainage state. For self-consistency, the continuum mechanics approach (Basu analysis) uses only drained elastic properties for both sand and clay layers (Basu and Salgado 2008). The p-y approach (LPILE analysis) uses a mixed form of analysis with parameters derived from both drained and undrained laboratory tests (Isenhower and Wang 2013). Since the model parameters, p_{ult} and k are derived within the LPILE code, this also lacks theoretical rigor due to the neglect of any combined drainage conditions of the different soil layers.

3.3.1 Biot's and Kishida's Relationships

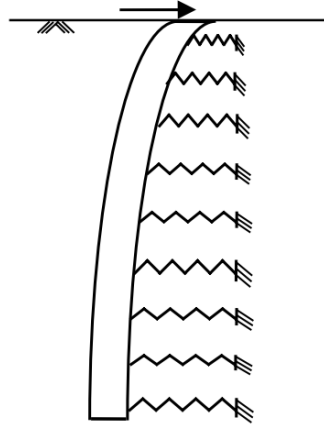
Biot (1937) conducted a series of numerical beam-on-elastic-foundation analyses for an infinite beam with a concentrated load resting on a linear-elastic soil subgrade (Figure 3-3a) (Basu et al. 2008). He compared the analytical results generated from the E_s' and ν_s' with those based on k . By matching the maximum moments in the beam, he developed the following empirical equation for k :

$$k = \frac{0.95E_s'}{(1-\nu_s'^2)} \left(\frac{E_s'B^4}{(1-\nu_s'^2)E_bI_b} \right)^{0.108} \quad (3-2)$$

where B is the width of the beam (m) and E_b and I_b are the Young's modulus (in kPa) and moment of inertia (m^4) of the beam, respectively. Since, in most cases, the piles behave in a similar manner to flexible beams but subjected to lateral loads, they can be considered to be beams-on-elastic foundations rotated by 90 degrees (Figure 3-3b) (Basu et al. 2008). Therefore, in theory Equation 3-2 can be applied to laterally loaded piles as well.



(a) Beam-on-Elastic Foundation (Basu et al. 2008)



(b) Laterally Loaded Pile in Soil (Basu et al. 2008)

Figures 3-3: Soil-Pile Interaction Idealizations

For a vertical pile, Equation 3-2 can be revised as:

$$k = \frac{0.95E_s'}{(1-\nu_s'^2)} \left(\frac{E_s' d^4}{(1-\nu_s'^2)E_p I_p} \right)^{0.108} \quad (3-2a)$$

where E_p and I_p are the Young's modulus (kPa) and moment of inertia (m^4) of the pile, respectively, shown in Table 3-1(b), and d is the depth of the pile cross-section (m).

By rearranging Equation 3-2a, E_s' can be computed as:

$$E_s' = \left[\frac{k(1-\nu_s'^2)}{0.95} \left(\frac{(1-\nu_s'^2)E_p I_p}{d^4} \right)^{0.108} \right]^{\frac{1}{1.108}} \quad (3-2b)$$

Based on the analytical results from Biot (1937), Vesic (1961) modified Equation 3-2 by matching the maximum displacements of the beam. He obtained the following relationship for k :

$$k = \frac{0.65E_s'}{1-\nu_s'^2} \left(\frac{E_s' B^4}{E_b I_b} \right)^{1/12} \quad (3-3)$$

Since the beam can be treated as a laterally loaded pile, Equation 3-3 can be revised as:

$$k = \frac{0.65E_s'}{1-\nu_s'^2} \left(\frac{E_s'd^4}{E_pI_p} \right)^{1/12} \quad (3-3a)$$

The form of Equation 3-3a is essentially identical to that of Equation 3-2a, but with different coefficients and exponents. Changing the exponents from 0.108 to 1/12, has only a slight influence on the k value, but reducing the coefficient from 0.96 to 0.65 reduces the k value by approximately 32%. As a result, the soil subgrade modulus predicted using Vesic's relationship is approximately 68% of that predicted using Biot's relationship. This difference occurs because Biot estimated the k value by matching the pile maximum deflection whereas Vesic matched the pile maximum moment. However, neither relationship correctly predicts k because neither estimates the maximum displacement and moment of the beam at the same point (Basudhar et al. 2018).

Kishida et al. (1985) conducted a series of laboratory tests on a model steel pipe pile, with a diameter of 60.5 mm and a length of 1800 mm, embedded in dry dense sand. The relationship between the applied load and pile head displacement was recorded to derive p-y curves. The slopes of the initial linear portion of the p-y curves, k, turned out to be twice that estimated using Vesic's relationship (Equation 3-3a), yielding:

$$k = \frac{1.3E_s'}{(1-\nu_s'^2)} \left(\frac{E_s'd^4}{E_pI_p} \right)^{1/12} \quad (3-4)$$

Kishida et al (1985) and Qin and Guo (2007) have suggested that more accurate predictions of pile head deformations and moments for a flexible pile subjected to a lateral load are obtained when k is computed using Equation 3-4 instead of Equation 3-3. Therefore, Equation 3-4 was adopted as one of the three relationships used for parameter estimation in the present study. From Equation 3-4, E_s' can be computed as:

$$E_s' = \left(\frac{k(1-\nu_s'^2)}{1.3} \left(\frac{E_pI_p}{d^4} \right)^{1/12} \right)^{12/13} \quad (3-4a)$$

The Poisson's ratios used in Equation 3-2b and 3-4a were estimated based on typical values for soil. Table 3-3 shows the typical ranges of Poisson's ratios for different types of soil or drainage states. From the table, the Poisson's ratios for the loose sand in Layers 1 and 3 were assumed to be 0.3 and for the medium to dense sand in Layer 4, 0.35.

Table 3-3: Typical Values of Poisson's Ratio (Ameratunga et al. 2016)

Soil Type	Drainage States	Poisson's Ratio
Loose Sand	Drained	0.1-0.3
Dense Sand	Drained	0.3-0.4
Clay	Undrained	0.5
	Drained	0.2-0.4

The previous Equations 3-2a to 3-4a all assumes that the soil behaves as an isotropic medium, since no account of the differences in horizontal and vertical elastic moduli is taken. The p-y curves for the soft clay layer (Matlock 1970) are nonlinear from the origin, so k for clay is hard to define and hence Equations 3-2b and 3-4a do not apply. Instead E_s' for the clay layer was quantified based on the typical value of the undrained Young's modulus, E_{su} as (Ameratunga et al. 2016):

$$E_s' = \frac{2}{3}(1 + \nu_s')E_{su} \quad (3-5)$$

The undrained Young's modulus was estimated based on Table 3-4 and the drained Poisson's ratio was assumed based on Table 3-3. The undrained cohesion of the clay is 20.7 kPa, so based on the classification by Ameratunga et al. (2016), the clay is on the stiff end of soft clay but soft end of medium clay. Therefore, upper bounds of soft clay were selected for the Poisson's ratio and undrained Young's modulus. With an E_{su} of 20 MPa and a ν_s' of 0.4, E_s' for the soft clay equals 18.7 MPa from Equation 3-5.

Table 3-4: Typical Values of E_{su} for Clays (Ameratunga et al. 2016)

Soil Type	E_{su} (MPa)
Very Soft Clay	0.5-5

Table 3-4 (Continued)

Soil Type	E_{su} (MPa)
Soft Clay	5-20
Medium Clay	20-50
Stiff Clay	50-100

3.3.2 Lashkaripour's Relationship

Lashkaripour and Ajalloeian (2003) performed a series of self-boring pressuremeter tests to investigate the influence of effective vertical stress, σ'_v , on the soil Young's modulus for normally consolidated sands. Based on these data, they established the following relationship between E_s' and σ'_v for different soil compaction levels:

$$E_s' = 2(1 + \nu_s') K_G \left(\frac{\sigma'_v (1 + 2K_0)}{p_a} \right)^{1/2} \quad (3-6)$$

where

K_G = empirical modulus coefficient, 313 kPa for loose sand or 516 kPa for dense sand

K_0 = coefficient of earth pressure at rest

p_a = reference stress ($p_a = 100$ kPa)

By assuming the soil in the present study is normally consolidated, the coefficient of earth pressure at rest can be estimated as $1 - \sin \phi'$.

Equation 3-6 was used to estimate the Young's modulus for sand layers. Since it only applies to sand, ν_s' for both sand and clay were taken from Table 3-3. Also, the E_s' for clay was estimated using Equation 3-5 from the assumed undrained Young's modulus based on Table 3-4.

3.3.3 Input Soil Parameters for Basu Analyses

Table 3-5 summarizes the values of E_s' and ν_s' adopted for Layers 1-4 in Figure 3-1(b). As described in Section 3.3.1, ν_s' for both sand and clay and E_s' for clay were assumed based

on the soil type (Ameratung et al. 2016). The subgrade reaction moduli for the sand layers were obtained from LPILE to estimate E_s' for the sand using the B- (Equation 3-2b), K- (Equation 3-4a), and L- (Equation 3-6) relationships. Also, the input parameters within each layer were assumed to be constant, such that the parameters estimated for the layer mid-depths are representative for the whole layer.

Table 3-5: Estimated Soil Poisson's Ratios and Young's moduli Based on Measured Soil Properties and Strengths

Layer	Soil Type	Depth Below Pile Head (m)	ν_s'	k (MPa)	σ'_v (kPa)	ϕ (deg)	K_G (kPa)	E_s' (MPa)		
								B- Relationship	K- Relationship	L- Relationship
1	Loose Sand	0.640	0.2	55.0	64.6	30	313	75.3	53.0	49.3
2	Soft Clay	1.74	0.4	NA	83.8	NA	NA	18.7	18.7	18.7
3	Medium to Dense Sand	4.33	0.2	125	125	31	516	158	113	112
4	Dense Sand	15.4	0.35	881	250	37	516	840	631	170

Comparing the E_s' values shown in Table 3-5, it is clear that those computed using the L-relationship (Equation 3-6) are generally consistent with those computed using the K-relationship (Equation 3-4a) for Layers 1 and 3. The E_s' value for Layer 4 computed using the L-relationship is only 27% of that computed using the K-relationship, however, because the k is more sensitive to the soil depth than σ_v' . When the soil depth below the pile head increases from 0.64 to 15.4 m, k increases by a factor of 16, while σ_v' increases by a factor of only 4. Also, in the K-relationship, E_s' is proportional to $k^{12/13}$, whereas in the L-relationship, E_s' is proportional to $\sigma_v'^{\frac{1}{2}}$. This difference in these exponents further increases the difference between the computed E_s' values when the depth increases.

3.4 Effect of Soil Stiffness

The piles are typically rigidly connected to the integral abutments, and so are considered to be fixed-ended. However, as a first step in investigating differences in results obtained using the LPILE and Basu analyses, a simple free-ended pile is investigated. A lateral force (F) of 40 kN and a moment (M) of 40 kN.m are applied separately at the pile head and the resulting pile deflection profiles and soil-pile lateral and rotational stiffnesses from the two analyses are compared. The Basu analyses are based on the three different sets of soil parameters shown in Tables 3-2 (a) and (b). The pile boundary conditions are assumed to be fixed at the bottom and free at the top.

Figure 3-4 shows the lateral deflections computed using the various analyses for the case of the lateral force applied at the pile head. Only deflections for the top 5 m of the pile are shown because the deflections at greater depths are negligible. For the lateral force of 40 kN, the LPILE analysis predicts the greatest pile head lateral deflection. This is approximately 52%, 36%, and 31% higher than those quantified from the Basu analyses based on the soil parameters estimated using the B- (Equation 3-2b), K-(Equation 3-4a), and L- (Equation 3-6) relationships, respectively. However, since the largest pile head deflections are less than 10 mm, the practical implications of these differences are likely slight. In addition, although the pile head lateral deflections vary between the analyses, the deflection profiles are similar. For a free-ended pile, the maximum deflection and slope

occur at the pile head. The magnitude of the lateral deflection along the pile depth decreases until the deflection reaches zero at approximately 1.5 m below the pile head for the LPILE analysis and for the Basu analysis based on the parameters estimated using the B-relationship. The locations of the zero deflection are at approximately 1.7 m below the pile head for the Basu analyses based on parameters estimated using the K- and L- relationships. Further downwards, the pile deflects in the opposite direction with the maximum magnitude at approximately 2 m below the pile head. Further downwards, the lateral deflections decrease in magnitude and start to become negligible ($|y/\Delta| < 0.5\%$, where Δ is the pile head lateral deflection) at approximately 3.5 m below the pile head for all the analyses.

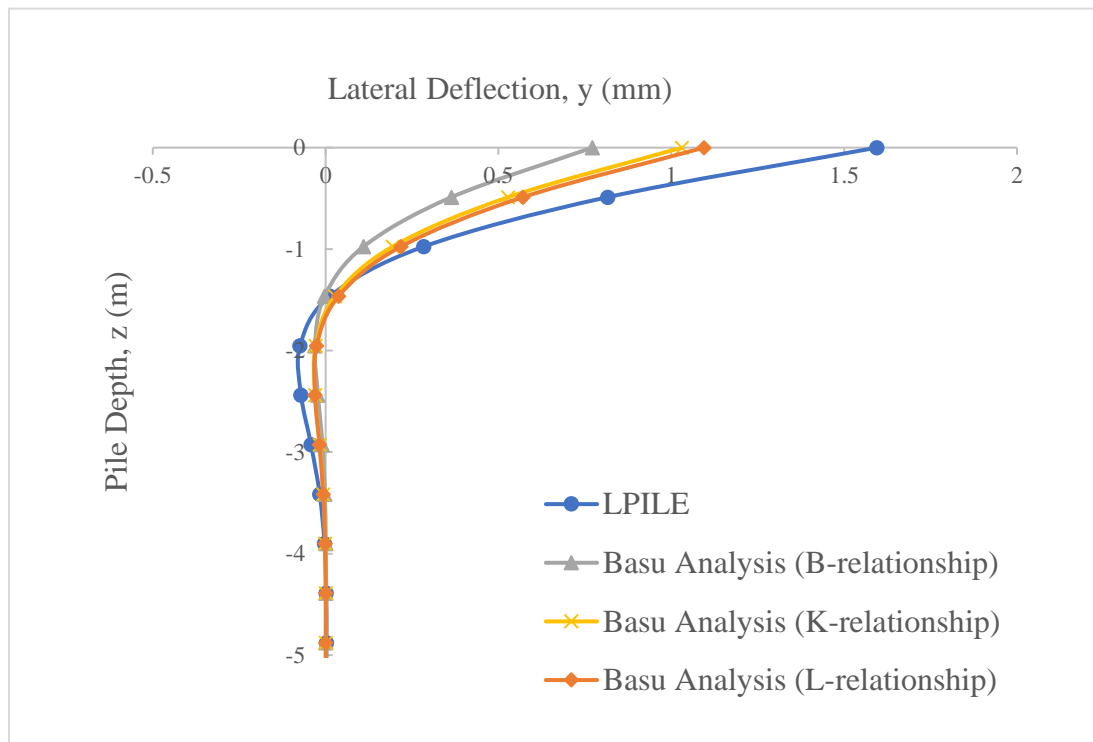


Figure 3-4: Pile Lateral Deflection Profiles (F=40 kN, M=0)

The difference in pile head lateral deflection between the LPILE and Basu analyses implies that the lateral and rotational soil-pile stiffnesses at the pile head from the LPILE analysis are lower than those found using the Basu analyses.

The following are possible explanations for the difference in the stiffness responses:

1. The continuum mechanics approach (Basu's software) captures the soil as a continuum, so it accounts for the soil shear stiffness arising due to differential deformations of soil, whereas the p-y approach (LPILE) does not.
2. The p-y curves are determined empirically based on a limited number of field tests. These curves may not apply to the current pile and soil conditions, so the p-y approach may not accurately predict the pile responses.
3. The input soil parameters adopted for the various analyses may not be exactly equivalent, even though efforts have been made to match the soil conditions in the different idealizations.
4. The drainage states of the soil input parameters are inconsistent between the LPILE and the Basu models. The Basu analyses are based on the drained Young's moduli and Poisson's ratios (Basu and Salgado 2008) whereas the LPILE analyses are based on the undrained cohesion and drained effective unit weight (Isenhower and Wang 2013). Hence, the different assumed drainage states may lead to the difference in soil-pile interactions.

In addition, pile head deflections are consistent with the input soil parameters quantified using the three relationships summarized in Table 3-5. The analysis based on the B-relationship (Equation 3-2b) yields the lowest lateral deflection and the highest pile head stiffness because the B-relationship corresponds to the greatest input soil stiffness. The pile head deflection for the B-relationship is approximately 34% and 42% lower than the K- and L-relationship, respectively. However, the implications of these differences are small given the uncertainties in soil in-situ properties. Also, analyses based on the K- (Equation 3-4a) and L- (Equation 3-6) relationships yield almost identical deflected shapes and pile head stiffness because they correspond to almost identical E_s' values in Layers 1 and 3. As previously noted, the K- and L- relationships give markedly different Young's moduli

for the lowest soil layer, Layer 4, but the influence of this is not significant because the lateral deflections in this layer are negligible.

Figure 3-5 shows the pile lateral deflections when the pile head is subjected to a moment of 40 kN.m. Again, only deflections for the top 5 m of the pile are shown because the deflections at greater depths are negligible. Similar to the responses for a pile subjected to a lateral force, the LPILE analysis provides the greatest pile head lateral deflection and slope. It is approximately 41%, 28% and 25% higher than those quantified from the Basu analyses based on the soil parameters estimated using the B- (Equation 3-2b), K-(Equation 3-4a), and L- (Equation 3-6) relationships, respectively. The lateral deflection profiles are similar to those for a pile subjected to a lateral force of 40 kN (Figure 3-4): the maximum deflections and rotations in all cases occur at the pile head and the deformations start to become negligible at approximately 3.5 m below the pile head. However, compared to Figure 3-4, the profiles in Figure 3-5 have greater slopes. As a result, the locations of zero deflection shift upward to approximately 0.4 to 0.6 m below the pile head.

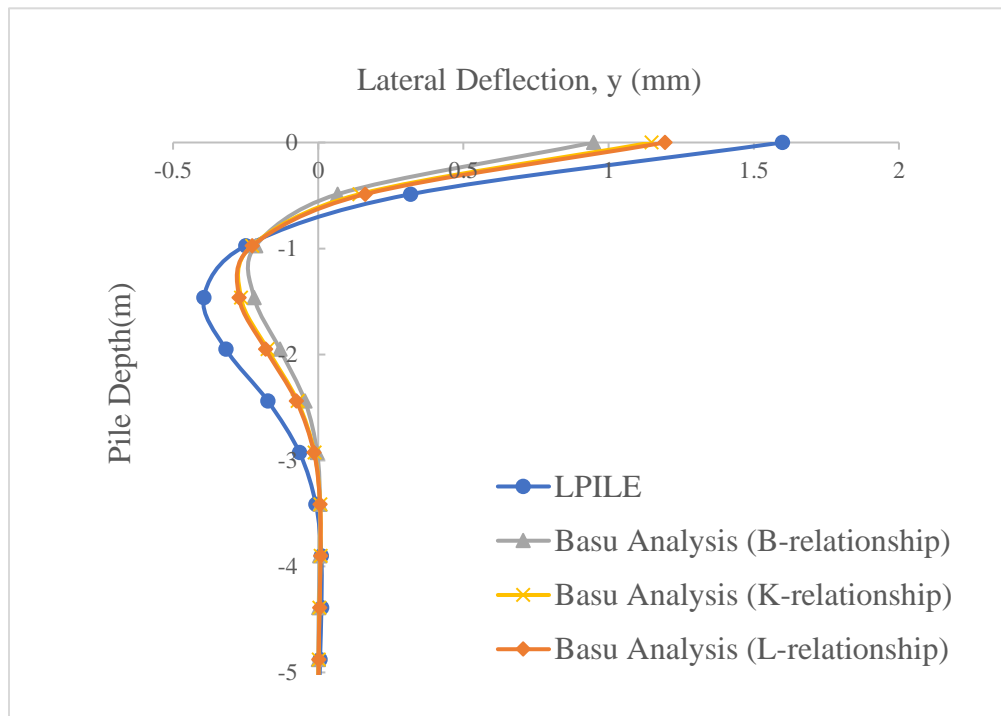


Figure 3-5: Pile Lateral Deflection Profiles (F=0 kN, M=40 kN.m)

Figure 3-5 also shows that LPILE provides the lowest soil lateral and rotational stiffness and the Basu analyses based on the B-relationship provides the highest pile head lateral and rotational stiffnesses. The Basu analyses based on the K- and L-relationships provide similar pile head lateral and rotational stiffnesses. These observations are consistent with those for the pile subjected to a lateral force, Figure 3-4.

3.5 Effect of Non-linear Soil Response

To investigate the effect of the soil response becoming nonlinear, the analyses were repeated for discrete lateral forces from 0 to 340 kN, in increments of 20 kN, applied at the pile head. This allows a comparison of the pile head deflection predicted by LPILE, which accounts for non-linear behavior of the soil, and the Basu analyses with the three sets of soil parameters, which account for only linear-elastic behavior. The pile boundary conditions were again assumed to be fixed at the bottom and free at the top.

Figure 3-6 shows the variation of pile head deflection with the applied lateral force. The pile head deflections from the Basu analyses are proportional to the applied force because Basu's software idealizes the soil as a linear-elastic material. The LPILE analysis, on the other hand, predicts a linear relationship between the pile head deflection and the applied load until the load exceeds approximately 223 kN, or the deflection exceeds 8.9 mm, which is in the range of 3.0% of the depth (d) of the rectangular cross-section. In the present study, the elastic limit is defined as the point where the initial linear region (defined by the first five data points) intersects the end linear region (defined last five data points). This limit is lower than, but comparable to, that suggested by Shirato et al (2009) who proposed a mean elastic limit of 5% of d with a coefficient of variation (COV) of 40-60% based on 37 field test data sets with different soil conditions and pile geometries.

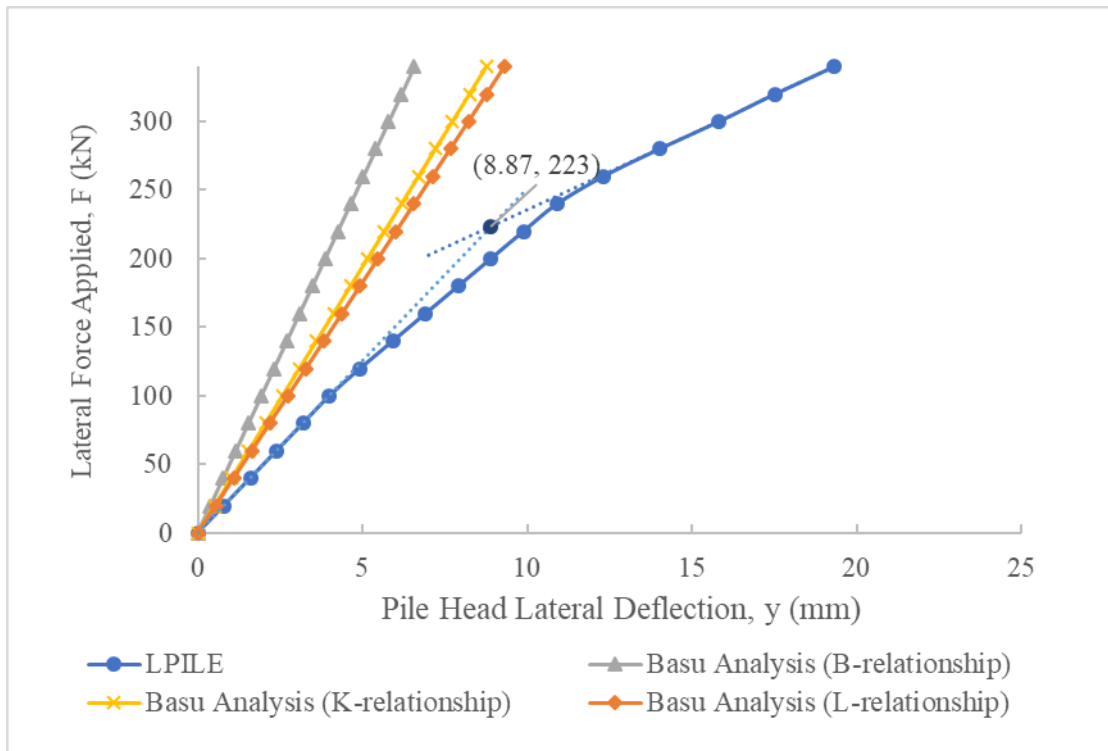


Figure 3-6: Variation of Pile Head Deflection with Lateral Force

Haldar et al. (1997) specified the pile lateral ultimate capacity as the lateral force that causing to a pile head rotation angle of 2° . Following this method, the ultimate capacity of the pile used in the present study equals approximately 468 kN, which is 110% greater than the elastic limit estimated from Figure 3-6.

The load-deflection relationship obtained using LPILE indicates that the soil behavior is initially linear-elastic, even though the p-y curve for clay is nonlinear at small deflections. This implies that any nonlinearity of the clay layer is not significant enough to influence the response of the entire pile-soil system, possibly because: (1) the clay layer is very thin; and/or (2) the reduction in slope of the clay p-y curve is not significant at small deflections.

3.6 Normalized Pile Head Lateral Deflection

Coupling the finite element method with Fourier techniques, Higgins et al. (2013) conducted numerical analyses of single free-ended circular piles subjected to a lateral force (F) or moment (M) at the pile head. The analyses considered a single layer of soil with

Young's modulus that was either constant or varied linearly with depth, and a two-layer soil with constant modulus within each layer.

For the case of a single layer of soil with a constant Young's modulus, the pile head lateral deflections (Δ) are functions of the pile slenderness ratio and the relative stiffnesses of the pile and the soil. The pile slenderness ratio is given by L_p/r , where r is the radius of the pile cross-section. The ratio of pile to soil stiffnesses is E_p/G_s^* where G_s^* is the equivalent shear modulus of soil. It considers the effect of the soil Poisson's ratio, ν_s' , on the response of laterally loaded piles (Randolph 1981), and is computed from the shear modulus, G_s' , as:

$$G_s^* = G_s' (1 + 0.75\nu_s') \quad (3-7)$$

The shear modulus, G_s' , can be derived based on the drained Young's modulus, E_s' , as:

$$G_s' = \frac{E_s'}{2(1 + \nu_s')} \quad (3-8)$$

By changing E_p/G_s^* , different lateral deflections can be obtained, and the variation of the normalized pile head lateral deflection with respect to E_p/G_s^* can be graphed. For a pile with a slenderness ratio of 80 subjected to a lateral force at the pile head, Higgins et al. obtained, using regression analysis, the following equation for normalized pile head lateral deflection:

$$\frac{\Delta G_s^* r}{F} = 0.34 \left(\frac{E_p}{G_s^*} \right)^{-0.18} \quad (3-9)$$

Similarly, when a pile with a slenderness ratio of 80 is subjected to a moment at the pile head, their regression analysis yielded the following equation for the normalized pile head lateral deflection:

$$\frac{\Delta G_s^* r^2}{M} = 0.30 \left(\frac{E_p}{G_s^*} \right)^{-0.43} \quad (3-10)$$

For the case of the two-layer soil with constant shear moduli, Higgins et al normalized the pile head lateral deflection in Equations 3-9 and 3-10 with the shear modulus of the top

layer. The relationships are characterized by the thickness of the top layer and the shear modulus ratios of the top and bottom layers.

In the present study, similar numerical analyses were performed for a rectangular pile embedded in four layers of soil with constant stiffness within each layer. Basu's software, which was created for rectangular piles, was used to obtain pile the head lateral deflections for piles with variable E_p . The pile was subjected to either a lateral force of 40 kN or a moment of 40 kN.m at the pile head. The soil properties, pile boundary conditions, and pile geometry are as described in Sections 3.2 and 3.3.

The parameters used in the Higgins et al. study for normalizing the pile head lateral deflection may not apply exactly to the present study because of the different pile shapes and soil conditions. However, a comparison is informative. The rectangular pile used in the present study does not have a radius. To facilitate the comparison with the results obtained by Higgins et al., the radius used in Equations 3-9 and 3-10 is replaced with an equivalent radius, r_{eq} , such that the moment of inertia of a circular cross-section with a radius of r_{eq} is equal to that of the rectangular cross-section. This scheme was adopted by Poulos et al. (2019) in their research to define equivalent circular piles for rectangular barrette foundations. Their numerical analysis indicated that laterally loaded circular piles have similar load-deflection responses as rectangular piles if the moment of inertia resisting the lateral deflection and pile surface area are similar. The pile surface area is simply dL when the piles bend about their weak-axis, where d is the depth of the cross-section bearing against the soil and L is the length of the pile. In the present study, the rectangular pile with a cross-sectional width of 0.3 m and a depth of 0.128 m has a r_{eq} of 0.0906 m. The use of this equivalent radius makes any comparison of normalized lateral deflections more difficult, however, because the pile surface area of the equivalent circular pile is 39.5% less than that of the rectangular pile.

Similarly, the soil shear modulus, G_s^* , used as a normalizing constant on both sides of Equations. 3-9 and 3-10, is replaced by an equivalent shear modulus, G_{seq}^* , to represent

the soil stiffness of the layered soil system. It can be calculated from the Young's moduli and thickness of all four layers ($G_{\text{seq-4}}^*$) or top two layers ($G_{\text{seq-2}}^*$):

$$G_{\text{seq-}n_s}^* = \frac{\sum_{i=1}^n \frac{(1+0.75)v_{si}'}{2(1+v_{si}')} E_{si}' t_i}{\sum_{i=1}^n t_i} \quad (3-11)$$

where n_s is the total number of layers considered and E_{si}' , v_{si}' , and t_i are the Young's modulus, Poisson's ratio, and thickness of Layer i , respectively. The values of E_s' and v_{si}' are obtained from Table 3-5 and the t_i values are obtained from Table 3-2(b). This equivalent shear modulus is again only used to normalize the lateral deflection, i.e., $\Delta G_{\text{seq}}^* r_{\text{sq}}/F$ or $\Delta G_{\text{seq}}^* r_{\text{eq}}^2/M$, and the relative stiffness, E_p/G_{seq}^* , but not in the idealization of the soil-pile system analyzed.

The accuracy of using $G_{\text{seq-2}}^*$ and $G_{\text{seq-4}}^*$ was evaluated using the B- relationship (Equation 3-2b) to determine the E_{si}' values, as shown in Table 3-5. Equation 3-11 yields, $G_{\text{seq-4}}^*$ and $G_{\text{seq-2}}^*$ values of 675 MPa and 26 MPa, respectively. Figure 3-7 (a) and (b) show the variation of the normalized pile head deflection with $E_p/G_{\text{seq-4}}^*$ (labelled as "Four Layers") and $E_p/G_{\text{seq-2}}^*$ (labelled as "Two Layers") when the pile is subjected to a lateral force or a moment, respectively. The results obtained by Higgins et al (Equations 3-9 and 3-10) are also shown. In both figures the pile head lateral deflections normalized by $G_{\text{seq-4}}^*$ are markedly greater than those obtained by Higgins et al. In contrast, the data points based on $G_{\text{seq-2}}^*$ are slightly lower than those from the study of Higgins et al: this difference barely perceptible in Figure 3-7 (a) and is slightly greater in Figure 3-7(b). The vertical axis of these figures has a linear scale and so is sensitive in changes to G_{seq}^* ; the horizontal axis has a logarithmic scale and so is much less sensitive to changes to G_{seq}^* .

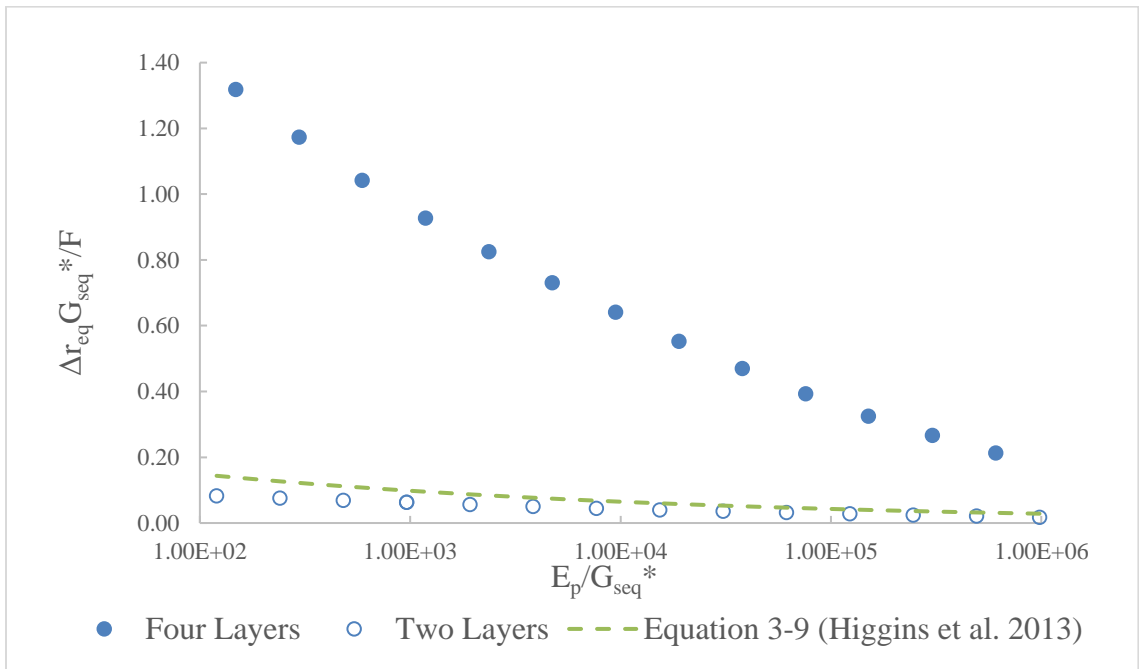


Figure 3-7(a): Variation of Normalized Pile Lateral Head Deflection with Pile-Soil Stiffness Ratio for Pile Subjected to Lateral Force

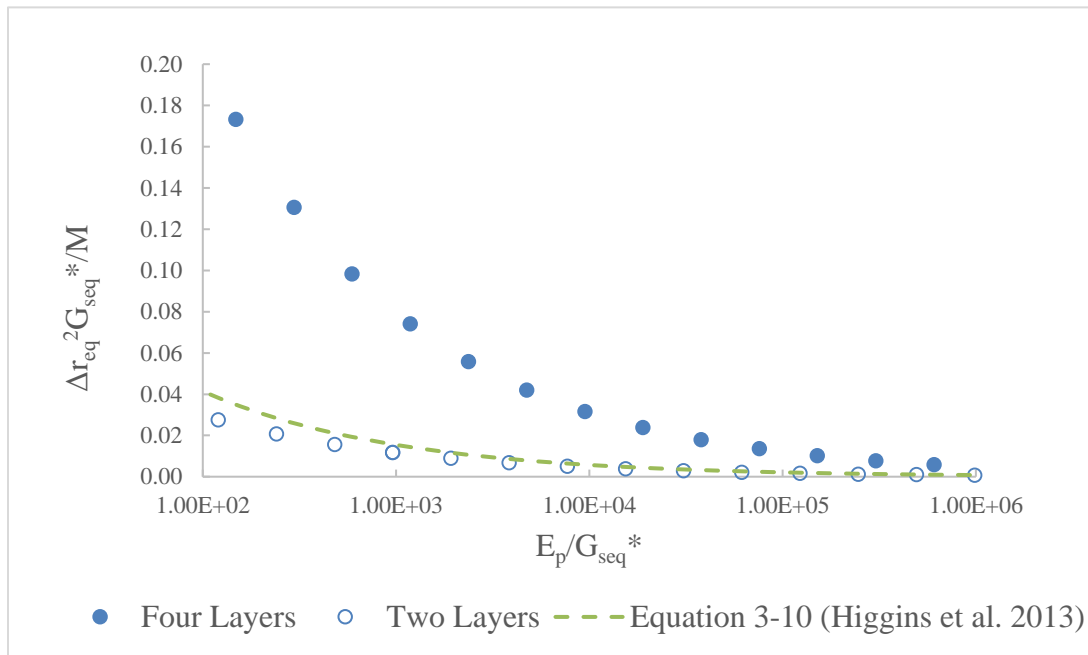


Figure 3-7 (b): Variation of Normalized Pile Head Lateral Deflection with Pile-Soil Stiffness Ratio for Pile Subjected to Moment

The considerable difference between the pile head lateral deflection normalized by G_{seq-4}^* and the relationship proposed by Higgins et al. implies that G_{seq-4}^* overestimates the stiffness of the layered soil system. This is likely because the computation of G_{seq-4}^* essentially assigns equal weights to the upper soil layers, where the lateral pile deflections are greatest, and to the lower soil layers, where, as shown in Figures 3-4 and 3-5, the lateral pile deflections are insignificant. The soil stiffnesses of the lower Layers 3 and 4 therefore have less effect on the pile response than those in the top two Layers 1 and 2. Therefore, G_{seq-4}^* significantly overestimates the stiffness of the entire soil system and, because it appears in the numerator of the normalized pile head deflection, gives higher values than reported by Higgins et al. (2013).

The normalized pile head deflections computed using G_{seq-2}^* in the present study are slightly lower than those reported by Higgins et al. This is likely because the computation of G_{seq-2}^* assign equal weights to Layers 1 and 2, where, as shown in Figures 3-4 and 3-5, the lateral pile deflection in Layer 1 is greater than in Layer 2. Therefore, when the shear modulus from the Higgins et al. study equals the equivalent shear modulus, the soil in the present study is stiffer and so the normalized pile deflection is slightly smaller. This difference is negligible, however, compared to the difference between the pile deflection normalized by G_{seq-4}^* in the present study and that reported by Higgins et al.

The fitted relationship between the normalized pile head lateral deflection and E_p/G_{seq-2}^* were then found by a form of least-squares analysis. Figures 3-8 (a), (b), and (c) shows the data points and fitted relationships of analyses conducted with E_s' quantified using the B- (Equation 3-2b), K- (Equation 3-4a), and L- (Equation 3-6) relationships, respectively. In all cases, the fitted relationships closely approximate the data points, which indicates the goodness of fit.

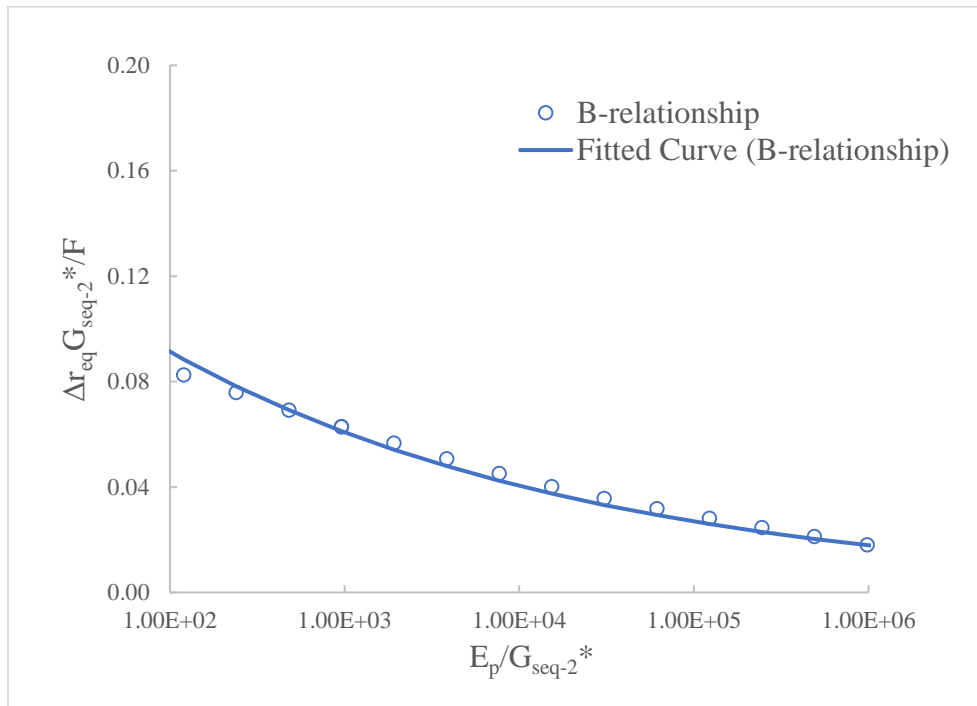


Figure 3-8(a): Curve Fitting for B-Relationship

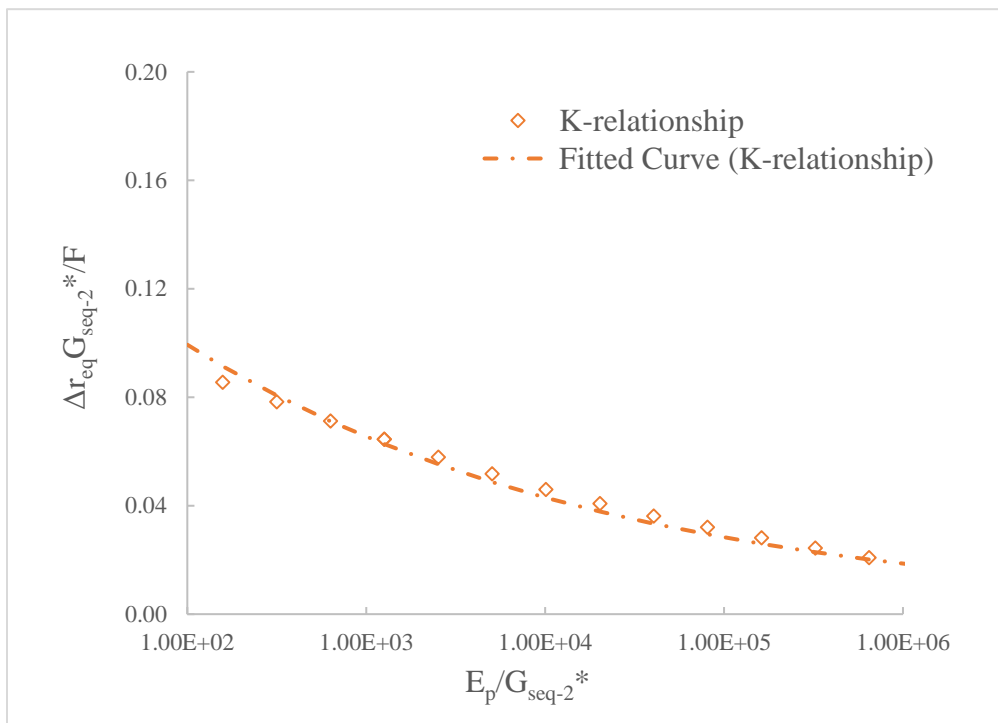


Figure 3-8(b): Curve Fitting for K-Relationship

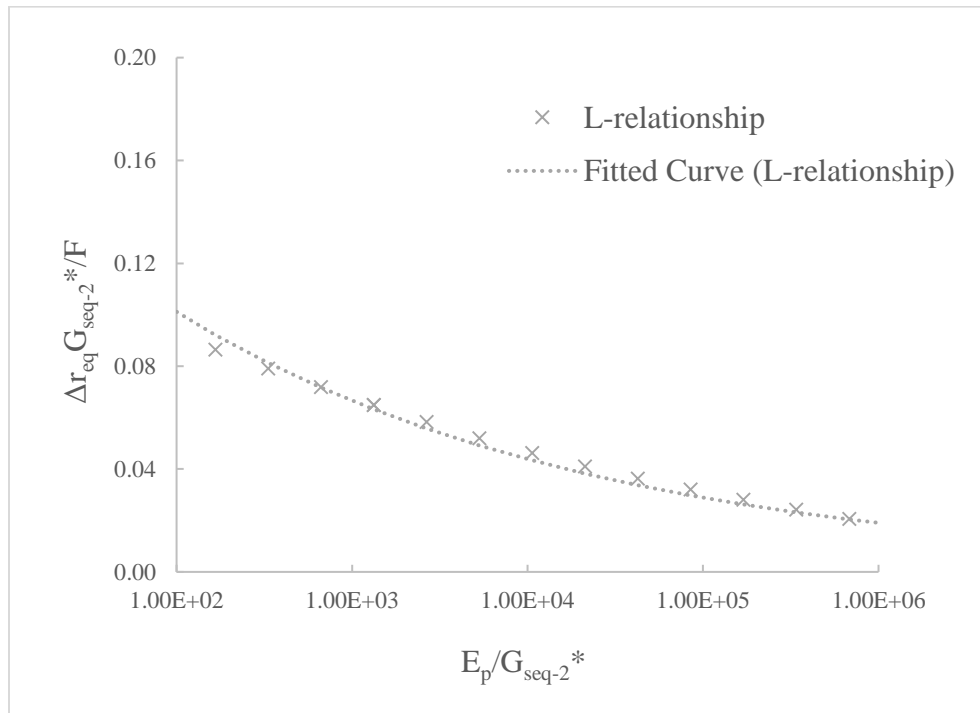


Figure 3-8(c): Curve Fitting for L-Relationship

Figure 3-9 shows the fitted relationships for normalized pile head lateral deflection with E_s' quantified using the B-, K-, and L- relationships. In general, the normalized pile head deflections from all the relationships decrease with increasing E_p / G_{seq-2}^* . Thus, for a given soil condition and applied force magnitude, increasing E_p decreases the pile head lateral deflection. At large values of E_p / G_{seq-2}^* , the pile does not deflect as a flexible pile but undergoes rigid translation and rotation, making the influence of E_p on the pile behavior negligible (Higgins et al. 2013). The normalized pile head deflections for the K- and L-relationships are indistinguishable and those for the B-relationship are slightly less. This is consistent with the values shown in Table 3-6: the E_s' and G_s^* values for Layer 1 are greatest when computed using the B-relationship and similar when computed using the K- or L-relationships, so the associated G_{seq-2}^* values are also greater. The deflections, shown for the case of E_p / G_{seq-2}^* equal to 7692 for the B-relationship and 10100 for the K, and L-relationships, are least for the B-relationship because Layer 1 is stiffer. The product ΔG_{seq-2}^* is relatively constant, in this case equal to 20.1 N/mm, 20.4 N/mm and 20.6 N/mm, respectively, for the B-, K-, and L-relationships. For a given soil condition, lateral force,

pile Young's modulus, and pile equivalent radius, the normalized pile head deflection is therefore slightly less for the B- relationship, and the difference between the K- and L- relationships is slight.

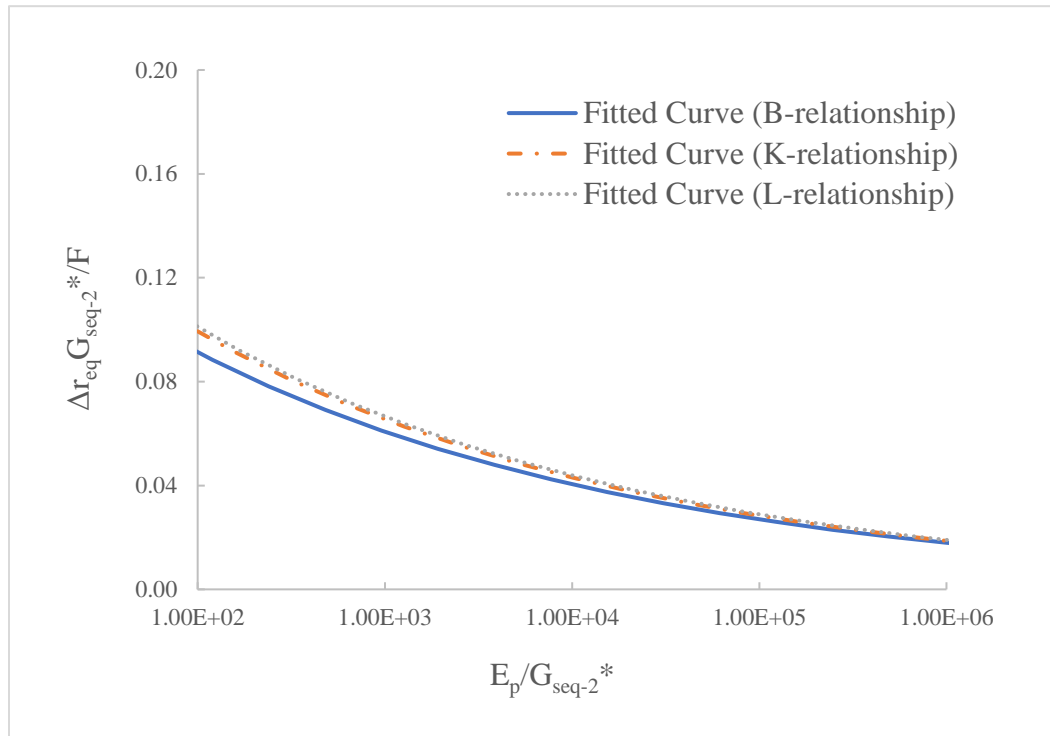


Figure 3-9: Variation of Normalized Lateral Deflection of Pile Head with Pile-Soil Stiffness Ratio for Lateral Force ($L_p/r_{eq}=271$)

Table 3-6: ΔG_{seq-2}^* for Analyses based on B-, K-, and L-Relationships

	E_s' (MPa)		G_s^* (MPa)		G_{seq-2}^* (MPa)	Δ (mm)	ΔG_{seq-2}^* (N/mm)
	Layer 1	Layer 2	Layer 1	Layer 2			
B-relationship	75.3	25	36.1	12.0	26.0	0.77	20.1
K-relationship	53.0	25	25.4	12.0	19.8	1.03	20.4
L-relationship	49.3	25	23.6	12.0	18.8	1.09	20.6

The relationships shown in Figure 3-9 are for piles with a slenderness ratio of 271, which is markedly greater than the slenderness ratio of 80 considered by Higgins et al. Figure 3-

10 compares the fitted relationships where the Basu analyses in the present study are repeated for a pile length of 7.2 m to give $L/r_{eq}=80$. The normalized pile head deflections proposed by Higgins et al. are 41%, 35%, and 35% greater than those proposed in the present study using the B-, K-, and L-relationships, respectively.

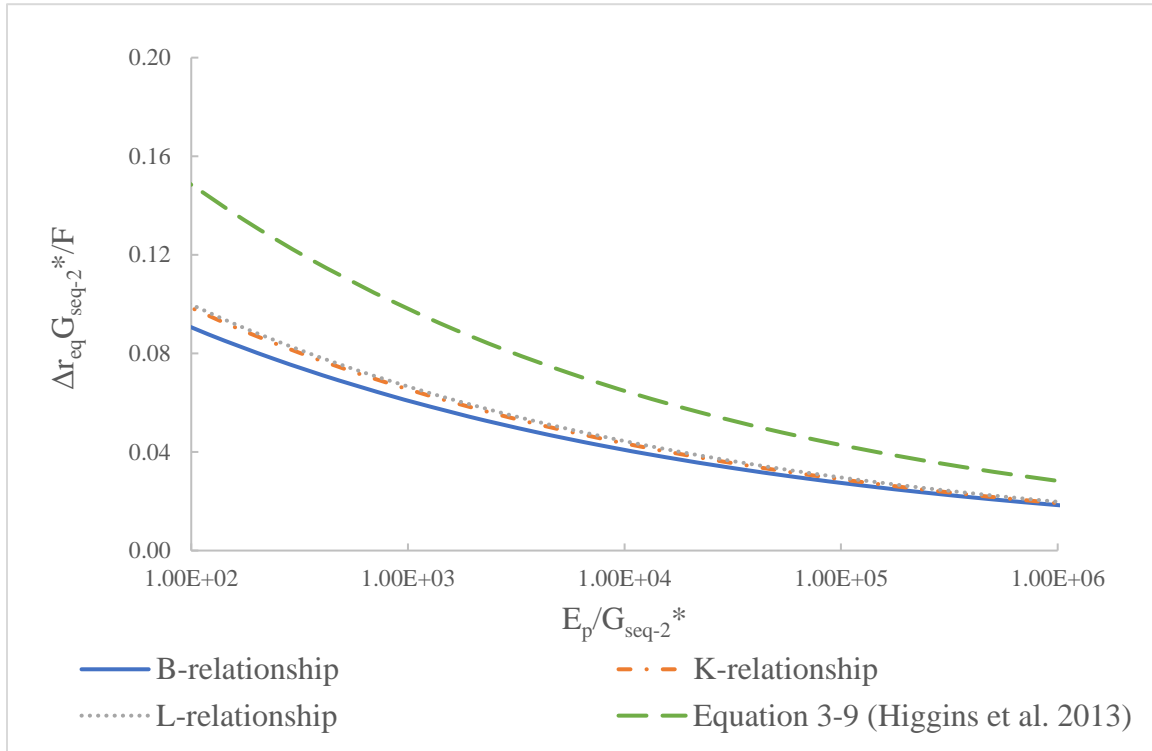


Figure 3-10: Variation of Normalized Lateral Deflection of Pile Head with Pile-Soil Stiffness Ratio for Applied Lateral Force ($L_p/r_{eq}=80$)

As noted by Higgins et al., the algebraic form of the relationships shown in Figure 3-10 is:

$$\frac{\Delta G_{seq-2}^* r_{eq}}{F} = k_1 \left(\frac{E_p}{G_{seq-2}^*} \right)^{-k_2} \quad (3-12)$$

where k_1 and k_2 are coefficients determined from the regression analysis.

Table 3-7 summarizes the value of the coefficients and the corresponding standard error showing the goodness of fit for the different methods. As the slenderness ratio decreases from 271 to 80, the normalized pile head deflection and corresponding regression coefficients hardly change. For long flexible piles, the pile lateral deflection is negligible

at great depth, so the pile lengths do not influence the deformation at the pile head significantly.

Table 3-7: Regression Coefficients for Applied Lateral Force

L_p/r_{eq} or L_p/r	Case	k_1	k_2	Standard Error
271	B-relationship	0.21	0.18	2.89E-03
	K-relationship	0.23	0.18	2.97E-03
	L-relationship	0.23	0.18	2.71E-03
80	B-relationship	0.20	0.17	2.30E-03
	K-relationship	0.22	0.18	2.39E-03
	L-relationship	0.22	0.18	2.18E-03
	Average	0.21	0.18	-
	Eq. 3-9 (Higgins et al.)	0.34	0.18	-

Table 3-7 also indicates that the average k_1 coefficient from the present study, 0.21, is approximately 62% of that from the Higgins et al. study, 0.34. This difference is attributed to the different pile geometries and pile surface area considered in the two studies. Even though the circular pile has the same moment of inertia as the rectangular pile, its pile surface area is only 60.4% of that of the rectangular pile. As a result, subjected to a given lateral force, the rectangular pile experiences higher soil resistance and hence has a lower pile head lateral deflection than the circular pile studied by Higgins et al. Therefore, the k_1 coefficient in the present study is lower than that reported by Higgins et al. Setting the equivalent pile diameter equal to the depth of pile cross-section will not duplicate the relationships proposed by Higgins et al. because the moment of inertia of the equivalent circular pile will be markedly greater than that of the rectangular pile. For a r_{eq} of 0.3 m, the moment of the inertia of the circular pile is $3.98 \times 10^8 \text{ mm}^4$, or 7.6 times greater than that of the rectangular pile.

In contrast, the average k_2 coefficient from the present study is consistent with that reported by Higgins et al. This suggests that changing the pile surface area does not influence the shape of the fitted relationships, but instead it only shifts the curve upwards or downwards.

Figure 3-11 shows the fitted relationships between the normalized pile head deflection and the relative stiffness ratio, E_p/G_{seq-2}^* for a moment applied at the pile head. As E_p/G_{seq-2}^* increases from 10^2 to 10^6 , the normalized lateral deflection decreases from 0.032 to 0.0007. This indicates for a given soil condition and applied moment, increasing E_p decreases the pile head lateral deflection. On the other hand, for a given pile and applied moment, decreasing G_{seq-2}^* increases the pile head lateral deflection.

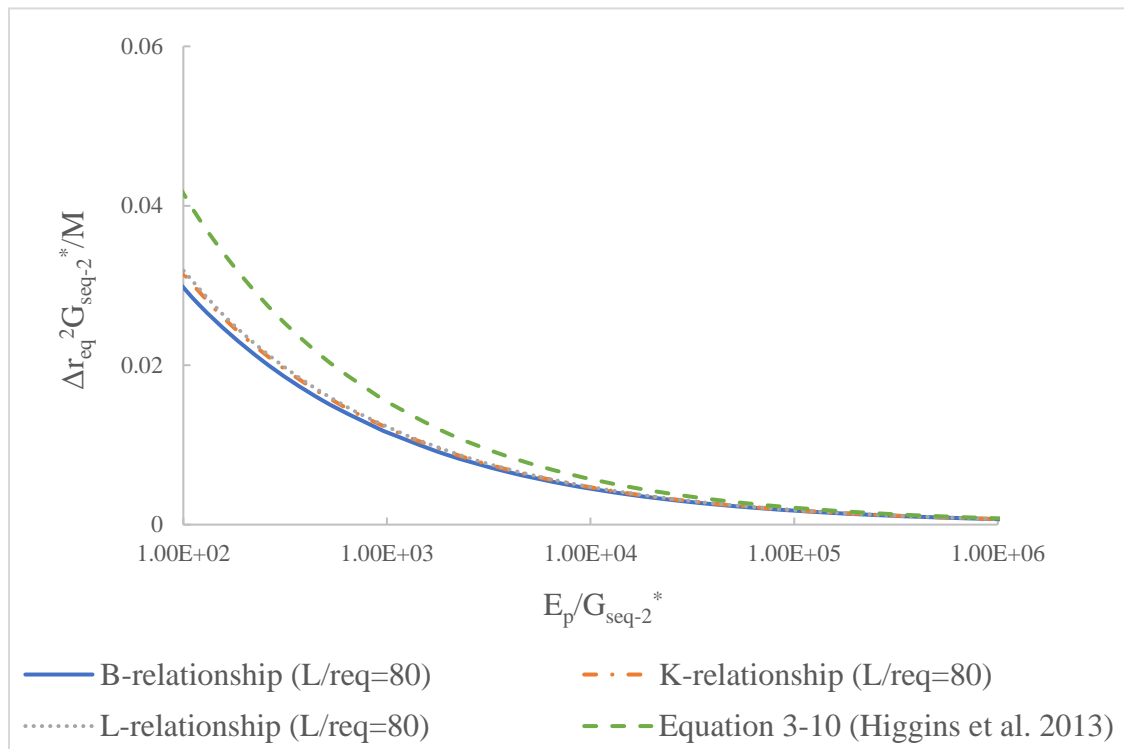


Figure 3-11: Normalized Pile Head Lateral Deflection versus Pile-Soil Stiffness Ratios for Moment ($L_p/r_{eq}=80$)

The relationships in Figure 3-11 are again of the form

$$\frac{\Delta G_{seq-2}^* r_{eq}^2}{M} = k_3 \left(\frac{E_p}{G_{seq-2}^*} \right)^{-k_4} \quad (3-13)$$

The regression coefficients k_3 and k_4 obtained using least-squares analysis are shown in Table 3-8. When the relative stiffness of pile and soil is 80, the average k_3 value from the present study is approximately 70% of that from the Higgins et al. study.

As for the case of a pile subjected to a lateral force, the regression coefficients are insensitive to the slenderness ratio. This again indicates that the pile lateral deflections are negligible at great depths, so the pile lengths do not influence the deflection at the pile head significantly.

Table 3-8: Regression Coefficients (F=0, M=40 kN.m)

L_p/r_{eq}	Case	k_3	k_4	Standard Error
271	B-relationship	0.20	0.41	1.20E-04
	K-relationship	0.21	0.41	1.13E-04
	L-relationship	0.21	0.41	1.11E-04
80	B-relationship	0.20	0.41	1.28E-04
	K-relationship	0.21	0.41	1.12E-04
	L-relationship	0.21	0.41	1.10E-04
	Average	0.21	0.41	-
	Eq. 3-10 (Higgins et al.)	0.30	0.43	-

3.7 Summary and Conclusions

This chapter presents a critical evaluation of the lateral deflection of a single free-headed pile subjected to lateral force or moment applied at the pile head as computed using the p-y and continuum mechanics approaches. Three distinct analyses are presented: (1) comparing the pile lateral deflections when the pile head is subjected to a lateral force or moment to evaluate the difference in the soil-pile stiffnesses; (2) comparing the pile head deflections for increasing lateral loads to assess the effect of accounting for soil plasticity; and (3) generalizing the lateral deflection of the head of a rectangular pile embedded in a linear-elastic layered soil subjected to either a lateral force or a moments a function of the relative stiffnesses of the pile and soil and the slenderness ratio of the pile.

The conclusions of this chapter are as follows:

1. For the specific case investigated, Basu's software (continuum mechanics approach) predicts higher soil-pile lateral stiffnesses than the p-y approach for apparently equivalent soil properties. Consequently, for a given applied lateral load

or moment, Basu's software predicts a lower lateral deflection and rotation at the pile head than the p-y approach. The pile head deflection obtained from the LPILE analyses are approximately 31-52% higher than the Basu analyses when a lateral force is applied and 25-41% when a moment is applied. However, because the largest pile head deflections are less than 10 mm, the practical implications of these differences are likely slight.

2. For a single free-ended pile subjected to a lateral force at the pile head, using the Basu software, the analysis based on the Biot relationship (Equation 3-2b) yields the lowest lateral deflection and hence the highest pile head stiffness because the Biot's relationship corresponds to the greatest input soil stiffness. The pile head deflection for the Biot's relationship is approximately 34% and 42% lower than the Kishida's and Lashkaripour's relationship. However, the implications of these differences are small given the uncertainties in soil in-situ properties. Similar responses were observed when the pile is subjected to a moment at the pile head.
3. When the maximum pile deflection is less than the linear-elastic limit of the soil, the difference between the pile responses predicted using LPILE and Basu's software is possibly due to:
 - The continuum mechanics approach (Basu's software) accounting for the soil shear stiffness arising due to differential deformations of soil, whereas the p-y approach (LPILE) does not.
 - The empirically determined p-y curves not applying to the investigated pile and soil conditions and thus may predict different lateral pile deflections.
 - The input parameters used in LPILE and Basu's software not being exactly equivalent because the parameters are computed based on different empirical equations.
 - The drainage states of the soil input parameters being inconsistent between the LPILE and the Basu approaches. The soil parameters used for the Basu

analyses are for the soil in a drained state, whereas those used for the LPILE analyses are for soil in both drained and undrained states. Such a difference in the assumed drainage states may lead to differences in soil-pile interactions.

4. When the maximum pile deflection exceeds the linear-elastic limit of the soil, the difference in the predicted pile response between LPILE and Basu's software increases because the p-y approach (LPILE) accounts for plastic behavior of soil, whereas Basu's software currently does not.
5. Using the p-y curves developed by Reese (1974) for sand and the p-y curve developed by Matlock (1970) for a thin layer of soft clay, the p-y approach predicts that the soil behavior is linear-elastic when the pile head deflection is less than 3.0% of the depth of the pile cross-section. This limit is lower than but comparable to the mean elastic limit of 5% (COV= 40-60%) proposed by Shirato et al (2009).
6. When soil behavior is linear elastic, the normalized lateral pile head deflection can be expressed as empirical functions of the relative stiffness of pile and soil, and of the pile slenderness ratio. When the pile is subjected to either a lateral force or a moment, the normalized pile head deflection decreases as the pile stiffness increases with respect to the soil stiffness. The influence of the pile slenderness ratio is negligible when the pile behaves as a long pile.

Chapter 4

4 Case Study of Integral Abutment Bridge

4.1 Objectives of Research Presented in this Chapter

Integral abutment bridges merge the bridge superstructure, abutment, and pile into a statically indeterminate structural system. When the superstructure deforms, the movements at its ends are accommodated by the piles interacting with the surrounding soil. Hence, the soil-pile idealization represents an essential part of the modelling and design of integral abutment bridges and can present a considerable challenge in the analysis of integral abutment bridges.

The p-y approach has been widely adopted in the analysis of integral abutment bridges subjected to thermally induced deformations. It is straightforward, using independent horizontal springs to represent the soil-structure interaction of the pile system. However, as described in Chapter 2, it is not always accurate since it is based on empirical relationships developed from a limited number of field tests. The continuum mechanics approach modified by Basu and Salgado (2008), on the other hand, has not been used in the idealization of any integral abutment bridges, but has been shown to yield accurate predictions for a single laterally loaded pile (Basu and Salgado 2008) and pile groups (Basu et al. 2008) through comparison with full-scale pile tests and finite element analyses. However, as described in Chapter 3, it considers only the linear-elastic response of the soil and therefore neglects any reduction of the soil stiffness due to a nonlinear response at higher soil strains. Neither approach is perfect. Therefore, the research presented in this chapter will critically assess how the limitations in the soil-pile interaction idealizations influence the prediction of load effects of a specific integral abutment bridge, Bridge #55555 in Minnesota, when the bridge is subjected to thermally induced deformations.

In addition, when integral abutment bridges are subjected to truck loadings, the abutments rotate with minimal lateral translations, as described in Chapter 2. The idealization of the soil-pile interaction may therefore have different influences on the response compared to the case of thermally induced deformations. Lawver et al. (2000) conducted a truck loading

test on Bridge #55555. The moments along the bridge superstructure were measured and then compared with the computed moments that were obtained from two simplified models, which idealized the bridge exterior span as pinned at the interior pier and either simply supported or fixed at the abutment. Since the actual fixity of the abutment-soil-pile system was not captured, however, these two simplified models only provide the upper and lower bounds of the rotational stiffnesses of the abutment-soil-pile system, and hence only approximate moment values. Therefore, the truck loading case will be re-analyzed using the p-y and Basu approaches. The computed moments will be compared with those from Lawver et al.'s simplified models and field measurements.

4.2 Bridge Description

The numerical analyses in the present research are based on the geometries and properties of Bridge #55555 located in Rochester, Minnesota, as reported by Huang et al. (2004). This bridge was selected for the present study because:

1. Detailed information related to member sizes, soil conditions, and temperature variation history are available. The bridge was instrumented by Lawver et al. (2000) and Huang et al. (2004) for eight years to monitor the short- and long-term behavior when subjected to truck loadings, temperature variations, and temperature gradients.
2. The bridge is non-skewed, so this three-dimensional (3D) bridge can be idealized as a two-dimensional (2D) model because the bridge only experiences in-plane deformations. Simplifying a 3D model to 2D can greatly improve the efficiency in model construction and analysis.
3. The bridge length and the temperature variation are not large enough to induce inelastic deformation of the soil surrounding the piles so the continuum mechanics approach modified by Basu and Salgado (2008) is applicable. Based on the results from the study of Shirato et al. (2009) and Chapter 3, the elastic limits of soil are approximately 3% or 5% of the pile cross-sectional depth (d), respectively. For an HP 310x79 with d of 300 mm, these limits correspond to a maximum pile deflection of 9.2 or 15 mm. The maximum pile head deflection occurred on December 25th, 2000 when the temperature

variation was greatest. The measured pile head deflection was not reported but it can be inferred from the bridge displacement and the measured girder rotation. As presented in Appendix B, the maximum pile head deflection during eight years of monitoring is approximately 7.6 mm, which lower than either elastic limit. Thus, the behavior of the soil surrounding the pile is linear elastic and the continuum mechanics approach adapted by Basu and Salgado (2008) applies.

4.2.1 Bridge Geometry

Figure 4-1 shows the elevation of the north half of the bridge, which is symmetric about the mid-point of the interior span. It consists of three spans with a total length of 66 m.

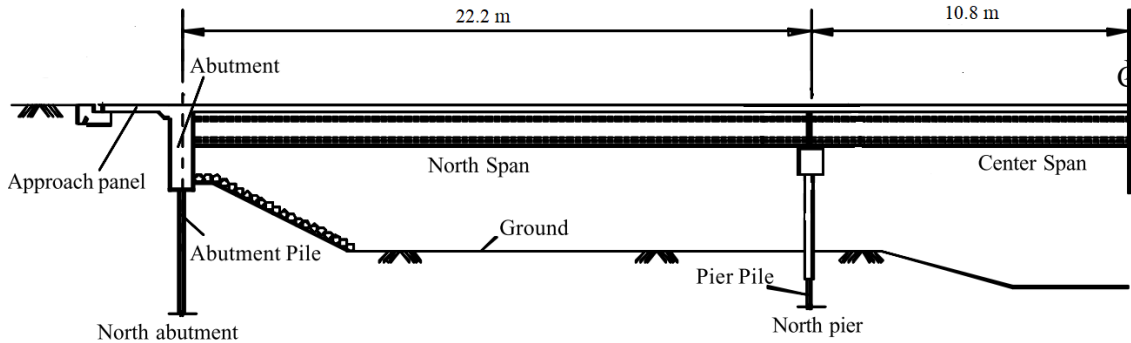


Figure 4-1: Bridge #55555 Elevation (after Huang et al. 2004)

Figure 4-2 shows the cross-section of the bridge superstructure. The total width of the bridge is 12 m, including a New Jersey barrier at each side of the deck. Each span consists of four MnDOT Type 45M precast prestressed concrete girders spaced at 3.4 m on center. The dimensions of the prestressed concrete girders are presented in Appendix C.

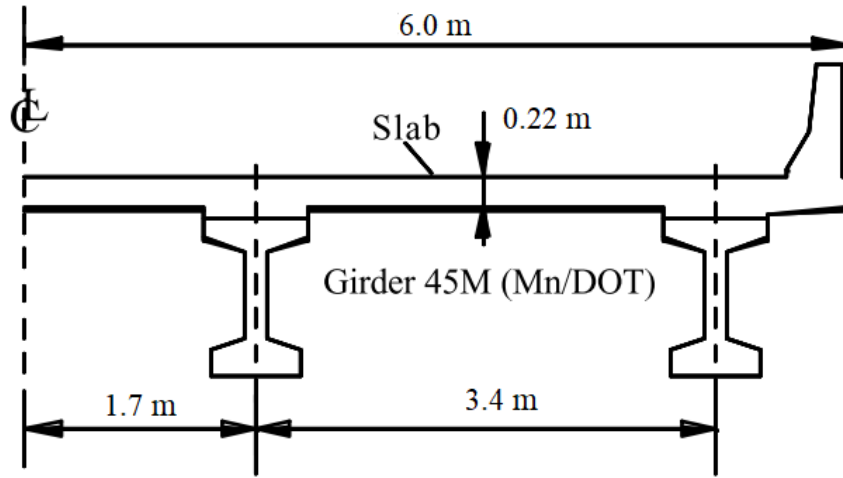


Figure 4-2: Cross-section of Superstructure (after Huang et al. 2004)

Figure 4-3 shows the connection detail at the pier. Each girder is supported by a curved plate-bearing assembly to achieve a simple support, with a 50.8 mm gap over the pier. Any continuity provided by the 220 mm thick reinforced concrete deck, which has a sawcut and V-groove over the pier, will be negligible, so the pier can be idealized as a simple support.

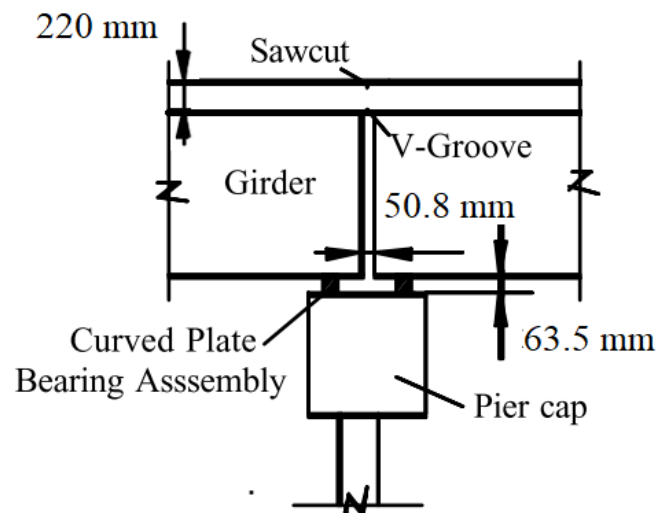


Figure 4-3: Pier Connection Detail (after Huang et al. 2004)

Figure 4-4 shows the front elevation of the abutment and piles. The reinforced concrete abutments are 12 m wide and 3 m high, supported on a single row of six 24.4 m long HP

310x79 piles. The piles are oriented to bend about their weak-axes when the bridge expands or contracts. Wingwalls, oriented at 45° in plan to the abutment centerline, retain the backfill and embankment. In the present study, the wingwalls are not included in the numerical models. Also, due to current limitations of the Basu’s software, the cross-sections of the H-piles were transformed into equivalent rectangular cross-sections with the same moment of inertia and cross-sectional depth as the H-shape cross-sections. The sizes of the transformed cross-section are as presented in Section 3.2.

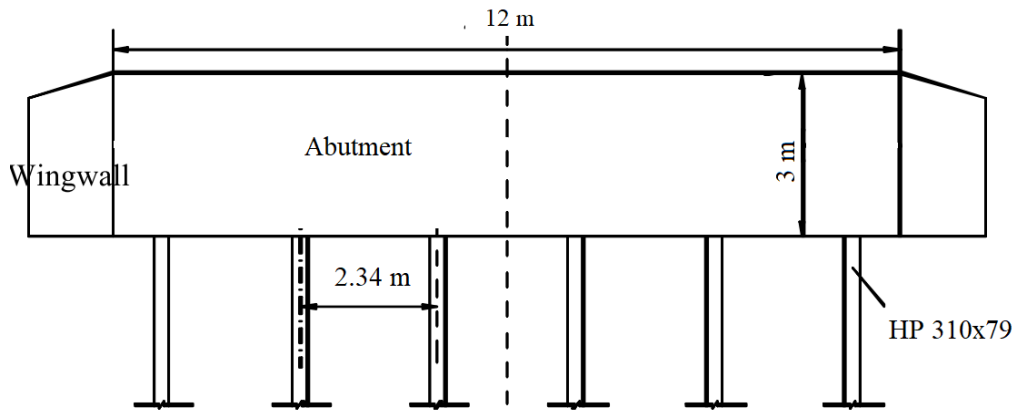


Figure 4-4: Abutment and Pile Details (after Huang et al. 2004)

4.2.2 Material Properties

The material properties of Bridge #55555 in Minnesota are shown in Table 4-1, as provided by Huang et al. (2004). These properties are used to define the numerical models in the present study. The material behavior is assumed to be linear elastic, which implies that the response of all structural components is also linear elastic.

Table 4-1: Material Properties for the SAP 2000 Models (Huang et al. 2004)

Materials	Young’s Modulus (MPa)	Coefficient of Thermal Expansion ($\mu\epsilon / ^\circ\text{C}$)
Concrete Deck	30330	11.07
Concrete	34470	11.48
Steel	200000	12.06

4.3 Integrated Analytical Procedures

In the present study, three analytical programs, SAP 2000, LPILE, and Basu's software, were used to predict the bridge response under thermally induced deformations or truck loadings. SAP 2000, a structural analysis software, was adopted to analyze the structural response of the integral abutment bridge. Due to the differences in the p-y and Basu approaches, two SAP 2000 models were constructed: one for use with LPILE and the other for use with the Basu's software. Both models use the same idealization of the bridge superstructure, piers, and abutments, but idealize the soil-pile interactions differently. The SAP 2000 model used with LPILE (SAP-LP model) idealizes the soil-pile interaction as a series of independent horizontal springs spaced vertically along the pile depth. The SAP 2000 model used with the Basu model (SAP-B model), on the other hand, idealizes the flexural and vertical rigidities of the piles and the soil-pile interaction as a set of springs, located at the base of each abutment, with stiffnesses defined by a 3x3 matrix.

Owing to the difference in the SAP 2000 models, the analytical procedures for integrating the SAP 2000 with LPILE or SAP 2000 with Basu's software were different. The procedure for the SAP-LP model is iterative, whereas the procedure for the SAP-B model is not.

4.3.1 Iterative Procedure for SAP 2000-LPILE Analysis

Figure 4-5 illustrates the procedure for determining the spring stiffnesses for the SAP 2000 model in the SAP-LP analysis. Due to the dependency between the soil stiffnesses and the lateral pile displacements, the procedure must be iterative. Initially, based on initial estimates of lateral force or shear force (V_i) and moment (M_i), the corresponding pile head lateral deflection (Δ_i) and spring stiffnesses over the pile depth were computed using LPILE. Next, these spring stiffnesses were substituted into the SAP 2000 model to generate new values of shear force and moment for subsequent input to LPILE. The iterative procedure continued until the difference in shear forces or moments between the subsequent iterations were less than 0.5% and the differences in deflection between the LPILE model and SAP 2000 model were less than 0.5%.

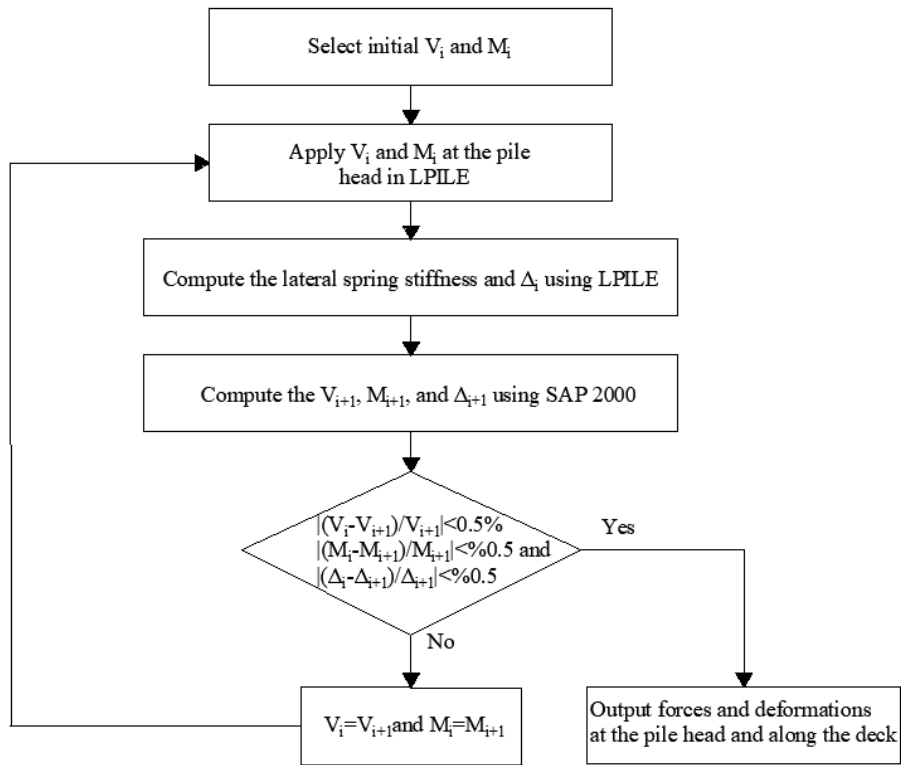


Figure 4-5: Integrated Analytical Procedure of SAP-LP Analyses

The results from LPILE represent the soil-pile stiffness and pile response of a single pile, whereas the results from the SAP 2000 model represent the total response of all the piles at one abutment. Therefore, the spring stiffness obtained from LPILE needs to be multiplied by the total number of piles underneath each abutment for substitution into the SAP 2000 model. Similarly, the pile response obtained from the SAP 2000 model needs to be divided by the total number of piles underneath each abutment before inputting into the LPILE model.

Figure 4-6 shows the right half of the 2D SAP 2000 models for the SAP-LP analyses superimposed on an outline of the elevation of the bridge. All the structural components, including the bridge deck, concrete girders, abutments, and piles, are modelled using frame elements. The four prestressed concrete girders and reinforced concrete deck properties are lumped into one horizontal frame element located at the neutral axis of the composite cross-section. The abutment is idealized as an infinitely rigid element between the neutral axis

and soffit of the superstructure because it is fully integrated with the superstructure in this region. Beneath the soffit of the superstructure, the abutment is modeled as a frame element. A similar idealization was adopted by Fennema et al. (2005). The six piles underneath each abutment are lumped into one vertical frame element with independent horizontal springs attached. For a single row of H-piles, when the pile center-to-center spacing is greater than 6.5 times the pile cross-sectional depth, any interaction between adjacent piles can be neglected (Rollins et al. 2006). Since in Bridge #55555, the pile center-to-center spacing is 7.8 times greater than the pile width, the piles are assumed to act independently. The deformations are assumed to be identical for each of the six piles, and the loads are assumed to be shared equally. The abutment-pile and deck-abutment connections are assumed to be fixed. The supports at the interior piers are idealized as pins, making the middle span simply supported.

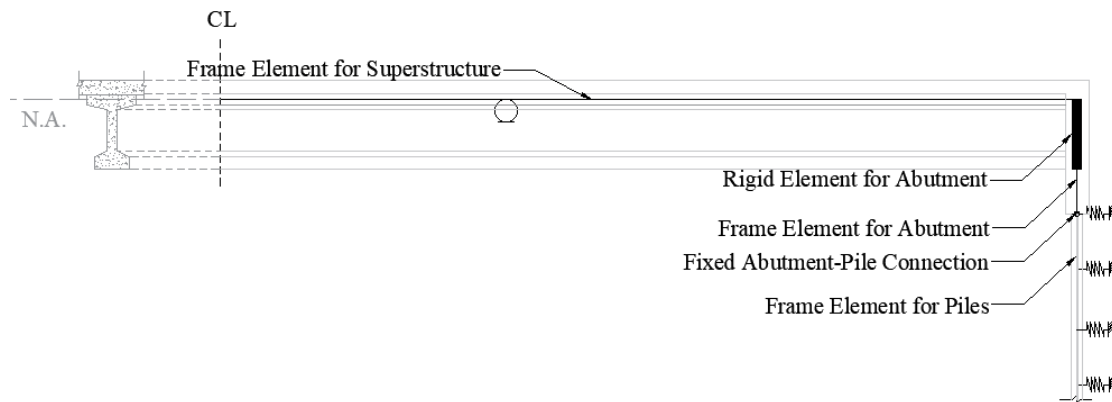


Figure 4-6: SAP 2000 Models in SAP-LP Analyses

4.3.2 Non-iterative Procedure for SAP 2000-Basu Analysis

Since the Basu analysis accounts for the interactions of adjacent soil layers at different elevations along the pile, idealizing the soil-pile interactions with independent springs along the depth is not appropriate. Instead, as shown in Figure 4-7, the soil-pile interactions at each abutment are idealized as a set of springs, located at the base of the abutment, with stiffnesses defined by a 3x3 matrix. A similar approach is adopted in a research report for the modification of Illinois Department of Transportation (IDOT) integral abutment design limitations (Olson et al. 2009). As shown in Figure 4-7, the stiffness matrix adopted in the

SAP 2000 model defines the soil-pile stiffness in vertical (z), lateral (y), and rotational (Θ) degrees of freedom. The diagonal coefficient for the pile axial stiffness (K_{zz}) is assumed to be infinite because soil settlement and pile axial deformations are neglected in the present study. The off-diagonal coefficients of the pile vertical and lateral responses (K_{zy} and K_{yz}), and the vertical and rotational responses ($K_{z\theta}$ and $K_{\theta z}$) are set to zero because there is no dependency between the pile vertical responses and lateral or rotational responses. On the other hand, the lateral and rotational responses are coupled with off-diagonal coefficients ($K_{y\theta}$ and $K_{\theta y}$) because the lateral and rotational responses are correlated: either a rotation or horizontal translation can generate a moment or shear force at the pile head. Specifically, $K_{y\theta}$ (kN/rad) is the force necessary to achieve a unit rotation as shown in Figure 3-4. Similarly, $K_{\theta y}$ (kN.m/m) is the moment required to achieve a unit deflection as shown in Figure 3-5.

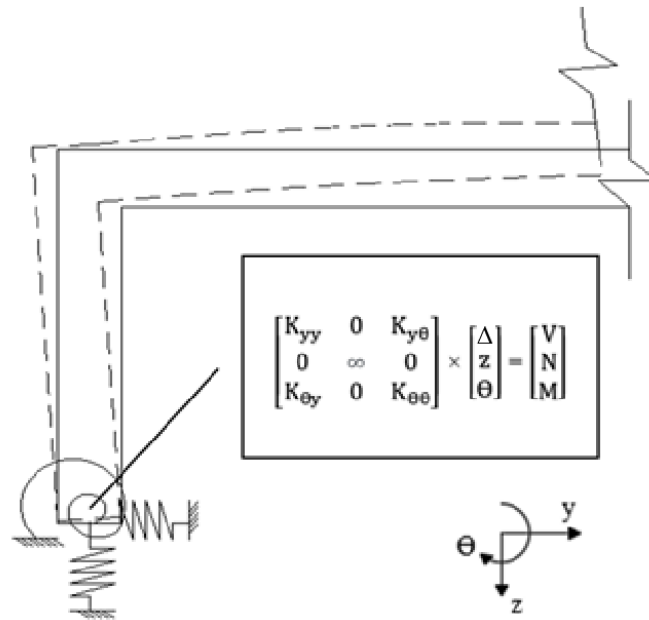


Figure 4-7: Soil-pile Interaction Modelling in SAP-B Analyses

The vertical pile response is independent of the lateral or the rotational responses, so K_{yy} , $K_{y\theta}$, $K_{\theta y}$, and $K_{\theta\theta}$ only depend on the lateral and rotational force effects and degrees of freedom. If the lateral deflections and rotations at the head of one pile due to a given

applied shear force or applied moment are known, these coefficients can be determined from:

$$\begin{bmatrix} K_{yy} & K_{y\theta} \\ K_{\theta y} & K_{\theta\theta} \end{bmatrix} = n_{eq} \times \begin{bmatrix} V_i & 0 \\ 0 & M_i \end{bmatrix} \begin{bmatrix} \Delta_v & \Delta_M \\ \theta_v & \theta_M \end{bmatrix}^{-1} \quad (4-1)$$

where: Δ_v and θ_v are the lateral deflection and rotation, respectively, at the pile head due to pile-head shear force V_i ; Δ_M and θ_M are the lateral deflection and rotation, respectively, at the pile head due to pile-head moment M_i ; and, n_{eq} is the equivalent number of piles at each abutment taking into account of the interactions between the adjacent piles. In the present study, since the pile interactions are neglected because the pile spacing is large, n_{eq} equals the actual number of piles underneath each abutment.

Assuming a positive moment generates a positive rotation at the pile head rotating the top of the pile towards the backfill and a positive shear force generates a displaces the pile head towards the backfill, the diagonal coefficients, K_{yy} and $K_{\theta\theta}$ are positive and the off-diagonal coefficients, $K_{y\theta}$ and $K_{\theta y}$ are negative and equal.

Figure 4-8 illustrates the procedure for the soil-pile interaction idealization for the SAP-B analyses. Given an initial shear force, V_i , Basu's software is used to predict pile head deflection (Δ_v) and rotation (θ_v) for a free-head pile. Similarly, for an initial moment, M_i , Basu's software is used to predict Δ_M and θ_M . The stiffness coefficients are then determined from Equation 4-1. Finally, by inputting the [K] stiffness matrix into the SAP 2000 model, the bridge responses are obtained. Since the Basu analysis treats the pile and soil as linear-elastic materials, the stiffness matrix is independent of the applied load and moment. Therefore, no iterations are required.

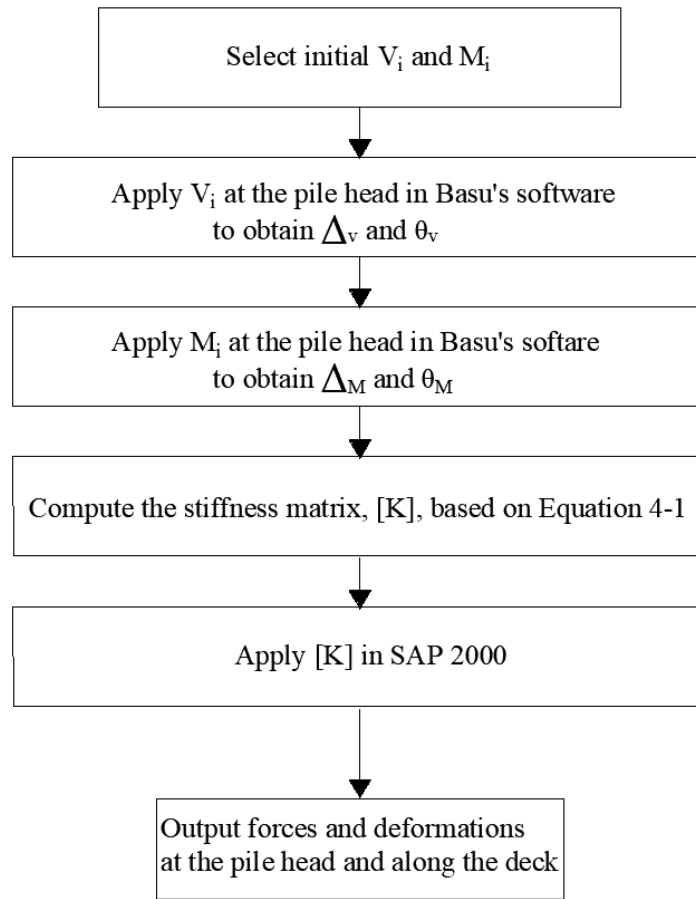


Figure 4-8: Integrated Analytical Procedure of SAP-B Analyses

Figure 4-9 shows the right half of the 2D SAP 2000 model used for the SAP-B analyses. The models are identical to those used for SAP-LP analyses, except that the piles and the pile-soil interaction are idealized by a set of springs at the pile head.

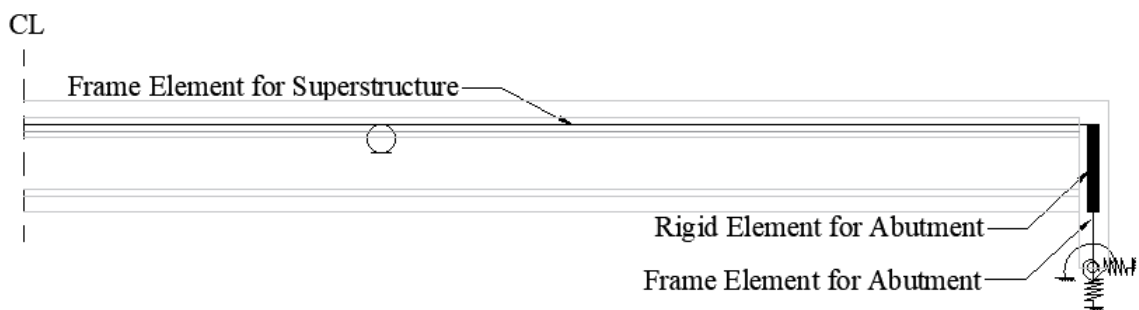


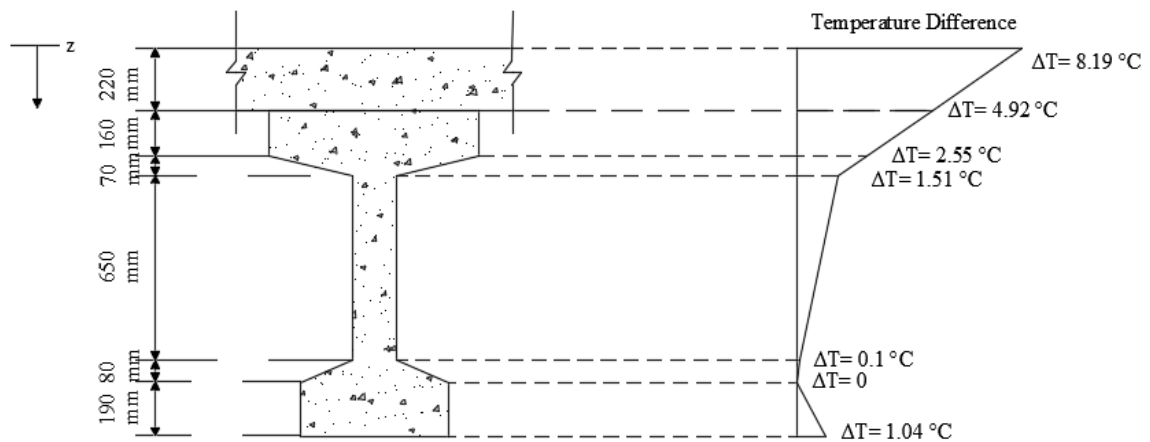
Figure 4-9: SAP 2000 Models in SAP-B Analyses

4.4 Thermally Induced Deformations and Earth Pressures Analyses

4.4.1 Maximum Temperature Variations and Gradients

During the eight years of monitoring of Bridge #55555, the highest daily average temperature of the deck, 45.0 °C, was observed on August 1st, 2001 and the lowest, -27.8 °C, was observed on December 25th, 2000. The bridge construction temperature was 12.8 °C. Therefore, the maximum temperature rise and drop considered in the current study are 32.2 °C and -40.6 °C, respectively. In the SAP 2000 models, these are applied to the frame element of the superstructure as a uniform strain distributed throughout the depth of the superstructure.

Figure 4-10 (a) shows a partial cross-section of the superstructure of Bridge #55555 and Figure 4-10 (b) shows the corresponding positive temperature gradient through the deck thickness and girder depth observed during a typical summer day at roughly 15:00 as reported by Huang et al. (2004). In the present study, only the positive temperature gradient shown in Figure 4-10 was applied to the SAP 2000 models. The negative temperature gradient was neglected because, as reported by Huang et al. (2004), it is small and so has negligible influence on the bridge response.



(a) Partial Cross-Section of Superstructure (b) Positive Temperature Gradient

Figures 4-10: Measured Positive Temperature Gradient (after Huang et al. 2004)

In SAP 2000, temperature gradients can be defined and applied to models as strain differences throughout the depth of the bridge superstructure cross-sections, but only as linear strain gradients. Therefore, in the present study, the positive temperature gradient was replaced by tensile axial force and a negative bending moment at the end of the superstructure in the SAP 2000 models to generate the same bridge deformations and final force effects in the abutment-pile system (Taly 1998).

If free movements are allowed at the ends of the superstructure, the bridge will expand when the temperature of the cross-section increases. At the same time, if a positive temperature gradient is present, the bridge superstructure will hog upwards and the ends will rotate as if equal negative moments are applied at the ends of the bridge. Therefore, to hold the cross-section in an initial zero-strain condition, a compressive axial force (F_h) and a positive bending moment (M_h) should be applied at the ends of the bridge. To release these holding forces, a tensile axial force ($-F_h$) and a negative bending moment ($-M_h$) are applied to the idealized superstructure (Figure 4-11). After the forces are released, the deformations, axial forces, shear forces, and moments in the abutment-pile system and the deformation of the superstructure can be obtained directly from the model. However, the forces in superstructure are incorrect because $-F_h$ and $-M_h$ are self-equilibrated internal forces, not external forces, in the real bridge system. To get the correct axial forces and moments of the superstructure, $-F_h$ and $-M_h$ must be subtracted from the superstructure force effects generated by the models.



Figure 4-11: Idealization of Positive Temperature Gradient in SAP 2000 Models

The magnitudes of F_h and M_h are calculated based on the geometry of the superstructure cross-section as shown in Figure 4-10 (a) and the horizontal stresses induced by the temperature gradient as shown in Figure 4-10 (b).

The horizontal tensile stress at depth z to achieve the strain induced by the positive temperature gradient is:

$$\sigma(z) = E(z)\alpha(z)\Delta T(z) \quad (4-2)$$

where:

$\sigma(z)$ is the horizontal stress at depth z (Pa);

$E(z)$ is the Young's Modulus of the superstructure cross-section at depth z (Pa);

$\alpha(z)$ is the coefficient of thermal expansion of the cross-section at depth z ($\epsilon / ^\circ\text{C}$); and

$\Delta T(z)$ is the temperature change at depth z ($^\circ\text{C}$).

To hold the cross-section in the initial zero-strain condition, a compressive axial force (F_h) is applied. The magnitude of F_h is computed by integrating the horizontal tensile stresses over the width and depth of the superstructure:

$$F_h = - \int_0^{H_s} b_s(z) \sigma(z) dz \quad (4-3)$$

where:

H_s is the depth of the superstructure (m); and

$b_s(z)$ is the width of the cross-section of the superstructure at depth z (m).

In conjunction with F_h , holding moment M_h is also needed to prevent the hogging and associated end rotation of the superstructure. The magnitude of M_h is obtained by summing the moments generated by the horizontal forces about the neutral axis of the cross-section of the superstructure.

$$M_h = - \int_0^{H_s} b_s(z) \sigma(z) (z - \bar{z}_t) dz \quad (4-4)$$

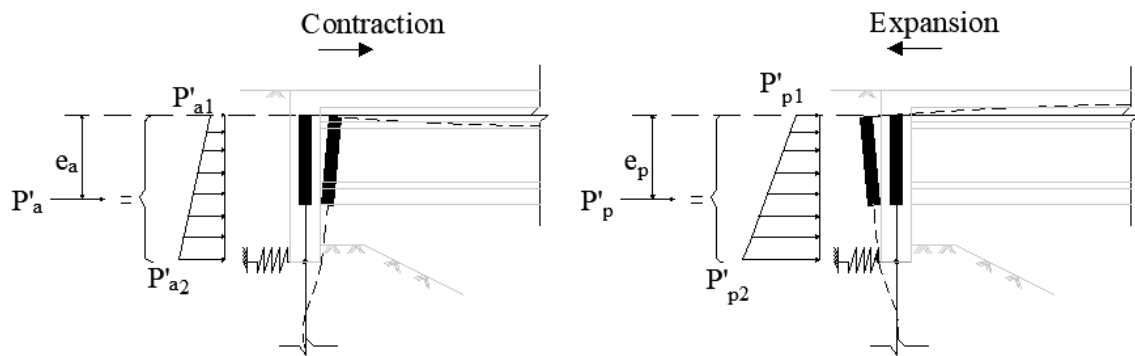
where \bar{z}_t is the distance from the bottom surface of the superstructure to the neutral axis of the cross-section.

The forces applied to the models to simulate the thermally induced movements are the same whether the LPILE or Basu soil-pile idealization are adopted. The detailed calculation of F_h and M_h is presented in Appendix D.

4.4.2 Earth Pressures

Figures 4-12(a) and (b) show the active and passive earth pressures applied to the SAP 2000 model as the bridge contracts or expands, respectively. The bridge model is again superimposed on the outline of the elevation of the bridge. These pressures can be idealized as distributed loads acting over the back face of the abutments from the neutral axis of the superstructure to the abutment soffit, with magnitudes calculated in accordance with Section C6.12.1 and Figure C6.16 of the Commentary to the Canadian Highway Bridge Design Code (CSA 2014). The magnitudes of the earth pressures partially depend on the ratio of the lateral translation at the top of the abutment and the abutment height. However, since a distributed load cannot be applied to a rigid element in SAP 2000, the earth

pressures were instead represented by an equivalent resultant force. When the bridge contracts, the resultant force due to active pressure, P'_a is applied at e_a m below the neutral axis of the superstructure and when the bridge expands, the resultant force due to passive pressure P'_p , is applied at e_p m below the neutral axis of the superstructure. In the present study, earth pressures acting on the top 0.36 m of the abutment, from the top of the abutment to the neutral axis of the superstructure, and the earth pressures acting on the river side along the bottom 0.29 m of the abutment were neglected. Detailed calculations of the magnitude and location of the equivalent force resultants are presented in Appendix E. The passive earth pressure applied when the bridge expands is approximately 38% of the full passive earth pressure, while the active earth pressure applied when the bridge contracts is the full active earth pressure.



(a) Active Pressure as Bridge Contracts (b) Passive Pressure as Bridge Expands

Figure 4-12: Earth Pressures in SAP 2000 Model Used with LPILE

4.4.3 Load Combinations

Two load combinations are considered in the analyses of thermally induced deformations. Combination A includes bridge expansion due to temperature rise, positive temperature gradient, and passive earth pressure. Combination B includes bridge contraction due to temperature drop and active earth pressure.

4.4.4 Results

4.4.4.1 Sign Convention

Figure 4-13 illustrates the sign convention adopted in this study for the force effects applied by the superstructure to the abutment. The convention used in this study is consistent with the convention used in SAP 2000 and LPILE. For the abutments and piles, a positive shear force causes a displacement towards the backfill and a positive moment rotates the top of the abutments towards the backfill. A positive axial force causes tension in the abutments and piles. A positive displacement is towards the backfill and a positive rotation rotates the top of the abutment towards the backfill. For the bridge superstructure, a positive moment causes compression in the top fibers of the superstructure and tension in the bottom fibers of the superstructure. A positive axial force causes tension in the superstructure. A positive displacement at the bridge end indicates bridge elongations and a positive rotation at the bridge end induces compression in the top fibers of the superstructure and tension in the bottom fibers.

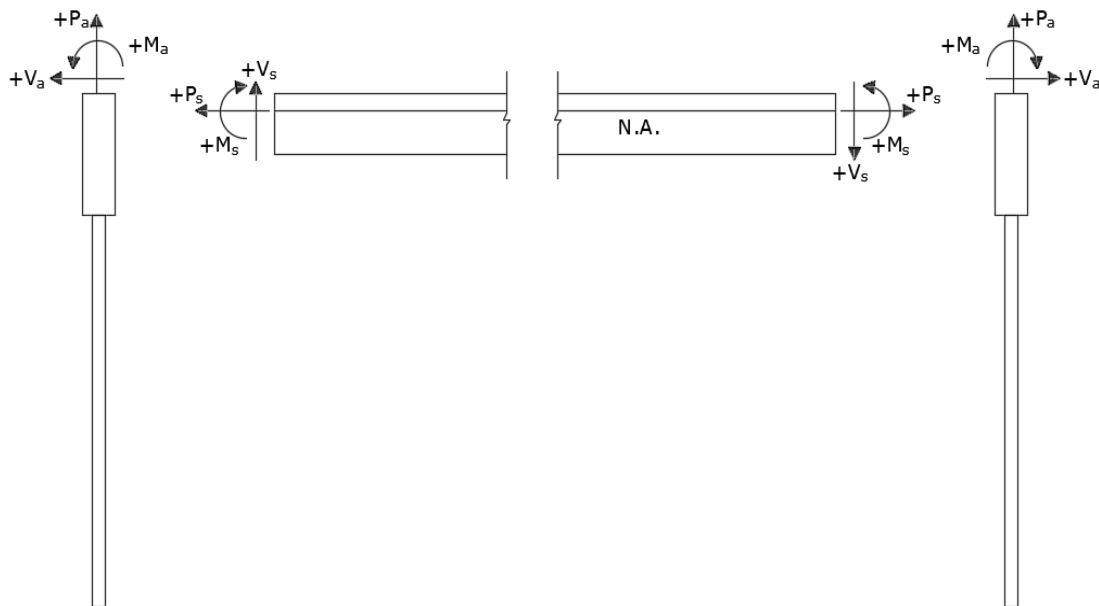


Figure 4-13: Sign Convention

4.4.4.2 Superstructure Deformations and Loads

Table 4-2 shows the lateral displacements at the end of the superstructure when the bridge expands or contracts. The variation in the soil-pile interaction idealization have negligible influence on the displacement because the axial stiffness of the superstructure is relatively large compared to the lateral stiffness of the soil-pile system.

The magnitudes of the bridge expansion and contraction are close to those computed from $\frac{1}{2}\Delta T\alpha L_s$ where ΔT is the temperature variation, α is the coefficient of thermal expansion, and L_s is the total length of the bridge. This simple calculation predicts the expansion at the ends of the superstructure to be 11.7 mm, which is 7.1% less than the average value in Table 4-2 of 12.6 mm. The positive temperature gradient induces an additional expansion of 1.6 mm, so the difference between the (11.7+1.6=) 13.3 mm expansion and the average value of 12.6 mm in Table 4-2 may be due to the passive earth pressure and pile shear force. Similarly, the simple calculation predicts a contraction of 14.8 mm, which exceeds the average value of 13.9 mm in Table 4-2 by 6.5%. As negative thermal gradients are ignored, the difference may be due to the pile shear force. It is reasonably accurate to compute the magnitudes of bridge expansion and contraction as simply $\frac{1}{2}\Delta T\alpha L_s$.

Table 4-2: Displacement at the End of the Superstructure

Analyses	Load Combination A: Expansion (mm)	Load Combination B: Contraction (mm)
SAP-LP	12.7	-14
SAP-B (B-relationship)	12.5	-13.8
SAP-B (K-Relationship)	12.6	-13.9
SAP-B (L-Relationship)	12.6	-13.9

Table 4-3 summarizes the moments at the end of the superstructure and the midspan moments of the exterior span (i.e. moments at the mid-point of the exterior spans) for the different analyses. These moments are per bridge: the moments per girder are one quarter of the values shown. The SAP-LP analysis predicts lower end and mid-span moments than the SAP-B analyses. This is consistent with the finding in Chapter 3 that the LPILE analysis

yields lower soil-pile stiffness than the Basu analyses. Therefore, when the soil-pile stiffness reduces, the bridge movements are less constrained, and hence the corresponding moments along the bridge superstructure reduce in magnitude.

Table 4-3: Bending Moments per Bridge at the End and Mid-point of the Exterior Spans

Analyses	Load Combination A: Expansion (kN.m)		Load Combination B: Contraction (kN.m)	
	End	Mid	End	Mid
SAP-LP	-5938	-2396	6025	3013
SAP-B (B-relationship)	-7554	-3233	8286	4143
SAP-B (K-Relationship)	-6944	-2898	7335	3667
SAP-B (L-Relationship)	-6803	-2828	7134	3567
Average	-6810	-2839	7195	3598

For the SAP-B analyses, as noted in Chapter 3, the B-relationship is associated with the highest lateral and rotational stiffnesses to resist rotations and translations at the head of the pile. Therefore, the moments corresponding to the B-relationship are the highest of all in the SAP-B analyses. The moments from the SAP-B analyses using soil parameters estimated using K- and L-relationships are comparable because, again as noted in Chapter 3, these relationships provide similar soil Young's moduli.

4.4.4.3 Pile Deformations and Loads

Tables 4-4(a) and (b) summarize the deformations and loads at the pile head when the bridge superstructure expands and contracts, respectively. In either case, the SAP-LP analysis predicts greater pile head deflections, slightly greater pile head moments and lower pile head rotations and shear force than the SAP-B analyses. This is again consistent with the lateral stiffness of the soil-pile system for the SAP-LP idealization being less than that for the various SAP-B idealizations.

Table 4-4(a): Deformations and Forces at the Pile Head for Bridge Expansion

Analyses	Deflection (mm)	Rotation (rad)	Shear Force (kN)	Moment (kN.m)
SAP-LP	6.4	0.0024	237	-83.0
SAP-B (B-relationship)	4.8	0.00301	336	-75.5
SAP-B (K-Relationship)	5.5	0.00268	300	-80.6
SAP-B (L-Relationship)	5.7	0.00268	291	-80.7
Average	5.6	0.00269	291	-80.0

Table 4-4(b): Deformations and Forces at the Pile Head for Bridge Contraction

Analyses	Deflection (mm)	Rotation (rad)	Shear Force (kN)	Moment (kN.m)
SAP-LP	-9.2	-0.00199	-351	145
SAP-B (B-relationship)	-6.6	-0.00292	-499	135
SAP-B (K-Relationship)	-7.5	-0.00259	-438	137
SAP-B (L-Relationship)	-7.7	-0.00252	-425	137
Average	-7.8	-0.00251	-428	139

Among the SAP-B analyses, for either bridge expansion or contraction, the lateral deflection at the pile head increases when the soil stiffnesses reduce. For example, the analysis based on the soil parameters computed using the B-relationship (Equation 3-2a) yields the lowest lateral deflections because it corresponds to the highest Young's modulus. As the lateral deflection at the end of the superstructure is essentially independent of the soil-pile idealization adopted (Table 4-2), higher lateral deflections of the pile head cause lower rotations of the abutment. However, since these deflections and rotations are insignificant in magnitude, the practical implications of these differences are small.

The SAP-B analysis based on the B-relationship has the highest soil-pile stiffnesses and so yields the highest shear force and the lowest moments. From Equation 4-1, the total shear force (V) and moment (M) of all the piles at one abutment can be computed as:

$$V=K_{yy}\Delta + K_{y\theta}\theta \quad (4-5)$$

$$M=K_{\theta y}\Delta + K_{\theta\theta}\Theta \quad (4-6)$$

where, as defined in Section 4.3.2, K_{yy} , $K_{y\theta}$, $K_{\theta y}$, and $K_{\theta\theta}$ are the coefficients in the stiffness matrix and Δ and Θ are the deflection and rotation at the pile head, respectively. For the case of bridge expansion, Figure 4-14 shows the calculations of V and M based on the stiffness matrices and pile head deformations for the SAP-B analyses using B-, K-, and L-relationships. All stiffness coefficients, and particularly K_{yy} , are greatest when the B-relationship is used. As shown in Table 4-4(a), when the soil-pile stiffness increases, Δ decreases and Θ increases, so $K_{yy}\Delta$ (positive) and $K_{y\theta}\Theta$ (negative) both increase. However, since the relative magnitude of K_{yy} markedly exceeds that of $K_{y\theta}$, the change of $K_{yy}\Delta$ more than overcomes any change in $K_{y\theta}\Theta$ and so V increases. Similarly, for moment, when the soil-stiffness increases, $K_{\theta y}\Delta$ (negative) and $K_{\theta\theta}\Theta$ (positive) increase. The associated change in $K_{\theta\theta}\Theta$ overcomes any change in $K_{\theta y}\Delta$, so M decreases. Since the changes to $K_{\theta\theta}\Theta$ and $K_{\theta y}\Delta$ are similar in magnitude, however, the change in M is relatively slight. Therefore, as the soil becomes stiffer, the shear force increases and the moment decreases slightly, so the SAP-B analysis based on the B-relationship has the highest V and lowest M.

	K_{yy}	$K_{y\theta}$	Δ	$K_{yy}\Delta$	$K_{y\theta}\Theta$	V
SAP-B (B-relationship)	$\begin{vmatrix} 5.42E+05 \\ -1.93E+05 \end{vmatrix}$	$\begin{vmatrix} -1.93E+05 \\ 1.57E+05 \end{vmatrix}$	$\begin{vmatrix} 0.0048 \\ 0.00301 \end{vmatrix}$	$\begin{vmatrix} 2601 + \\ -926 \end{vmatrix}$	$\begin{vmatrix} -580 \\ 472 \end{vmatrix}$	$\begin{vmatrix} 2021 \\ -454 \end{vmatrix}$
	$K_{\theta y}$	$K_{\theta\theta}$	Θ	$K_{\theta y}\Delta$	$K_{\theta\theta}\Theta$	M
SAP-B (K-relationship)	$\begin{vmatrix} 4.19E+05 \\ -1.68E+05 \end{vmatrix}$	$\begin{vmatrix} -1.68E+05 \\ 1.51E+05 \end{vmatrix}$	$\begin{vmatrix} 0.0055 \\ 0.00268 \end{vmatrix}$	$\begin{vmatrix} 2305 + \\ -924 \end{vmatrix}$	$\begin{vmatrix} -450 \\ 405 \end{vmatrix}$	$\begin{vmatrix} 1855 \\ -519 \end{vmatrix}$
SAP-B (L-relationship)	$\begin{vmatrix} 3.87E+05 \\ -1.58E+05 \end{vmatrix}$	$\begin{vmatrix} -1.58E+05 \\ 1.45E+05 \end{vmatrix}$	$\begin{vmatrix} 0.0057 \\ 0.00268 \end{vmatrix}$	$\begin{vmatrix} 2205 + \\ -901 \end{vmatrix}$	$\begin{vmatrix} -423 \\ 389 \end{vmatrix}$	$\begin{vmatrix} 1782 \\ -512 \end{vmatrix}$

Figure 4-14: Calculation of Shear Force and Moment at Pile Head

In addition, for this specific case, the difference between the SAP-B analyses and SAP-LP analysis in shear forces and moments are approximately within 23%-42% and 3%-9%,

respectively, when the bridge expands. When the bridge contracts, the ranges are 21%-43% for shear forces and 4%-7% for moments. This implies, for this case, the shear forces are more sensitive to the soil-pile interaction idealization than the moments at the pile head. The shear capacity of an HP 310x79 can be computed as $0.66\phi_s A_w F_y$, where ϕ_s is the resistance factor for steel, A_w is the cross-sectional area of the web, and F_y is the yield strength of the pile (CSA 2014). Based on the properties and sizes of the pile, the shear capacity of an HP 310x79 is approximately 454 kN. Therefore, the difference in the predicted shear force between the idealizations may affect the design of the pile.

Figure 4-15 shows the variation of the pile curvatures measured between August 1st, 1996 and August 1st, 2004 (Huang, et al. 2011). The “Row A” and “Row B” labels indicate the location of the strain gauges at 0.1 m and 0.9 m below the pile head, respectively. In the present study, the strains at Row A are taken to be the strains at the pile head. The pile curvature is also clearly influenced by both daily and seasonal temperature variations. Since the temperature variations applied to the numerical models are calculated based on the average daily temperatures, to be consistent, the measured pile curvature should be taken as the average pile curvature on a given day. Therefore, the pile curvatures measured on August 1st, 2001 and December 25, 2000 equal approximately 3.54 $\mu\epsilon/\text{mm}$ and 6.25 $\mu\epsilon/\text{mm}$, respectively, which correspond to pile head moments of 37.5 kN.m and 66.2 kN.m, respectively. The calculation of the moments inferred from the measured pile curvature are presented in Appendix F and the locations of the instrumentation are summarized in Appendix G.

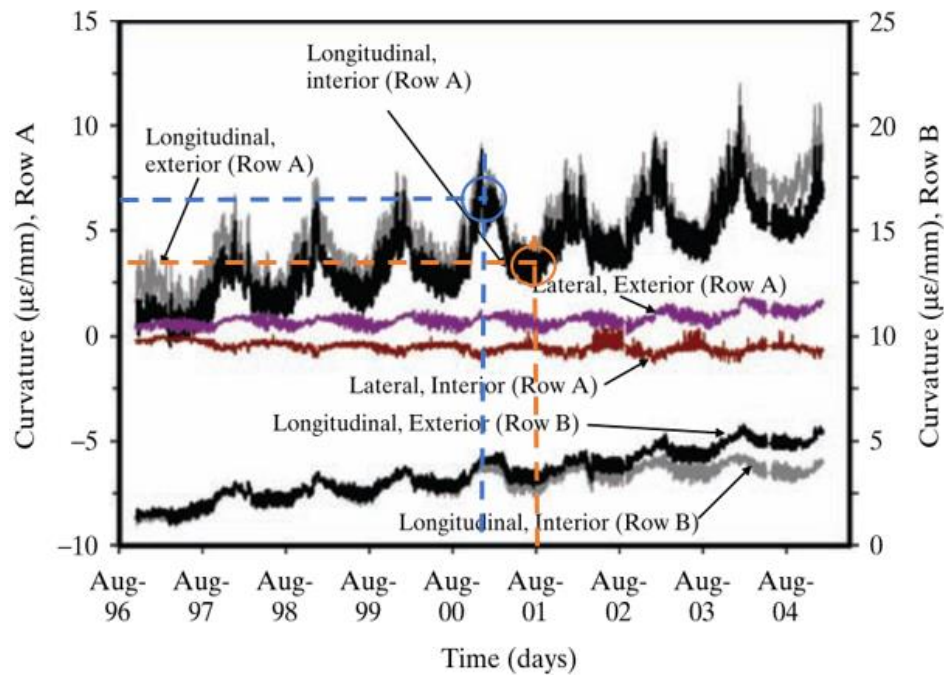


Figure 4-15: Pile Curvatures (Huang et al. 2011)

The moment inferred from the measured curvature has the opposite sense to that predicted from the SAP-LP and SAP-B analyses when the bridge expands. The moments predicted in the SAP analyses in the present study are markedly higher than those inferred from the measured pile curvature, by factors of approximately 2.13 and 2.10 for the cases of bridge expansion and contraction, respectively. A possible explanation for these differences is that the measured values are influenced by the long-term effects, including creep of the prestressed concrete girder and shrinkage of the concrete deck. As discussed in Chapter 2, the temperature rise, negative temperature gradient, and shrinkage cause a decrease in the pile curvature and moment, whereas the temperature drop, positive temperature gradient, and creep cause an increase in the pile curvature and moment. During the eight years of the monitoring period, the shrinkage effect decreases while the creep effects increases (Huang et al. 2011). Therefore, when the creep effect dominates, the inferred moments may be higher than the predicted moments because the long-term effects are not included in the predicted moments.

As reported by Huang et al. (2011) the total time-dependent change in the longitudinal pile curvature at Row A between August 1st 1996 to August 1st 2004 is approximately 4.5 $\mu\epsilon/\text{mm}$. Assuming the permanent pile curvature steadily increases, the time-dependent change in the longitudinal pile curvature at Row A is, by interpolation, approximately 2.81 $\mu\epsilon/\text{mm}$ until August 1st, 2001 and 2.43 $\mu\epsilon/\text{mm}$ until December 25, 2000. Therefore, the short-term pile curvatures are approximately 0.73 $\mu\epsilon/\text{mm}$ and 3.44 $\mu\epsilon/\text{mm}$ corresponding to pile head moments of 7.72 kN.m and 36.4 kN.m, for the cases of expansion and contraction, respectively. Compared to the values shown in Tables 4-4(a) and (b), the moment inferred from Figure 4-16 for the case of expansion is still of the opposite sense and lower in magnitude than those predicted by the SAP-LP and SAP-B analyses.

The following are possible explanations for the difference between the pile head moments inferred from the measured pile curvatures, Figure 4-16 and those predicted from the numerical analyses, Tables 4-4 (a) and (b):

- As noted by Huang et al. (2004), the soil subgrade reaction moduli used in the analytical models may be much stiffer than those for the real soil conditions at the bridge site.
- The pile curvatures were not measured exactly at the pile head, but 0.1 m below the pile head. From the SAP-LP analysis, when the bridge expands, the moments at the pile head and 0.1 m below the pile are approximately -83.0 and -61.4 kN.m, respectively, a decrease of 26.0% within 0.1 m. Therefore, the actual difference is less than implied by the discussion above.

Based on the computed moments shown in Tables 4-4 (a) and (b), the maximum pile stresses exceed the nominal yield stress when combined with the axial force due to the self-weight of the bridge. Assuming a linear elastic response, the maximum compressive stresses are 258 and 441 MPa when the bridge expands and contracts, respectively, which exceed the nominal yield stress of 250 MPa. This violates the assumption of a linear-elastic pile response. However, the shear forces have high magnitudes at the pile head and are of the sense that reduces the pile moments, so the yielding region is localized. From the SAP

2000 analyses, the pile axial force due to the self-weight of the bridge is approximately 261 kN per pile, so yielding occurs when the magnitude of the weak-axis moment exceeds 78 kN.m. Based on the bending moment diagrams from SAP-LP analysis, when the bridge expands and contracts, only the top 0.024 and 0.20 m of the pile yields, respectively, and only locally at the flange tips (i.e., the free edges of the flanges) that are in compression. Therefore, the equivalent secant rigidity of the pile is likely close to the product of the elastic modulus of steel and weak-axis moment of inertia, as listed in Table 4-1. Hence, in this case, idealizing the pile response as linearly elastic is valid. The bending moment diagram of the pile is presented in Appendix H.

4.5 Truck Loading

4.5.1 Truck Tests (Lawver et al. 2000)

Truck tests were also conducted by Lawver et al. (2000) on Bridge #55555 with a single Minnesota Department of Transportation (MnDOT) sand truck. The tests were conducted statically because the vibration due to the moving truck led to fluctuations of measurements. Therefore, as shown in Figure 4-16, the truck was placed at 23 different positions across the length of the bridge deck. The interior girder moments were measured at Points A and B on Figure 4-16, where Point A is at the face of the abutment, 1 m from the pile centerline and Point B is located 12 m from the vertical centerline of the piles. Although Points A and B are not exactly at the end and mid-point of the exterior span, the moments at these two locations are taken in the present study to be the support moment and midspan moment, respectively. The maximum moments at Points A and B were recorded.(Lawver et al. 2000).

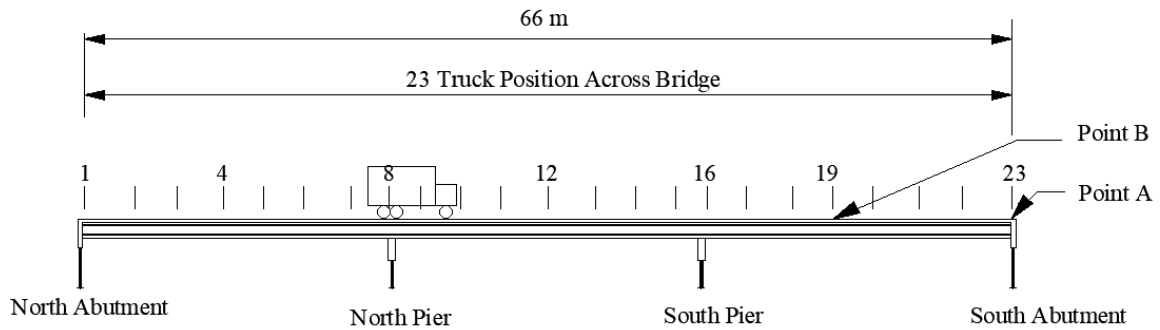


Figure 4-16: Truck Positions (after Lawver et al. 2000)

4.5.2 Truck Loading

Figure 4-17 illustrates the axle loads and spacings for the MnDOT sand truck as reported by Huang et al. (2004). It is not immediately clear, however, whether the 157 kN weight is for the tandem axle or for a single axle of the tandem. Minnesota regulations limit the maximum weight on a tandem axle to be 34 kips, or 151 kN, and the maximum weight on a single axle to be 20 kips, or 89.0 kN (Minnesota Department of Transportation 2005). Therefore, if 157 kN is for the tandem axle, the axle is 4% over the legal limits, whereas if 157 kN is for a single axle of the tandem, the axle is 108% over the legal limits. It is therefore assumed in the present study that the weight of 157 kN is for the tandem axle and so the total weight of the truck is 215 kN.

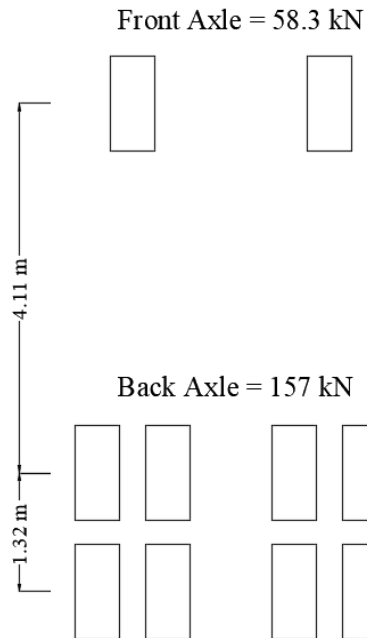


Figure 4-17: MnDOT Sand Truck (after Huang et al. 2004)

To determine the lateral distribution factor for an interior girder, the measured values of the average support moment (i.e. moment at the support) and the midspan moment (i.e. moment at the mid-point of the span) were summed. Equilibrium requires that this sum equals the midspan moment of a simply supported beam with the truck placed in the same location. So a 22 m simply supported beam was analyzed for the truck using the multi-step static load feature of SAP 2000, and the maximum truck moment was obtained. The lateral distribution factor for the interior girder was computed as the ratio between the observed total moment value and the computed simple span moment value, yielding a value of 0.375. The instrumented interior girder was therefore assigned 37.5% of the total moment due to the truck loading.

4.5.2 Results

Table 4-5 summarizes the measured and computed moments for a single interior girder at Points A (end of the exterior span) and Point B (mid-point of the exterior span). The average of the end moment (i.e. moments at the end of the exterior span) computed by the SAP-LP and SAP-B analyses is approximately -35.8 kN.m. Assuming the interior girder

carries 35% of the truck loading, the total end moment caused by the truck is -102 kN.m . Compared with the average moments induced by the temperature variations, temperature gradient, and soil pressures, -6810 kN.m as the bridge expands and 7195 kN.m as the bridge contracts, this total truck moment is insignificant. Therefore, even though the SAP-LP and SAP-B analyses underestimate the measured bridge end moment by 40% to 67%, the design of the superstructure in this region is unlikely to be affected. On the other hand, the average of the midspan moment computed by the four analyses for an interior girder is approximately 411 kN.m. Assuming the girder carries 35% of the truck loading, the bridge is subjected to 881 kN.m in total at the mid-point of the exterior span. Compared to the averaged midspan moment summarized in Table 4-3, this is approximately 31% of the moments induced by temperature variations and earth pressures, so the superstructure design is more sensitive to the truck loading case. However, since the SAP-LP and SAP-B analyses provide slightly conservative estimates of the measured midspan moment, the soil-pile interaction idealizations are appropriate for the analysis of integral abutment bridge response subjected to truck loading.

Table 4-5: Measured and Computed Moments for Interior Girder of Exterior Span

Analyses	M_A (kN.m)	M_B (kN.m)
SAP-LP	-27.3	313
SAP-B (B-relationship)	-38	307
SAP-B (K-Relationship)	-40	307
SAP-B (L-Relationship)	-38	307
Simply Supported Span (Lawver et al. 2000)	46	366
Fixed-Pinned Span (Lawver et al. 2000)	-251	227
Measured	-81	285

In addition, as shown in Table 4-5, the results from the simplified analyses of Lawver et al. (2000) bound the field measured values, but neither bounds accurately represents the actual bridge responses. Assuming the measured moments to be accurate, the assumption of a simple support at the abutment causes the moment at Point A to have the wrong sense

and overestimates the midspan moment at Point B by approximately 28%. These observations are consistent with the effect of ignoring any rotational restraint caused by the integral abutment. The assumption of a fixed support at the abutment, on the other hand, markedly overestimates the negative moment at the end of the bridge superstructure by 210% and underestimates the associated midspan moment by 29%. Therefore, these two simplified models are not recommended for the estimation of bridge superstructure moments due to the applied truck loading.

4.6 Summary and Conclusions

This chapter presents the influence of different soil-pile interaction idealizations on the prediction of deformations and force effects of an integral abutment bridge subjected to temperature variations, temperature gradients and corresponding earth pressures. A 2D model of Bridge #55555 in Minnesota, instrumented by others, is created using SAP 2000. The model was integrated with two different soil-pile interaction analyses: the LPILE analysis (SAP-LP) and the Basu analysis (SAP-B). As in Chapter 3, the SAP-B analyses are conducted based on soil Young's moduli estimated using the Biot (B-), Kishida (K-), and Lashkaripour (L-) relationships. The responses are quantified using the lateral deflections, rotations, moments and shear force at the pile head and the lateral displacement, rotation, moment and shear force at the end of the superstructure. This chapter also presents the influence of soil-pile interactions on the responses of the bridge subjected to truck loading. Besides the SAP-LP and SAP-B analyses, the responses are also approximated with simplified models that idealize the bridge exterior span as simply supported or fixed at the abutment. The computed superstructure moments are compared with those from the simplified models and field measurements.

The conclusions of this chapter are as follows:

1. The longitudinal displacement at the end of the superstructure due to thermal expansion or contraction is insensitive to the soil-pile idealization because the axial stiffness of the superstructure is relatively large compared to the lateral stiffness of the soil-pile system. For a symmetrical bridge with identical soil conditions at the abutments, it can

be approximated as $\frac{1}{2}\Delta T\alpha L_s$ where ΔT is the temperature variation, α is the coefficient of expansion, and L_s is the total length of the bridge.

2. When the bridge expands or contracts due to combinations of temperature variations, temperature gradients, and earth pressures, the SAP-LP analysis yields lower moments in the superstructure, higher lateral deflections and moments and lower rotations at the pile head compared to the SAP-B analyses. The difference between the SAP-B analyses and SAP-LP analysis in shear forces and moments are approximately within 23%-42% and 3%-9%, respectively, when the bridge expands. When the bridge contracts, the ranges are 21%-42% for shear forces and 4%-7% for moments. These differences are attributable to the different soil stiffness parameters associated with the p-y (LPILE) and continuum (Basu) approaches and are consistent with the findings reported for a single pile in Chapter 3. In particular, for the Basu analyses:

- the soil-pile stiffnesses estimated using the Biot (B-) relationship are the greatest and so the moments at the end of the superstructure are the greatest, the lateral deflections at the pile head are the least, and the rotation at the pile head are the greatest.
- The soil-pile stiffnesses estimated using the Kishida (K-) and Lashkaripour (L-) relationships are similar, so the lateral deflections, rotations and force effects in the bridge superstructure and piles from these analyses are also similar.

3. When the integral abutment bridge is subjected to truck loading, the SAP-LP and SAP-B analyses yield a conservative moment at the mid-point of the exterior span but an unconservative moment at the end of the bridge. However, since the truck-load moment at the end of the bridge is very small compared to the moment induced by the temperature variation, earth pressure, and temperature gradient, for design purposes any of these analyses are appropriate for predicting the moments at both locations.

4. When the integral abutment bridge is subjected to truck loading, idealizing the span/abutment connection as a simple support yields a bridge end moment of the wrong

sense and a conservative midspan moment. Idealizing this connection as a fixed support markedly underestimates the midspan moment and excessively overestimates the end moment. Therefore, these simplified idealizations are not recommended to determine the superstructure moments in this bridge due to sand truck loading.

Chapter 5

5 Parametric Study of Integral Abutment Bridges

5.1 Objectives of Research Presented in this Chapter

- Since thermal movements of integral abutment bridges are accommodated at the abutments and piles, the response depends on the bridge geometry, member stiffnesses, and soil parameters. As described in Chapter 2, extensive parametric studies by others have investigated the influence of these variables on the behavior of integral abutment bridges subjected to thermally induced deformations (Huang et al. 2008; Kong et al. 2016; Quinn and Civjan 2017). However, most of these studies are numerical analyses that cannot provide insight knowledge on the fundamental relationship between the various design parameters, such as force equilibrium and compatibility of the system. Therefore, the research reported in this chapter will: Derive fundamental equilibrium and compatibility equations to quantify the response in the integral abutment region.
- Confirm the adequacy and applicability of these equations using finite element models based on the continuum mechanics approach modified by Basu and Salgado (2008) for bridges with different geometries, member stiffnesses, and soil parameters.
- Apply these equations to gain a fundamentals-based understanding of the response of the integral abutment region.

In addition, as described in Chapter 4, different soil-pile interaction idealizations lead to different responses for the specific integral abutment bridge investigated. However, the influence of the soil-pile interaction idealization on the response of bridges with different structural configurations and soil properties has not been studied. Therefore, the research reported in this chapter will also:

- Conduct a parametric study to investigate how the soil-pile interaction idealizations affect the deformations and restraint force effects on bridges with various geometries, stiffnesses, and soil parameters using finite element models based on

the p-y (Reese et al. 1974; Matlock 1970) and continuum (Basu and Salgado 2008) approaches.

This sensitivity analysis will focus on the responses of integral abutment bridges subjected to positive uniform temperature variations, positive temperature gradients, and the corresponding passive earth pressures. Cases involving bridge contractions are not investigated because the soil-pile interaction has very similar but opposite effects on the bridge response as the direction of the bridge movement reverses. Therefore, the findings reported in this chapter also apply to bridges subjected to thermal contractions.

5.2 Mechanics-based Bridge Responses

The statically indeterminate integral abutment region can be idealized as shown in Figure 5-1, where the simplified model is superimposed on an outline of the bridge components. The abutment is idealized as a rigid body from its soffit to the neutral axis of the superstructure. The superstructure is idealized as a frame element with a flexural stiffness of K_s and axial stiffness of k_s connect to the top of the rigid body. The axial, lateral, and rotational stiffnesses of the soil-pile system are represented as a stiffness matrix $[K]$, as described in Section 4.3.2, at the abutment soffit. The matrix coefficients can be calculated following the procedure described in Section 4.3.2 and illustrated in Figure 4-8.

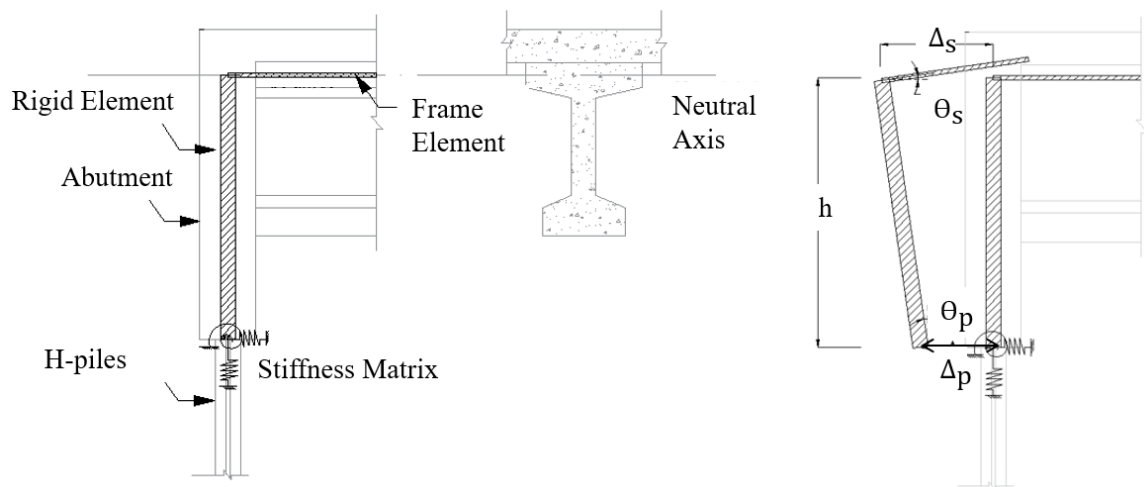


Figure 5-1: Simplified Integral Abutment

The response of this idealized model can be determined analytically using mechanics-based equations of equilibrium and compatibility. Figures 5-2(a) and (b) show the deflections and the free body diagram of the idealized integral abutment, respectively, as the bridge expands. The sign conventions for the force effects and deflections are as shown in Figure 4-13. Since the abutment is rigid, the rotations at the pile head (Θ_p) and at the end of the superstructure (Θ_s) must equal the rotation of the abutment (Θ_a) given by:

$$\Theta_a = \frac{\Delta_s - \Delta_p}{h} \quad (5-1)$$

where Δ_s and Δ_p are the horizontal displacements at the end of the superstructure and at the pile head, respectively, induced by the temperature variation, temperature gradient, and earth pressure, and h the vertical distance between the neutral axis of the superstructure and the soffit of the abutment.

For a linear elastic response, the moment at the end of the superstructure (M_s) is:

$$M_s = K_s(\Theta_s - \Theta_{st}) \quad (5-2)$$

where K_s is the flexural stiffness of the superstructure, Θ_s is the rotation at the end of the superstructure due to temperature variation, temperature gradient, and earth pressure, and Θ_{st} is the rotation at the end of the unrestrained superstructure due to temperature variation and temperature gradient only. Similarly, the axial force at the end of the superstructure (N_s) satisfies:

$$N_s = k_s(\Delta_{st} - \Delta_s) \quad (5-3)$$

where k_s is the axial stiffness of the superstructure, Δ_s is the lateral displacement at the end of the superstructure due to temperature variation, temperature gradient, and earth pressure, and Δ_{st} is the lateral displacement at the end of the unrestrained superstructure due to temperature variation and temperature gradient only.

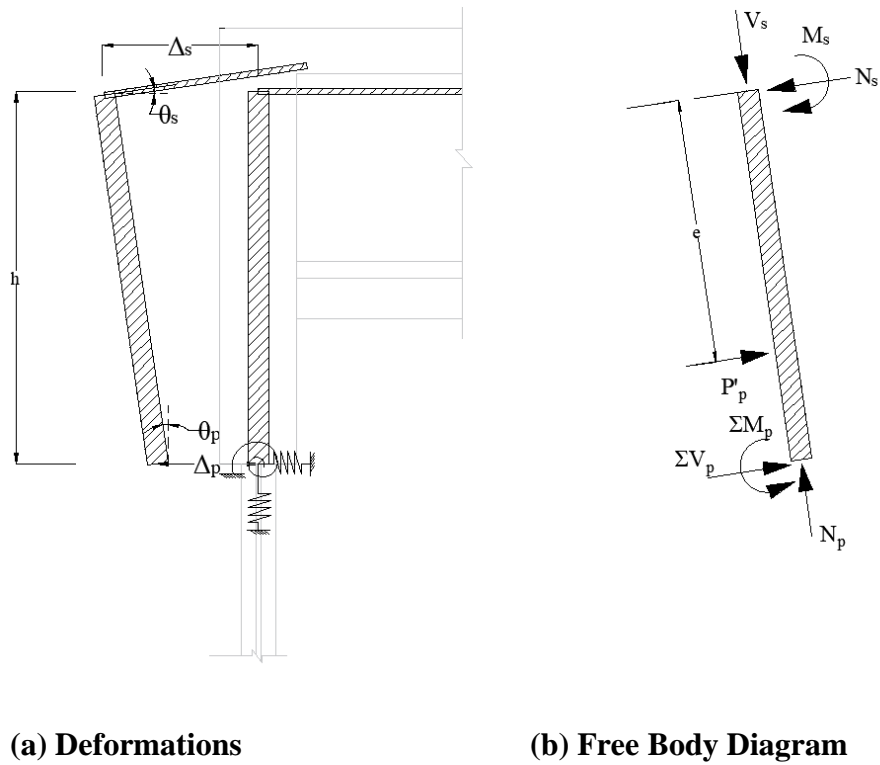


Figure 5-2: Deformations and Free Body Diagram of the Simplified Model

Vertical force equilibrium requires that:

$$N_p = V_s + W_a \quad (5-4)$$

where N_p is the axial force applied to the head of the pile, V_s is the shear force at the end of the superstructure, and W_a is the weight of the abutment. Similarly, horizontal force equilibrium, requires that:

$$N_s = P'_p + \Sigma V_p \quad (5-5)$$

where P'_p is the resultant of the earth pressures, located a distance (e_p) from the neutral axis of the superstructure, and ΣV_p , is the total shear force at the heads of all piles beneath one abutment. Finally, moment equilibrium about the point where the neutral axis of the superstructure intersects the vertical axis of the abutment requires:

$$M_s = -\Sigma V_p h + \Sigma M_p - P'_p e_p \quad (5-6)$$

where ΣM_p is the total moment at the heads of all piles beneath one abutment. As described in Section 4.3.2, ΣM_p and ΣV_p can be determined from Δ_p , Θ_a , and the coefficients in the stiffness matrix (K_{yy} , $K_{y\theta}$, $K_{\theta y}$, and $K_{\theta\theta}$) representing the soil-pile system as:

$$\Sigma M_p = K_{\theta y} \Delta_p + K_{\theta\theta} \Theta_a \quad (5-7)$$

$$\Sigma V_p = K_{yy} \Delta_p + K_{y\theta} \Theta_a \quad (5-8)$$

Substitution of Equations 5-2, 5-7 and 5-8 into Equation 5-6, yields:

$$\Delta_p \left[-K_{yy}h + 2K_{y\theta} - \frac{K_{\theta\theta}}{h} - \frac{K_s}{h} \right] + \Delta_s \left[-K_{y\theta} + \frac{K_{\theta\theta}}{h} + \frac{K_s}{h} \right] = P'_p e_p + K_s \Theta_{st} \quad (5-9)$$

If Δ_s , Θ_{st} , K_{yy} , $K_{y\theta}$, $K_{\theta\theta}$, K_s , P'_p , e_p , and h are known, the lateral pile head deflection (Δ_p) can be computed by rearranging Equation 5-9 as:

$$\Delta_p = \frac{-\Delta_s \left[-K_{y\theta} + \frac{K_{\theta\theta}}{h} + \frac{K_s}{h} \right] + P'_p e_p + K_s \Theta_{st}}{-K_{yy}h + 2K_{y\theta} - \frac{K_{\theta\theta}}{h} - \frac{K_s}{h}} \quad (5-9a)$$

Then Θ_a can be determined using Equation 5-1, the force effects in the pile can be determined from Equations 5-7 and 5-8 and the force effects in the superstructure can be determined from Equation 5-5 and 5-6.

5.2.1 Validation of Equations

The bridge deformations and load effects obtained from the SAP-B analyses can be used to verify Equations 5-1 to 5-9a. Tables 5-1 (a) and (b) compare the deformations and load effects, respectively, at the pile head and at the end of the superstructure obtained from these independent procedures. For consistency with the assumption used to derive Equations 5-1 to 5-9a, the abutment is idealized in the SAP-B analysis as rigid from its soffit to the neutral axis of the superstructure. The results are essentially identical, confirming the validity of Equations 5-1 to 5-9a.

Table 5-1(a): Deformations at the Pile Head and the End of the Superstructure for Case 1 (Fully Rigid Abutment)

	SAP-B		Eq. 5-9(a)	SAP-B		Eq. 5-1
	Δ_p (mm)	Δ_s (mm)	Δ_p (mm)	Θ_p (rad)	Θ_s (rad)	Θ_a (rad)
B-	4.8	12.5	4.9	0.0029	0.0029	0.0029
K-	5.5	12.6	5.4	0.0027	0.0027	0.0027
L-	5.6	12.6	5.6	0.0026	0.0026	0.0026

Table 5-1(b): Load Effects at the Pile Head and the End of the Superstructure for Case 1 (Fully Rigid Abutment)

	ΣM_p (kN.m)		ΣV_p (kN)		N_s (kN)		M_s (kN.m)	
	SAP-B	Eq. 5-7	SAP-B	Eq. 5-8	SAP-B	Eq. 5-5	SAP-B	Eq. 5-6
B-	-482	-483	2067	2068	3140	3140	-7727	-7729
K-	-493	-494	1805	1806	2878	2878	-7045	-7048
L-	-494	-495	1750	1752	2823	2824	-6902	-6906

Tables 5-2 (a) and (b) repeat the comparison for the case where the abutment is idealized in the SAP-B analysis as rigid only from the neutral axis of the superstructure to the soffit of the girder. In this case Equations 5-1 to 5-9a yield comparable results to those obtained from the SAP-B analysis, with slightly higher load effects at the pile head and superstructure end, and a lower displacement at the pile head. However, the maximum difference for the pile deflection is 2.1%, and the maximum force effects are only slightly overestimated. The SAP-B results in Tables 5-1 and 5-2 are almost identical, suggesting that the abutment beneath the girder soffit acts essentially as a rigid body. Equations 5-1 to 5-9a can therefore be used to estimate the responses of integral abutment bridges, and to check the results of numerical models.

Table 5-2(a): Deformations at the Pile Head and the End of the Superstructure for Case 1 (Partially Rigid Abutment)

	SAP-B		Eq. 5-9(a)	SAP-B		Eq. 5-1
	Δ_p (mm)	Δ_s (mm)	Δ_p (mm)	Θ_p (rad)	Θ_s (rad)	Θ_a (rad)
B-	4.8	12.5	4.9	0.0030	0.0028	0.0029
K-	5.5	12.6	5.4	0.0028	0.0026	0.0027
L-	5.7	12.6	5.6	0.0027	0.0026	0.0026

Table 5-2(b): Load Effects at the Pile Head and the End of the Superstructure for Case 1 (Partially Rigid Abutment)

	ΣM_p (kN.m)		ΣV_p (kN)		N_s (kN)		M_s (kN.m)	
	SAP-B	Eq. 5-7	SAP-B	Eq. 5-8	SAP-B	Eq. 5-5	SAP-B	Eq. 5-6
B-	-453	-469	2013	2036	3086	3108	-7554	-7630
K-	-467	-519	1760	1853	2833	2925	-6901	-7199
L-	-468	-501	1708	1746	2781	2818	-6763	-6898

5.3 Parameters Investigated in Parametric Study

As is clear from the derivation of Equations 5-6 to 5-9a, the key variables that control the thermally induced response include: the superstructure longitudinal displacement (Δ_s); the pile head lateral deflection (Δ_p); the abutment rotation (Θ_a); the vertical distance between the neutral axis and soffit of the superstructure (h); the passive soil resultant force (P'_p) and location of the line of action (e_p) of the passive earth pressure; the superstructure flexural stiffness (K_s); and soil-pile spring stiffnesses located at the abutment soffit (K_{yy} , $K_{y\theta}$, and $K_{\theta\theta}$). These quantities are influenced by design variables such as: (1) the total bridge length, which influences Δ_s and P'_p ; (2) the superstructure flexural stiffness; and, (3) the abutment height which influences h , e_p , and P'_p . These quantities also depend on foundation-related variables that influence K_{yy} , $K_{y\theta}$, and $K_{\theta\theta}$ including: (4) the pile stiffness (and so orientation); (5) the pile-soil surface area; (6) the soil properties; and, (7) the presence of a sleeve around the head of the pile. Therefore, these seven variables were selected as input parameters for the parametric study.

Table 5-3 shows the corresponding cases investigated in the current parametric study. The bridge investigated in Chapter 4, Bridge #55555 in Minnesota (Huang et al. 2004) was used as the base case (Case 1). Ten other models were analyzed to investigate the influence of the seven variables investigated.

Table 5-3: Variables and Cases for the Parametric Study

Case	Bridge Length (m)	Superstructure Stiffnesses (kN/m or kN.m/rad)	Abutment Height	Pile Design	Soil
1	66	k_s and K_s	3 m	6-HP310x79 (weak)	4 layers
2	132	k_s and K_s	3 m	6-HP310x79 (weak)	4 layers
3	66	$2k_s$ and $2K_s$	3 m	6-HP310x79 (weak)	4 layers
4	66	k_s and K_s	5 m	6-HP310x79 (weak)	4 layers
5	66	k_s and K_s	7 m	6-HP310x79 (weak)	4 layers
6	66	k_s and K_s	3 m	6-HP310x79 (strong)	4 layers
7	66	k_s and K_s	3 m	4-HP310x110 (strong)	4 layers
8	66	k_s and K_s	3 m	6-HP310x79 (weak)	uniform loose sand
9	66	k_s and K_s	3 m	6-HP310x79 (weak)	uniform dense sand
10	66	k_s and K_s	3 m	6-HP310x79 (weak)	very loose sand for top 3 m (sleeve filled with loose material)
11	66	k_s and K_s	3 m	6-HP310x79 (weak)	very dense sand for top 3 m (sleeve filled with compacted material)

Case 2 focuses on the influence of superstructure displacement (Δ_s) on the response of integral abutment bridges. As shown in Equation 5-9a, increasing Δ_s increases the lateral deflection at the pile head, and so, from Equations 5-7 and 5-8, the shear force and moment at the pile head also increase. The total bridge length was increased from 66 m in Case 1 to 132 m in Case 2 to investigate the effect of essentially doubling Δ_s .

Case 3 focuses on the influence of superstructure flexural stiffness (K_s) on the response. The rotational stiffness K_s is proportional to $E_c I_s / L_{es}$, where E_c is Young's Modulus of the

superstructure, I_s is the moment of inertia of the composite superstructure cross-section, and L_{es} is the end span length. It is increased from 1.01×10^6 kN.m/rad to 2.02×10^6 kN.m/rad by doubling E_c . Doubling E_c also doubles k_s quantified as $E_c A_s / L_{es}$, where A_s is the area of the superstructure cross section, from 6.03×10^6 to 12.1×10^6 kN/m.

Cases 4 and 5 focus on the influence of three variables related to the abutment height: vertical distance between the neutral axis of the superstructure and the soffit of the abutment (h), resultant force of the earth pressures (P'_p), and vertical distance between neutral axis of superstructure and the resultant force of earth pressures (e_p). Increasing the abutment height increases each of these quantities. Equations 5-5, 5-6, and 5-9a indicate that changes in h , P'_p , and e_p influence the axial force and moment at the end of the superstructure, N_s and M_s , and the deflection at the pile head, Δ_p , respectively. In this study, abutment heights of 3 (Case 1), 5 (Case 4), and 7 m (Case 5) were investigated to represent realistic short, intermediate, and tall abutment heights.

Case 6 focuses on the influence of pile orientation, and consequently the pile stiffness, on the response. Changing the pile orientation from weak- to strong-axis bending increases the magnitudes of all coefficients in the stiffness matrix (K_{yy} , $K_{y\theta}$, and $K_{\theta\theta}$), and so, from Equations 5-7, 5-8, and 5-9a, the moment, shear force, and deflection at the pile head. In the present study, the pile orientation was changed from weak-axis bending (Case 1) to strong-axis bending (Case 6), which increases the moment of inertia of the pile cross-section from 5.26×10^7 mm⁴ to 16.3×10^7 mm⁴, and so increases the stiffness matrix coefficients by a factor of approximately 3.1.

Case 7 is considered in the context of Case 6 to investigate the influence of the pile surface area on the coefficients in the soil-pile stiffness matrix, and so on the response. This area, shown shaded in Figure 5-3, is simply bL , where b is the width of the cross-section bearing against the soil and L is the length of the pile. Increasing the pile surface area increases the soil resistance to lateral pile deflections and so increases stiffness coefficients K_{yy} , $K_{y\theta}$, and $K_{\theta\theta}$, influencing Δ_p (Equation 5-9a), ΣM_p (Equations 5-7), ΣV_p (Equation 5-8), and consequently, M_s (Equation 5-6). As shown in Figure 5-3, the six HP310x79 piles bending

about their strong axes (Case 6) are replaced with four HP 310x110 piles bending about their strong axes (Case 7). The center-to-center spacings between the piles goes from 2.34 m (S_1) to 3.90 m (S_2). The combined moments of inertia for all piles at one abutment are approximately equal: $97.8 \times 10^7 \text{ mm}^4$ and $94.8 \times 10^7 \text{ mm}^4$ for Cases 6 and 7, respectively. Similarly, the combined cross-sectional areas of for all piles at one abutment are also approximately equal: $5.99 \times 10^4 \text{ mm}^2$ and $5.64 \times 10^4 \text{ mm}^2$ for Cases 6 and 7, respectively. The pile designs in Cases 6 and 7 are therefore similar: they have the same lateral stiffness and the same areas to resist axial loads. The cross-sectional depths for each pile are also similar: 305 mm for HP310x79 (Case 6) and 310 mm for HP310x110 (Case 7). Thus, the pile surface area of six HP310x79 (Case 6) is $4.45 \times 10^7 \text{ mm}^2$, which is 47.7% greater than that of four HP310x110, $3.02 \times 10^7 \text{ mm}^2$ (Case 7)

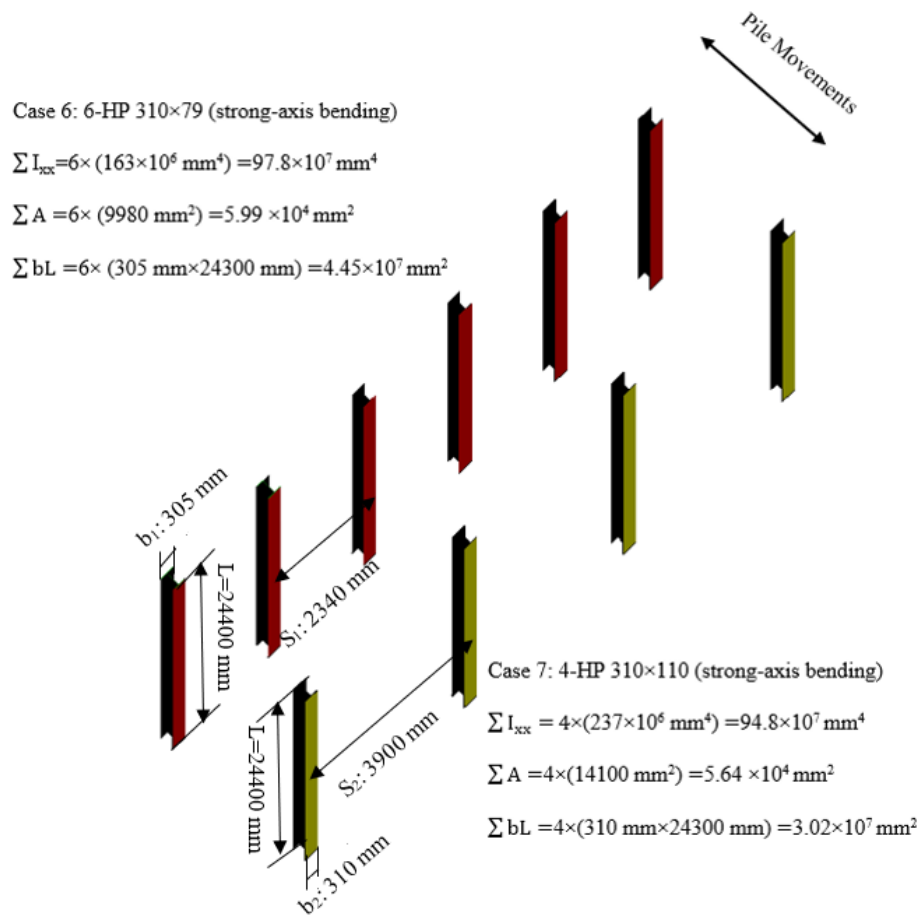


Figure 5-3: Illustration of Piles in Cases 6 and 7

Cases 8 and 9 focus on the influence of the soil properties, and so the soil-pile stiffness and associated coefficients in the stiffness matrix (K_{yy} , $K_{y\theta}$, and $K_{\theta\theta}$) on the response. The parameters expected to be sensitive to changes of the soil properties are Δ_p (Equation 5-9a), ΣM_p (Equation 5-7), ΣV_p (Equation 5-8), and consequently, M_s (Equation 5-6). Here the four layer soil profile (Case 1) is changed to uniform loose sand with effective unit weight of 17.5 kN/m^3 and friction angle of 30° (Case 8) and dense sand with effective unit weight of 20 kN/m^3 and friction angle 36° (Case 9), which are both expected to yield higher soil-pile stiffnesses than Case 1, because the soft clay in Case 1 is less stiff than either the loose or dense sand.

Cases 10 and 11 focus on the influence of any pile sleeves present, which again affects the soil-pile stiffness and associated coefficients in the stiffness matrix (K_{yy} , $K_{y\theta}$, and $K_{\theta\theta}$) as described for Cases 8 and 9. In Cases 10 and 11, it is assumed that a sleeve filled with very loose sand is present around the top 3 m of the pile. It is common practice to assume that sleeved piles are laterally unconstrained in the sleeved region. Russell (2016) conducted a set of field load tests, compared the results with those obtained from numerical analyses, and concluded that even loose fill can provide significant resistance to lateral the pile deflections. Therefore, the sleeve effects typically assumed in design are idealized as the pile being embedded in very loose with effective unit weight of 15 kN/m^3 and friction angle of 30° (Case 10) and Russell (2016) found that compaction had occurred in some sleeves due to the cyclic thermal movements of the integral abutments. Therefore, very dense sand with effective unit weight of 22 kN/m^3 and friction angle 40° (Case 11) in the sleeved region.

The bridge response in the parametric study is quantified using the variables defined in Equations 5-1 to 5-9a. Specifically these are: the axial force (N_s), moment (M_s), longitudinal displacement (Δ_s), and rotation (Θ_s) at the end of the superstructure; and the shear force (ΣV_p), moment (ΣM_p), displacement (Δ_p), and rotation (Θ_p) at the pile head.

5.4 Parametric Study Results

Each case investigated in the parametric study comprises four analyses: a SAP-LP analysis and three SAP-B analyses conducted based on soil parameters estimated using the B- (Equation 3-2b), K- (Equation 3-4a), and L- (Equation 3-6) relationships. The equations derived in Section 5.2 are applied to explain analytically the influence of different bridge variables on the deformations and the load effects at the pile head and end of the superstructure.

5.4.1 Effect of Bridge Length

Tables 5-4(a) and (b) summarize lateral deflections and rotations, respectively, at the pile head and the end of the superstructure, for the bridges with lengths of 66 m (Case 1) and 132 m (Case 2). When the bridge length doubles, the displacements at the end of the superstructure and pile head also approximately double. The Δ_s value from the SAP-B (B-relationship) analysis increases by approximately 90% because while the free expansion due to the temperature variation is doubled for the longer bridge, the greater end deflection causes greater passive earth pressures and pile shear forces that restrain this deformation. The θ_p and θ_s values from the SAP-B (B-relationship) analysis increase by approximately 70% and 71%, respectively, because greater passive earth pressure and pile shear forces cause greater abutment rotation. For the greater deflections at the end of the superstructure and greater abutment rotations, Δ_p can be estimated using Equation 5-1. The Δ_p value from the SAP-B (B-relationship) analysis increases by approximately 104%.

Table 5-4(a): Displacements at the Pile Head and the End of the Superstructure Obtained from SAP 2000 Analyses for Cases 1 and 2

Case	Δ_p (mm)				Δ_s (mm)			
	LP	B-	K-	L-	LP	B-	K-	L-
1	6.4	4.8	5.5	5.7	12.6	12.5	12.6	12.6
2	13.9	9.8	11.4	11.7	24.5	23.7	23.9	24

**Table 5-4(b): Rotations at the Pile Head and the End of the Superstructure
Obtained from SAP 2000 Analyses for Cases 1 and 2**

Case	Θ_p (rad)				Θ_s (rad)			
	LP	B-	K-	L-	LP	B-	K-	L-
1	0.0024	0.0030	0.0027	0.0027	0.0023	0.0028	0.0026	0.0026
2	0.0042	0.0051	0.0050	0.0049	0.0039	0.0048	0.0047	0.0046

Similar to the results from Chapter 4, the SAP-LP analysis yields greater deflection and lower rotation at the pile head than the SAP-B analyses. These differences increase as the bridge length increases because the pile head deflection of 13.9 mm from the SAP-LP analysis exceeds the elastic limit of 9.15 mm as determined in Chapter 3. As the SAP-LP analysis accounts for possible plastic behavior of soil, whereas the SAP-B analysis does not, it will predict relatively more lateral pile head deflections for the longer bridge. The greater pile head deflections cause lesser abutment rotations, from Equation 5-1.

Tables 5-5(a) and (b) summarize the moments and shear forces at each pile head and the moments and axial forces at the superstructure ends, respectively, for the two bridge lengths. Again, the force effect magnitudes approximately double when the bridge length doubles.

**Table 5-5(a): Moments and Shear Forces at the Head of Each Pile
Obtained from SAP 2000 for Cases 1 and 2**

Case	M_p per pile (kN.m/pile)				V_p per pile (kN/pile)			
	LP	B-	K-	L-	LP	B-	K-	L-
1	-83.0	-75.5	-80.6	-80.7	235	336	300	291
2	-189	-172	-183	-184	453	707	637	621

**Table 5-5(b): Moments and Axial Forces at the End of the Superstructure
Obtained from SAP 2000 for Cases 1 and 2**

Case	M_s (kN.m)				N_s (kN)			
	LP	B-	K-	L-	LP	B-	K-	L-
1	-5938	-7554	-6944	-6803	2502	3086	2895	2841
2	-10635	-14556	-13293	-13002	4115	5640	5223	5074

These force effects shown in Tables 5-5(a) and 5-5(b) can be reproduced almost exactly using Equations 5-5 to 5-8 with the lateral deflections and pile rotations tabulated in Tables 5-4(a) and 5-4(b).

As shown in Table 5-5(a), the SAP-B analyses yield higher shear forces and lower moments at the pile head than the SAP-LP analysis. As concluded in Chapter 3, the SAP-B analyses are associated with greater soil stiffnesses than SAP-LP analysis. This implies if the soil response is linear elastic, the SAP-LP analyses will yield lower soil-pile stiffness coefficients than the SAP-B analyses. Equation 5-7 indicates that the shear forces at the pile head the sum of the shear forces induced by the pile head deflection ($K_{yy}\Delta_p$) and rotation ($K_{y\theta}\Theta_a$), which counteract. The influence of K_{yy} is markedly greater than $K_{y\theta}$, so the stiffer soil in the SAP-B analyses cause greater shear forces. Similarly, Equation 5-8 indicates that the total pile head moment is the sum of those induced by the pile head deflection ($K_{\theta y}\Delta_p$) and rotation ($K_{\theta\theta}\Theta_a$). In this case, the effect of $K_{\theta y}$ is opposite to that of $K_{\theta\theta}$. In the SAP-B analyses, the magnitudes of $K_{\theta y}\Delta_p$ and $K_{\theta\theta}\Theta_a$ are similar, so the SAP-B analyses yields smaller moment at the pile head than the SAP-LP analysis.

Table 5-6 presents the maximum extreme fiber compressive stress at the pile head, computed using the SAP-B analysis (B-relationship), due to the dead load reaction of the abutment and superstructure and the pile head moment from Table 5-4(a). The total stress in both cases exceeds the nominal yield stress of 250 MPa, and hence the assumption of a linear-elastic pile response is violated. However, as discussed previously, the shear forces at the pile head are large and of the sense that reduces the pile moments, so the yielding region is localized. Based on the pile bending moment diagrams, yielding is confined to only the top 0.01 or 0.22 m of the piles for Cases 1 or 2, respectively. The equivalent secant rigidity of the pile is therefore likely close to the product of the elastic modulus of steel and weak-axis moment of inertia, so the assumption of linear-elastic pile stands. Detailed calculations of extreme fibre pile stresses for Cases 1 to 11 are presented in Appendix J. Any yielding regions present are localized within the top 0.25 m of the pile, so the assumption of a linear-elastic pile response is approximately valid in all cases.

Table 5-6: Maximum Pile Compressive Stresses at the Pile Head for Cases 1 and 2

Case	Axial Stress (MPa)	Flexural Stress (MPa)	Total Compressive Stress (MPa)
1	-26.8	-231	-258
2	-26.8	-491	-518

5.4.2 Effect of Superstructure Stiffnesses

Tables 5-7 (a) and (b) present the lateral deflections at the pile head and end of the superstructure, respectively, for bridges with rotational stiffness ($E_c I_s / L_s$) of 1.01×10^6 kN.m/rad (Case 1) and 2.02×10^6 kN.m/rad (Case 3), and axial stiffness ($E_c A_s / L_s$) of 6.03×10^6 kN/m (Case 1) and 12.1×10^6 kN/m (Case 3). The displacements at the end of the superstructure are similar for the two cases because: (1) the axial stiffness of the superstructure dominates and, (2) the passive earth pressures constraining the displacement are similar. As the superstructure stiffnesses double, abutment rotations decrease. Hence, from Equation 5-1, the deflection at the pile head must increase when Δ_s remains essentially constant and θ_a reduces. Again, the SAP-LP analysis yields greater deflection and lower rotation at the pile head than the SAP-B analyses.

Table 5-7(a): Displacements at the Pile Head and at the End of the Superstructure Obtained from SAP 2000 Analyses for Cases 1 and 3

Case	Δ_p (mm)				Δ_s (mm)			
	LP	B-	K-	L-	LP	B-	K-	L-
1	6.4	4.8	5.5	5.7	12.6	12.5	12.6	12.6
3	8.2	6.7	7.4	7.5	12.9	12.7	12.8	12.8

Table 5-7(b): Rotations at the Pile Head and the End of the Superstructure Obtained from SAP 2000 Analyses for Cases 1 and 3

Case	θ_p (rad)				θ_s (rad)			
	LP	B-	K-	L-	LP	B-	K-	L-
1	0.0025	0.0030	0.0028	0.0027	0.0023	0.0028	0.0026	0.0026
3	0.0019	0.0025	0.0022	0.0021	0.0017	0.0022	0.0019	0.0019

Tables 5-8 (a) and (b) summarize the load effects at the pile head and end of the superstructure, respectively, for Cases 1 and 3. The force effects shown in Tables 5-8(a) and 5-8(b) can be reproduced almost exactly using Equations 5-5 to 5-8 with the lateral deflections and pile rotations tabulated in Tables 5-7.

**Table 5-8(a): Moments and Shear Forces at the Head of Each Pile
Obtained from SAP 2000 Analyses for Cases 1 and 3**

Case	M _p per pile (kN.m/pile)				V _p per pile (kN/pile)			
	LP	B-	K-	L-	LP	B-	K-	L-
1	-80.7	-75.5	-77.9	-78.0	230	336	293	285
3	-132	-151	-144	-142	322	524	440	423

**Table 5-8(b): Moments and Axial Forces at the End of the Superstructure
Obtained from SAP 2000 for Cases 1 and 3**

Case	M _s (kN.m)				N _s (kN)			
	LP	B-	K-	L-	LP	B-	K-	L-
1	-5915	-7554	-6901	-6763	2453	3086	2833	2841
3	-7676	-10990	-9619	-9343	2958	4216	3714	3613

5.4.3 Effect of Abutment Height

Figure 5-3 shows the deflected shape of the abutment and pile for abutment heights of 3 m (Cases 1), 5 m (Case 4), and 7 m (Case 5) as obtained from the SAP-LP analysis. Positive deflections corresponding to deflections towards the backfill. The horizontal dotted line shows the elevation of the pile head, at the abutment soffit, so the deflections shown above this line are for the abutment and those below are for the pile. The maximum deflections in all cases occur at the elevation of the neutral axis of the superstructure and have nearly identical magnitudes. The rotations of the abutment, which are severely exaggerated because of the axis units selected, are also independent of the abutment height. As a result, the deflection at the pile head decreases from approximately 4.8 to -1.4 mm when the abutment height increases from 3 to 7 m.

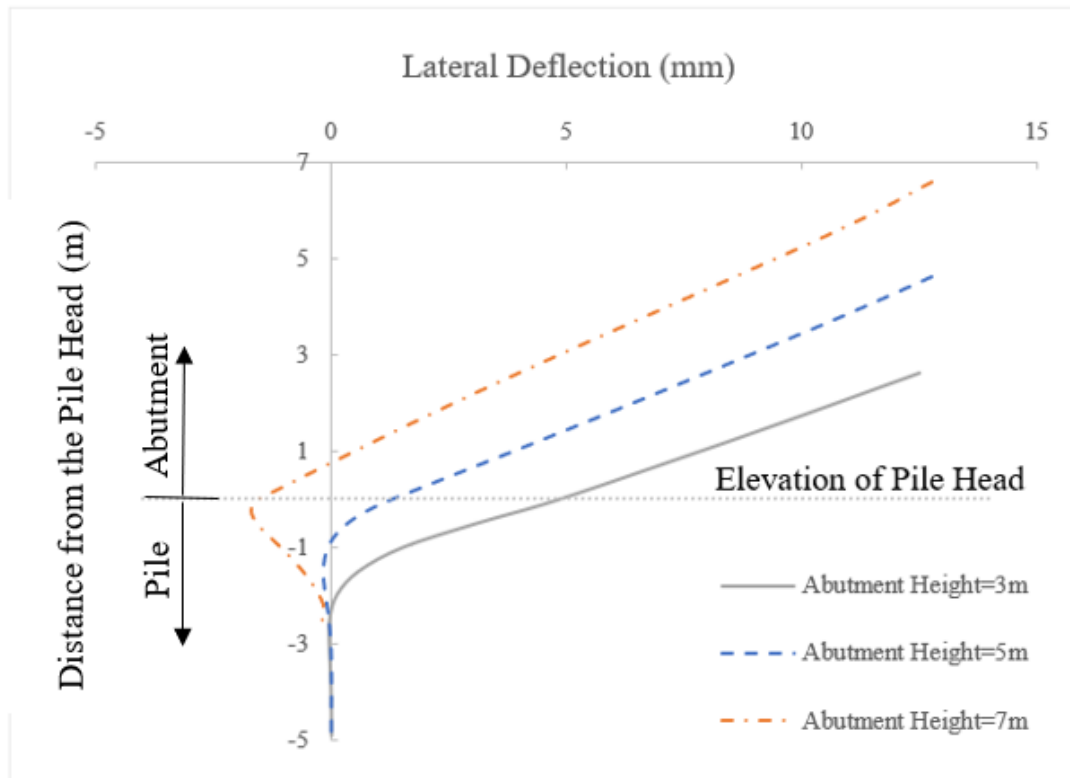


Figure 5-4: Lateral Deflection of Abutment and Pile

Table 5-9 summarizes the load effects at the pile head of each pile for Cases 1, 4, and 5 as the abutment height increases from 3 m, 5m, to 7m. Based on Equations 5-7 and 5-8, the moment and shear force at the pile head are dependent on Δ_p and Θ_p , so with a smaller Δ_p and a constant Θ_p , the moment at the pile head increases and the shear force at the pile head decreases.

**Table 5-9: Moments and Shear Forces at the Head of Each Pile
Obtained from SAP 2000 Analyses for Cases 1, 4, and 5**

Case	M_p per pile (kN.m)				V_p per pile (kN)			
	LP	B-	K-	L-	LP	B-	K-	L-
1	-83.0	-75.5	-77.9	-80.7	235	336	293	291
4	16.6	23.7	20.0	19.3	26.0	38.2	34.0	33.2
5	102	94.5	97.7	98.3	-173	-186	-180	-179

Table 5-10 summarizes the moments and axial forces at the end of the superstructure for the different abutment heights. The variation of M_s with the abutment height differs for the

SAP-LP and SAP-B analyses. When the abutment height increases from 5 m to 7 m, M_s increases from 5705 to 5815 kN.m in the SAP-LP analysis but decreases from 6001 to 5366 kN.m in the SAP-B analysis (B-relationship).

Table 5-10: Moments and Axial Forces at the End of the Superstructure Obtained from SAP 2000 Analyses for Cases 1, 4, and 5

Case	M_s (kN.m)				N_s (kN)			
	LP	B-	K-	L-	LP	B-	K-	L-
1	-5938	-7554	-6901	-6763	2502	3086	2833	2841
4	-5705	-6001	-5909	-5888	1856	1929	1904	1899
5	-5815	-5366	-5542	-5589	2044	1968	2000	2008

This difference can be explained analytically using Equation 5-6. Table 5-11 quantifies each term in Equation 5-6 using the values obtained from the corresponding SAP-LP and SAP-B (B-relationship) analyses. The moment at the end of the superstructure depends on the moments due to the shear force at the pile head ($V_p h$) and the equivalent earth pressure ($P'_p e_p$). As the abutment height increases, $V_p h$ becomes more positive while $P'_p e_p$ becomes more negative. Since the SAP-B analyses yields greater shear force at the pile (Table 5-9), the reduction of the moment induced by the shear force at the pile head exceeds the increase in the moment due to the equivalent earth pressure. Thus, when the abutment height increases from 5 m to 7 m, the magnitude of moment at the end of the superstructure decreases in the SAP-B analyses and increases in the SAP-LP analysis.

Table 5-11: Computed Moments at the End of the Superstructure Based on Results Obtained from SAP 2000 for Case 1, 4, and 5

Case	SAP-LP				SAP-B (B-relationship)			
	$-V_p h$ (kN.m)	M_p (kN.m)	$-e_p$ (kN.m)	M_s (kN.m)	$-V_p h$ (kN.m)	M_p (kN.m)	$-P'_p e_p$ (kN.m)	M_s (kN.m)
1	-3643	-484	-1785	-5912	-5314	-453	-1785	-7552
4	-725	99.5	-5078	-5704	-1063	142	-5078	-5999
5	6892	610	-13314	-5812	7397	567	-13314	-5350

5.4.4 Effect of Pile Stiffness

Tables 5-12 (a) and (b) present the deflections and rotations, respectively, at the pile head and the end of the superstructure when the piles are orientated to bend about their weak-

(Case 1) or strong- (Case 6) axes. The effects are similar for both analyses: for example, for the SAP-B (B-relationship) analysis, Δ_s and Δ_p decrease by approximately 6.3% and 0.8%, respectively, and Θ_p and Θ_s increase by approximately 3.3% and 7.1%, respectively, for the strong-axis bending case. The change in the pile stiffness has negligible effect on the displacement at the end of the superstructure because the axial stiffness of the superstructure is relatively large compared to the lateral stiffness of the soil-pile system. As noted previously, the SAP-LP analysis yields greater Δ_p , so as the Δ_s are similar, it yields lower Θ_p and Θ_s than the SAP-B analyses.

Table 5-12(a): Displacements at the Pile Head and the End of the Superstructure Obtained from SAP 2000 Analyses for Cases 1 and 6

Case	Δ_p (mm)				Δ_s (mm)			
	LP	B-	K-	L-	LP	B-	K-	L-
1	6.4	4.8	5.5	5.6	12.6	12.5	12.6	12.6
6	6.2	4.5	5.2	5.4	12.6	12.4	12.5	12.5

Table 5-12(b): Rotations at the Pile Head and the End of the Superstructure Obtained from SAP 2000 Analyses for Cases 1 and 6

Case	Θ_p (rad)				Θ_s (rad)			
	LP	B-	K-	L-	LP	B-	K-	L-
1	0.0025	0.0030	0.0028	0.0027	0.0023	0.0028	0.0026	0.0026
6	0.0026	0.0031	0.0029	0.0028	0.0024	0.0030	0.0028	0.0027

Tables 5-13 (a) and (b) summarize the load effects at the pile head and at the end of the superstructure, respectively, for the different pile orientations. As the pile flexural stiffness increases, these load effects generally increase, but the moment at the pile head from the SAP-B analyses decreases. As discussed in Section 5.4.2 and 5.4.3, as the lateral stiffness of the soil-pile system increase, the moment at the pile head from the SAP-B analyses may increase or decrease depending on the magnitude of the stiffness coefficients and the deformations at the pile head.

**Table 5-13(a): Moments and Shear Forces at the Head of Each Pile
Obtained from SAP 2000 Analyses for Cases 1 and 6**

Case	M _p per pile (kN.m/pile)				V _p per pile (kN/pile)			
	LP	B-	K-	L-	LP	B-	K-	L-
1	-80.7	-75.5	-77.9	-78.0	230	336	293	285
6	-88.3	-62.0	-74.8	-75.0	250	374	328	308

**Table 5-13(b): Moments and Axial Forces at the End of the Superstructure
Obtained from SAP 2000 Analyses for Cases 1 and 6**

Case	M _s (kN.m)				N _s (kN)			
	LP	B-	K-	L-	LP	B-	K-	L-
1	-5915	-7554	-6901	-6763	2453	3086	2833	2841
6	-6205	-7979	-7339	-7062	2593	3338	3061	2944

5.4.5 Effect of Pile Surface Area

Tables 5-14 (a) and (b) present the deflections and rotations, respectively, at the pile head and the end of the superstructure when the pile surface area is reduced from $4.46 \times 10^5 \text{ mm}^2$ (Case 6) to $3.02 \times 10^5 \text{ mm}^2$ (Case 7). The lateral displacement at the end of the superstructure is not sensitive to the pile surface area because the axial stiffness of the superstructure is markedly greater than the lateral stiffness of the soil-pile system. The pile head deflection increases because the soil resistance decreases due to the reduction of the pile surface area. Based on Equation 5-1, with similar lateral displacement at the end of the superstructure and greater pile head deflection, the rotations (Θ_p and Θ_s) decrease.

**Table 5-14(a): Displacements at the Pile Head and at the End of the Superstructure
Obtained from SAP 2000 Analyses for Cases 6 and 7**

Case	Δ_p (mm)				Δ_s (mm)			
	LP	B-	K-	L-	LP	B-	K-	L-
6	6.2	4.5	5.2	5.4	12.6	12.4	12.5	12.5
7	6.7	5.2	5.8	6.3	12.6	12.5	12.6	12.6

**Table 5-14(b): Rotations at the Pile Head and the End of the Superstructure
Obtained from SAP 2000 Analyses for Cases 1 and 6**

Case	Θ_p (rad)				Θ_s (rad)			
	LP	B-	K-	L-	LP	B-	K-	L-
6	0.0026	0.0031	0.0029	0.0028	0.0024	0.0030	0.0028	0.0027
7	0.0023	0.0029	0.0027	0.0026	0.0022	0.0028	0.0025	0.0025

Tables 5-15(a) and (b) summarize the total pile-head moments and shear forces at each abutment and the moments and axial forces at the end of the superstructure, respectively, for the different pile surface areas. As the soil-pile stiffness reduces due to the decrease of the pile surface area, the SAP-LP and SAP-B analyses generally yield lower restraint load effects at the pile head and end of the superstructure, except for the moment at the pile head obtained from the SAP-B analyses. The probable reasons are as presented previously in Section 5.4.4.

**Table 5-15(a): Total Moments and Shear Forces of Piles from SAP 2000
for Cases 6 and 7**

Case	$\sum M_p$ (kN.m)				$\sum V_p$ (kN)			
	LP	B-	K-	L-	LP	B-	K-	L-
6	-530	-372	-449	-477	1499	2244	1968	1850
7	-330	-444	-496	-541	1476	1967	1690	1623

**Table 5-15(b): Moments and Axial Forces at the End of the Superstructure
Obtained from SAP 2000 for Cases 6 and 7**

Case	M_s (kN.m)				N_s (kN)			
	LP	B-	K-	L-	LP	B-	K-	L-
6	-6205	-7979	-7339	-7062	2593	3338	3061	2944
7	-6178	-7332	-6666	-6536	2549	3061	2784	2717

The $\sum M_p$ values increase for the SAP-LP analysis but reduce for the SAP-B analyses when the pile surface area is reduced. The SAP-B analyses consistently yield greater $\sum V_p$, M_s , and N_s than the SAP-LP analysis when the pile surface area is reduced.

5.4.6 Effect of Soil Conditions

Tables 5-16 (a) and (b) present the deflections and rotations, respectively, at the pile head of each pile and at the end of the superstructure as the mixed soil profile with four soil layers (Case 1) is replaced with uniform loose sand (Case 8) and uniform dense sand (Case 9). The soil properties assumed for Cases 8 and 9 and the corresponding soil Young's moduli estimated using the B-, K-, and L-, relationships are included in Appendix K. For simplicity of the soil-pile modelling, the water table located at 5.55 m below the pile head is assumed to have negligible effect on the deformations and load effects of the bridge and piles. This assumption is validated by Appendix L. As noted previously, the displacement at the end of the superstructure is insensitive to the soil-pile stiffness because the axial stiffness of the bridge superstructure is markedly higher than the lateral stiffness of the soil-pile system. The pile head deflection decreases, and the rotation increases as the surrounding soil becomes stiffer. Again, as noted previously, the SAP-LP analysis yields similar Δ_s , greater Δ_p , and hence lower Θ_p and Θ_s than the SAP-B analyses.

Table 5-16(a): Displacements at the Pile Head and at the End of the Superstructure Obtained from SAP 2000 Analyses for Cases 1, 8, and 9

Case	Δ_p (mm)				Δ_s (mm)			
	LP	B-	K-	L-	LP	B-	K-	L-
1	6.4	4.8	5.5	5.7	12.6	12.5	12.6	12.6
8	6.3	4.4	5.0	5.2	12.6	12.4	12.5	12.5
9	5.1	3.0	3.5	4.2	12.5	12.3	12.3	12.4

Table 5-16(b): Rotations at the Pile Head and the End of the Superstructure Obtained from SAP 2000 Analyses for Cases 1, 8, and 9

Case	Θ_p (rad)				Θ_s (rad)			
	LP	B-	K-	L-	LP	B-	K-	L-
1	0.0025	0.0030	0.0028	0.0027	0.0023	0.0028	0.0026	0.0026
8	0.0025	0.0032	0.0030	0.0029	0.0024	0.0030	0.0028	0.0027
9	0.0029	0.0037	0.0035	0.0033	0.0027	0.0035	0.0033	0.0031

Tables 5-17 (a) and (b) summarize the load effects at the pile head and at the end of the superstructure, respectively, for bridges with different soils surrounding the piles. As described in Section 5.4.4, as the soil stiffness increases, these load effects generally

increase, but the moment at the pile head from the SAP-B analyses decreases. The probable reasons are as presented in Section 5.4.4.

Table 5-17(a): Moments and Shear Forces at the Head of Each Pile Obtained from SAP 2000 Analyses for Cases 1, 8, and 9

Case	M_p per pile (kN.m/pile)				V_p per pile (kN/pile)			
	LP	B-	K-	L-	LP	B-	K-	L-
1	-80.7	-75.5	-77.9	-78.0	230	336	293	285
8	-83.5	-70.2	-76.8	-75.2	232	379	336	321
9	-87.3	-49.7	-50.3	-63.3	304	479	448	397

Table 5-17(b): Moments and Axial Forces at the End of the Superstructure Obtained from SAP 2000

Case	M_s (kN.m)				N_s (kN)			
	LP	B-	K-	L-	LP	B-	K-	L-
1	-5915	-7554	-6901	-6763	-2453	-3086	-2833	-2841
8	-5964	-8102	-7479	-7251	-2464	-3366	-3111	-3026
9	-7113	-9540	-8096	-8051	-2894	-3968	-3358	-3349

As described in Section 5.4.4, the SAP-B analyses yield consistently greater V_p , M_s , and N_s but lower M_p than the SAP-LP analysis. The probable reasons are discussed in Section 5.4.4.

5.4.7 Effect of Pile Sleeve Presence and Infill Soil State

Tables 5-18 (a) and (b) present the deflections and rotations, respectively, at the pile head of each pile and at the end of the superstructure as the soil in the top (sleeved) 3 m is replaced by sand with effective unit weight of 15 kN/m³ and friction angle of 30° (Case 10) and sand with effective unit weight of 22 kN/m³ and friction angle 40° (Case 11). Case 10 represents the responses for the bridge with piles sleeved with very loose sand, while Case 11 represents the responses for the bridge with piles sleeved with very dense sand. The soil input parameters for the SAP-LP and SAP-B analyses are presented in Appendix M. As discussed in Section 5.4.6, the water table is neglected for simplicity of the soil modelling. As shown in the tables, the lateral displacement at the end of the superstructure is insensitive to the presence of a sleeve or to the soil stiffness. On the other hand, the

deflection at the pile head decreases because the sleeve-fill is stiffer than the original soil surrounding the piles. Consequently, from Equation 5-1, the rotations (Θ_p and Θ_s) increase.

Table 5-18(a): Displacements at the Pile Head and at the End of the Superstructure Obtained from SAP 2000 Analyses for Cases 1, 10, and 11

Case	Δ_p (mm)				Δ_s (mm)			
	LP	B-	K-	L-	LP	B-	K-	L-
1	6.4	4.8	5.5	5.7	12.6	12.5	12.6	12.6
10	6.2	4.7	5.3	5.5	12.6	12.5	12.5	12.5
11	4.4	2.7	3.1	4.4	12.5	12.2	12.3	12.4

Table 5-18(b): Rotations at the Pile Head and the End of the Superstructure Obtained from SAP 2000 Analyses for Cases 1, 10, and 11

Case	Θ_p (rad)				Θ_s (rad)			
	LP	B-	K-	L-	LP	B-	K-	L-
1	0.0025	0.0030	0.0028	0.0027	0.0023	0.0028	0.0026	0.0026
10	0.0025	0.0031	0.0029	0.0028	0.0024	0.0029	0.0027	0.0027
11	0.0031	0.0038	0.0036	0.0032	0.0030	0.0036	0.0034	0.0030

Tables 5-19 (a) and (b) summarize the load effects at the pile head and at the end of the superstructure, respectively, for bridges with different sleeve presence and infill soil states. As described in Section 5.4.7, as the soil-pile stiffness increases, the SAP-LP and SAP-B analyses yield higher restrained load effects at the pile head and the end of the superstructure except the moment at the pile head obtained from the SAP-B analyses. As the piles will likely experience cyclic deformations due to seasonal and daily temperature variations, the sleeve fill may be compacted and become denser, so that the moment and axial force at the end of the superstructure and the shear force at the pile head will increase over time, and the moment at the pile head may increase.

Table 5-19(a): Moments and Shear Forces at the Head of Each Pile Obtained from SAP 2000 for Cases 1, 10, and 11

Case	M_p per pile (kN.m/pile)				V_p per pile (kN/pile)			
	LP	B-	K-	L-	LP	B-	K-	L-
1	-80.7	-75.5	-77.9	-78.0	230	336	293	285
10	-85.0	-77.5	-81.4	-81.8	239	357	314	303
11	-81.8	-38.3	-51.0	-74.3	349	503	471	378

**Table 5-19(b): Moments and Axial Forces at the End of the Superstructure
Obtained from SAP 2000 for Cases 1, 10, and 11**

Case	M_s (kN.m)				N_s (kN)			
	LP	B-	K-	L-	LP	B-	K-	L-
1	-5915	-7554	-6901	-6763	2453	3086	2833	2841
10	-6077	-7799	-7154	-6989	2505	3232	2975	2910
11	-7799	-9840	-9414	-8122	-3164	-4110	-3916	-3364

As discussed in Section 5.4.4, the SAP-B analyses yield consistent greater V_p , M_s , and N_s but lower M_p than the SAP-LP analysis. The probable reasons are discussed in Section 5.4.4.

5.5 Summary and Conclusions

This chapter develops equilibrium and compatibility equations describing the fundamental mechanics of the integral abutment region for an integral abutment bridge subjected to uniform temperature variations, temperature gradients, and earth pressures. The accuracy of these equations is verified using a finite-element-based parametric study using the p-y approach (Reese et al. 1974; Matlock 1970) and the continuum mechanics approach adapted by Basu and Salgado (2008). The influences of different structural configurations and soil properties on the bridge deformations and restrained load effects are explained analytically using the derived equations. Also, the finite-element results are compared to study the influence of soil-pile interactions on different integral abutment bridges.

The conclusions of this chapter are as follows:

1. Equations are derived considering the equilibrium and compatibility of the integral abutment region to analyze integral abutment bridges. If the abutment height, soil-pile stiffness matrix, superstructure flexural and axial stiffnesses, earth pressure and the displacement at the end of the superstructure due to the temperature variation, temperature gradient and earth pressure known, the deformations at the pile head, rotation of the abutment, and the force effects at the pile head and the end of the superstructure can be quantified. The associated equations are validated by the finite element analysis. Therefore, these equations are important tools to enhance

the understanding of the behavior of integral abutment bridges, and to independently check results from finite element analyses.

2. The lateral displacements at the end of the superstructure are insensitive to the soil-pile idealization adopted because the axial stiffness of the superstructure is markedly greater than the lateral stiffness of the soil-pile system. When the superstructure expands due to a positive temperature gradient, the backfill and soil-pile system do not significantly restrain this expansion.
3. Based on the parametric study, the soil-pile idealizations do not change the rotation and displacement at the end of the superstructure markedly, but they can influence the moment and axial force at the end of the superstructure. However, the influence may not be significant enough to affect the design. On the other hand, the influence of soil-pile stiffnesses is relatively insignificant for the moment at the pile head but significant for the shear forces at the pile head, which may affect the pile design.
4. The corresponding SAP 2000 analysis with the Basu soil-pile idealization (SAP-B) consistently yields lower pile head deflections, greater pile head rotations, and greater pile shear forces than the SAP 2000 analysis with the LPILE soil-pile idealization (SAP-LP). This occurs because the lateral stiffness of the soil-pile system is consistently greater for the Basu-based idealization. Consequently, the axial force and moment at the end of the superstructure are also consistently greater for the SAP-B analyses.
5. The parametric study confirms that the restraint force effects at the end of the superstructure can be reduced if the bridge length is reduced, the superstructure is more flexible, or the lateral stiffness of the soil-pile system is reduced.
6. The parametric study indicates that the change of the abutment height has insignificant influence on the abutment rotation and displacement at the end of the superstructure. Consequently, increasing the abutment height reduces the magnitude of pile head deflection and load effects at the pile head and the end of

the superstructure until the displacement at the end of the bridge and at the pile head in opposite sense.

Chapter 6

6 Research Summary, Limitations, Conclusions, and Future Work

6.1 Summary

Integral abutment bridges eliminate the expansion joints at the end of the bridge deck and integrate the bridge superstructure with the abutments. This practice effectively reduces the high costs associated with the installation, maintenance and replacement of the expansion joints. It also simplifies the construction process but introduces complexity to the analysis and design. Deformations of the superstructure must be accommodated by movement of the abutment and piles, inducing reactions in the surrounding soil. Normally, a fully integrated geo-structural analysis is required to determine the soil reactions and the corresponding pile lateral deflections. Should the soil response become nonlinear, an iterative analysis must be performed.

The two common approaches to idealize the soil-pile interactions for laterally loaded piles are the p-y and continuum mechanics approaches. The p-y approach idealizes the interaction using a series of lateral linear-elastic springs distributed vertically over the depth of the pile. The continuum mechanics approach, particularly as adapted by Basu and Salgado (2008), idealizes the soil as a continuous medium so is more rational.

Chapter 2 presented an overview of integral abutment bridge systems, loadings, construction sequence, and previous field studies and numerical studies by others to quantify the behavior. It also reviewed the p-y and continuum mechanics approaches including their integration in the idealizations of laterally loaded piles and integral abutment bridges.

Chapter 3 presented an investigation of the influence of soil-pile interactions on the response of a specific single free-headed pile subjected to a lateral force or a moment. Three distinct analyses were included: (1) comparing the pile lateral deflections when the pile is subjected to a lateral force or a moment to evaluate the difference in soil-pile

stiffnesses; (2) comparing the pile head deflections when the pile is subjected to increasing lateral loads to assess the effect of accounting for soil plasticity; and (3) generalizing the lateral deflection of the head of the pile as a function of the relative stiffness of the pile and soil and the slenderness ratio of the pile to extend the findings of a specific soil-pile system to various soil-pile systems. Each analysis comprised of four independent analyses, including an analysis conducted using LPILE, a p-y approach-based software, and three continuum-based analyses conducted using Basu's software, based on soil input parameters estimated using the relationships developed by Biot (1937), Kishida et al. (1985), and Lashkaripour and Ajalloejan (2003).

Chapter 4 presented the deformations and force effects, computed using the p-y and Basu approaches, of a specific integral abutment bridge subjected to combinations of: (1) temperature variations, temperature gradients, and earth pressures; or (2) truck loading. A 2D finite element model of Bridge #55555 in Minnesota was created using SAP 2000 and was integrated with the LPILE (SAP-LP) or Basu analyses (SAP-B). As in Chapter 3, the soil input parameters for the SAP-B analyses were estimated using the relationships developed by Biot (1937), Kishida et al. (1985), and Lashkaripour and Ajalloejan (2003). In addition, the response of simple idealizations of the superstructure/abutment connection as fixed or pinned were compared to those from the SAP-LP and SAP-B models for a single truck loading case.

Chapter 5 presented a simplified model of the integral abutment region. Mechanics-based equations are derived based on the principles of equilibrium and compatibility to quantify the deformations and restraint-induced load effects at the pile head and the end of the superstructure. The equations are validated by independent finite-element analysis. This chapter also presented a parametric study that investigates the influence of soil-pile interactions on the response of integral abutment bridges with various design configurations and soil conditions.

6.2 Limitations and Assumptions

The limitations of this research are as follows:

1. The integral abutment bridges used for the numerical analyses were straight with no skew and the soil surrounding piles and behind the abutments were assumed to be identical at each side of the bridge.
2. The soil and pile were assumed to behave as a linear-elastic system in the Basu analyses and the pile was assumed to have a linear-plastic response in the LPILE analyses.
3. Backfill is assumed present on both sides of the pile head in LPILE and Basu analyses even though it is really only present on one side of the abutment due to limitations of the software.
4. The superstructure/abutment and the abutment/pile connections were assumed to be fixed, with identical rotation of the connected components under load..

6.3 Conclusions

The conclusions of this study are as follows:

1. For the specific case of a single free-ended pile investigated, the continuum mechanics approach tends to predict a higher soil-pile stiffness than the p-y approach for apparently equivalent soil properties. Consequently, for a given applied lateral load or moment, the continuum mechanics approach predicts a lower lateral deflection and rotation at the pile head. The pile head deflections obtained from the LPILE analyses are approximately 31-52% higher than the Basu analyses when a lateral force is applied and 25-41% when a moment is applied. However, because the largest pile head deflections are less than 10 mm, the practical implications of these differences are likely slight.
2. For a single free-ended pile subjected to a lateral force at the pile head, using the Basu software, the analysis based on the Biot relationship (Equation 3-2b) yields the lowest lateral deflection and hence the highest pile head stiffness because the Biot's relationship corresponds to the greatest input soil stiffness. The pile head deflection for the Biot's relationship is approximately 34% and 42% lower than the

Kishida's and Lashkaripour's relationship. However, the implications of these differences are small given the uncertainties in soil in-situ properties. Similar responses were observed when the pile is subjected to a moment at the pile head.

3. For free-ended laterally loaded piles, when the maximum pile deflection exceeds the linear-elastic limit of the soil, the difference between the soil-pile stiffnesses predicted using LPILE and Basu's software increases because the p-y approach (LPILE) accounts for plastic behavior of soil, whereas the continuum mechanics approach (Basu's software) does not.
4. For free-ended laterally loaded piles, when soil behavior is linear elastic, the normalized lateral pile head deflection can be expressed as an empirical function of the relative stiffness of pile and soil, and of the pile slenderness ratio. When the pile head is subjected to either a lateral force or a moment, the normalized pile head deflection decreases as the pile stiffness increases with respect to the soil stiffness. The influence of the pile slenderness ratio is negligible when the pile behaves as a long pile.
5. For integral abutment bridges, the longitudinal displacement at the end of the superstructure due to thermal expansion or contraction is insensitive to the soil-pile idealization because the axial stiffness of the superstructure is relatively large compared to that of the soil-pile system. For a symmetrical bridge with identical soil conditions at the abutments, this longitudinal displacement can be approximated as $\frac{1}{2}\Delta T\alpha L_s$ where ΔT is the temperature variation, α is the coefficient of expansion, and L_s is the total length of the bridge.
6. For the specific integral abutment bridge investigated, when subjected to thermally induced movements and soil pressures, the lower soil-pile stiffness obtained using the p-y (LPILE) approach typically yielded greater deflection and moment and lesser rotation and shear force at the pile head, and lesser moment and axial forces at the end of the superstructure. For the case of bridge expansion investigated, the difference between the LPILE and Basu-based analyses range between 23-42% for

pile shear forces and between 3-9% for pile moments. Similar ranges were observed for the case of bridge contraction. The difference in shear forces may influence the pile design.

7. When the specific integral abutment bridge investigated is subjected to truck loadings, the SAP 2000 analysis with the LPILE soil-pile idealization (SAP-LP) and the SAP 2000 analyses with the Basu soil-pile idealizations (SAP-B) yield a conservative moment at the mid-point of the exterior span but an unconservative moment at the end of the superstructure compared to actual moments measured in the field. However, the moment at the end of the superstructure is very small compared to that induced by the thermal movements and earth pressure, so for design purposes either the SAP-LP or SAP-B procedures are adequate for quantifying the moments at both locations.
8. The simplified idealizations of the abutment/superstructure connection as being fully fixed or pinned yield inaccurate results due to single truck loading the specific integral abutment bridge investigated. The assumption of a pinned connection yields a moment of the wrong sense at the end of the superstructure and overestimates the midspan moment in the exterior span. The assumption of a fully fixed connection markedly overestimates the moment at the abutment and so markedly underestimates the midspan moment in the exterior span.
9. Based on the parametric study, the soil-pile idealizations do not change the rotation and displacement at the end of the superstructure markedly, but they can influence the moment and axial force at the end of the superstructure. However, the influence may not be significant enough to affect the design. The influence of soil-pile stiffnesses is relatively insignificant for the moment at the pile head, but the influence on the shear forces at the pile head may affect the pile design.
10. The parametric study of integral abutment bridges confirms that the restraint force effects at the end of the superstructure can be reduced if the bridge length, stiffness of the superstructure, or the stiffness of the soil-pile system decrease.

11. The parametric study indicates that the change of the abutment height has insignificant influence on the abutment rotation and displacement at the end of the superstructure. Consequently, increasing the abutment height reduces the magnitude of pile head deflection and load effects at the pile head and the end of the superstructure until the displacement at the end of the bridge and at the pile head are in opposite sense.
12. Mechanics-based equations derived considering equilibrium and compatibility in the integral abutment region can accurately quantify the deformations and load effects in integral abutment bridges. Specifically, if the abutment height, soil-pile stiffness matrix, superstructure flexural and axial stiffnesses, earth pressure and the displacement at the end of the superstructure are known, the deformations at the pile head, rotation of the abutment, and the force effects at the pile head and the end of the superstructure can be quantified.

6.4 Recommendations for Future Work

It is recommended that further research efforts be directed to address the following:

1. Field tests or small-scaled laboratory tests are necessary to validate the p-y and continuum mechanics approaches considered in the present study. In particular, tests to improve the empirical basis of the p-y method are needed. Small-scaled laboratory tests conducted using geotechnical centrifuge modelling is recommended because it provides a controlled laboratory environment and is relatively inexpensive.
2. The algorithms in Basu's software could possibly be modified to account for the non-linear elastic responses of soil. Although the response is nominally still in the elastic (recoverable) state, it has been found that shear force and Young's modulus can vary by orders of magnitude for different strain ranges. This would improve the application of Basu analysis. The inclusion of plasticity effects would also allow application to longer integral abutment bridges with greater bridge end displacements due to thermal movements.

3. The mechanics-based equations describing the equilibrium and compatibility of the integral abutment region can be further developed and exploited to, for example, to derive design limits that support current design guidelines or extend the application of integral abutment bridges to longer spans. This can be achieved by carrying out sensitivity analyses using these equations.
4. The research can be further expanded to consider skewed and curved integral abutment bridges to determine rationally based limits on skew angle and curvature radius.
5. The passive/active earth pressures were estimated based on the approach recommended by the commentary of Canadian Highway Bridge Design Code (CSA 2019). However, it is relatively crude. A more sophisticated approach can be adopted to idealize the interactions between the backfill and abutment.

References

- Ameratunga, J., Sivakugan, N., and Das, B.M. 2016. *Correlations of Soil and Rock Properties in Geotechnical Engineering*. Springer India: New Delhi.
- Anderson, J.B., Townsend, F.C., and Grajales, B. 2003. “Case History Evaluation of Laterally Loaded Piles.” *Journal of Geotechnical and Geoenvironmental Engineering* **129** (3): 187–96.
- API (American Petroleum Institute). 2011. *Geotechnical and Foundation Design Considerations, API Recommended Practice*. 1st Edition. Washington, DC.
- Arockiasamy, M., Butrieng, N., and Sivakumar, M. 2004. “State-of-the-Art of Integral Abutment Bridges: Design and Practice.” *Journal of Bridge Engineering* **9** (5): 497–506.
- Baptiste, K.T., Kim, W.S., and Laman, J.A. 2011. “Parametric Study and Length Limitations for Prestressed Concrete Girder Integral Abutment Bridges.” *Journal of the International Association for Bridge and Structural Engineering* **21** (2): 151–56.
- Basu, D., Salgado, R., and Prezzi, M. 2008. “Analysis of Laterally Loaded Piles in Multilayered Soil Deposits.” Indiana Department of Transportation. West Lafayette, Indiana.
- Basu, D., and Salgado, R. 2008. “Analysis of Laterally Loaded Piles with Rectangular Cross Sections Embedded in Layered Soil.” *International Journal for Numerical and Analytical Methods in Geomechanics* **32** (7): 721–44.
- Basu, D., Salgado, R., and Prezzi, M. 2009. “A Continuum-Based Model for Analysis of Laterally Loaded Piles in Layered Soils.” *Geotechnique* **59** (2): 127–40.
- Basudhar, P.K., Yadav, S.K., and Basudhar, A. 2018. “Treatise on Winkler Modulus of Subgrade Reaction and Its Estimation for Improved Soil–Structure Interaction Analysis.” *Geotechnical and Geological Engineering* **36** (5): 3091–3109.

- Biot, M.A. 1937. "Bending of an Infinite Beams on an Elastic Foundation." *Journal of Applied Mechanics* **4**: A1–7.
- Bloodworth, A.G., Xu, M., Banks, J.R., and Clayton, C.R.I. 2012. "Predicting the Earth Pressure on Integral Bridge Abutments." *Journal of Bridge Engineering* **17** (2): 371–81.
- Bouafia, A., and Garnier, J. 1991. "Experimental Study of P-y Curves for Piles in Sand." *Proceedings of the International Conference on Centrifuge*, Rotterdam, the Netherlands, 261–68.
- Breña, S.F., Bonczar, C.H., Civjan, S.A., DeJong, J.T., and Crovo, D.S. 2007. "Evaluation of Seasonal and Yearly Behavior of an Integral Abutment Bridge." *Journal of Bridge Engineering* **12** (3): 296–305.
- Burke, P.M. 1993. "Design of Integral Concrete Bridges." *Concrete International* **15** (6): 37–42.
- Bustamante, G. 2014. "Influence of Pile Shape on Resistance to Lateral Loading." MSc. Thesis. Brigham Young University.
- Card, G.B. and Carder, D.R. 1993. "A literature Review of the Geotechnical Aspects of the Design of Integral Bridge Abutments." Transportation Research Laboratory. Crowthorne, Berkshire.
- Civjan, S.A., Kalayci, E., Quinn, B.H., Breña, S.F., and Allen, C.A. 2013. "Observed Integral Abutment Bridge Substructure Response." *Engineering Structures* **56**: 1177–91.
- Computers and Structures. 2020. "CSI Analysis Reference Manual." Berkeley, California.
- Craig, R.F. 1983. "Lateral Earth Pressure." In *Soil Mechanics*, 183–236. Springer: Boston, MA.

- CSA International. 2014. *Design of Steel Structure (S16-14)*. CSA International: Mississauga, Ontario.
- CSA International. 2019. *Commentary On CSA S6:19, Canadian Highway Bridge Design Code*. CSA International: Mississauga, Ontario.
- David, T. K., and Forth, J.P. 2011. “Modelling of Soil Structure Interaction of Integral Abutment Bridges.” *Proceedings of International Conference on Structural Engineering*. Kandy, Sri Lanka. 78: 769–74.
- David, T.K., Forth, J.P., and Ye, J. 2014. “Superstructure Behavior of a Stub-Type Integral Abutment Bridge.” *Journal of Bridge Engineering* **19** (6): 1–12.
- Dicleli, and Albhaisi. 2003. “Maximum Length of Integral Bridges Supported on Steel H-Piles Driven in Sand.” *Engineering Structures* **25** (12): 1491–1504.
- Dicleli, M. 2000. “Simplified Model for Computer-Aided Analysis of Integral Bridges.” *Journal of Bridge Engineering* **5** (3): 107–13.
- Faraji, S., Ting, J.M., Crovo, D., and Ernst, H. 2001. “Non-Linear Analysis of Integral Bridges: Finite Element Model.” *Journal of Geotechnical and Geoenvironmental Engineering* **127** (5): 454–61.
- Fennema, J.L., Laman, J.A., and Linzell, D.G. 2005. “Predicted and Measured Response of an Integral Abutment Bridge.” *Journal of Bridge Engineering* **10** (6): 666–77.
- Federal Highway Administration. 1986. “Seismic Design of Highway Bridge Foundations, Vol. II: Design Procedures and Guidelines.” Washington, DC.
- Gerolymos, N., Escoffier, S., Gazetas, G., and Garnier, J. 2009. “Numerical Modeling of Centrifuge Cyclic Lateral Pile Load Experiments.” *Earthquake Engineering and Engineering Vibration* **8** (1): 61–76.
- Greimann, L.F., Yang, P., and Wolde-Tinsae, A.M. 1987. “Nonlinear Analysis of Integral Abutment Bridges.” *Journal of Structural Engineering* **112** (10): 2263–80.

- Gupta, B.K., and Basu, D. 2020. “Computationally Efficient Three-Dimensional Continuum-Based Model for Nonlinear Analysis of Laterally Loaded Piles.” *Journal of Engineering Mechanics* **146** (2): 1–17.
- Haldar, A., Prasad, Y. V. S. N., and Chari, T. R., 2000, “Full-Scale Field Tests on Directly Embedded Steel Pole Foundations.” *Canadian Geotechnical Journal*. **37**: 414–37
- Hassiotis, S., Khodair, Y., Roman, E., and Dehne, Y. 2006. “Evaluation of Integral Abutments.”. Stevens Institute of Technology. Hoboken, New Jersey.
- Hassiotis, S., and Xiong, K. 2007. “Deformation of Cohesionless Fill Due to Cyclic Loading.”. Stevens Institute of Technology. Hoboken, New Jersey.
- He, L., Elgamal, A., Yang, Z., and Lu, J. 2004. “A Three-Dimensional Finite Element Study To Obtain P-Y Curves for Sand.” *Proceedings of 17th ASCE Engineering Mechanics Conference*. Newark, Delaware. **1**: 1–13.
- Heidari, M., Jahanandish, M., Naggar, H. El, and Ghahramani, A. 2014. “Nonlinear Cyclic Behavior of Laterally Loaded Pile in Cohesive Soil.” *Canadian Geotechnical Journal* **51** (2): 129–43.
- Higgins, W., Vasquez, C., Basu, D., and Griffiths, D. V. 2013. “Elastic Solutions for Laterally Loaded Piles.” *Journal of Geotechnical and Geoenvironmental Engineering* **139** (7): 1096–1103.
- Hu, B., and Wu, Z. 2014. “Extending Applicability of Integral Abutment in Highly Skewed Bridges.” *Proceedings of International Conference on Short and Medium Span Bridges*, Calgary, Alberta. 1970-79
- Huang, J., French, C., and Shield, C. 2004. “Behavior of Concrete Integral Abutment Bridges.”. Minnesota Department of Transportation. St. Paul. Minneapolis.
- Huang, Shield, C., and French, C. 2011. “Behavior of an Integral Abutment Bridge in

- Minnesota, US.” *Journal of the International Association for Bridge and Structural Engineering* **21** (3): 320–31.
- Huang, Shield, and French. 2008. “Parametric Study of Concrete Integral Abutment Bridges.” *Journal of Bridge Engineering* **13** (5): 511–26.
- Huntley, S.A., and Valsangkar, A.J. 2014. “Behaviour of H-Piles Supporting an Integral Abutment Bridge.” *Canadian Geotechnical Journal* **51** (7): 713–34.
- Isenhower, W.M., and Wang, S.T. 2013. *Technical Manual for L-Pile 2013*. Vol. 2013. Ensoft: Austin, Texas.
- Johnson, I.D., and McAndrew, S.P. 1993. “Research into the Condition and Performance of Bridge Deck Expansion Joints.” Transport Research Laboratory: Crowthorne, Berkshire.
- Khodair, Y.A., and Hassiotis, S. 2005. “Analysis of Soil-Pile Interaction in Integral Abutment.” *Computers and Geotechnics* **32** (3): 201–9.
- Kim, B.T., Kim, N.-K., Lee, W.J., and Kim, Y.S. 2004. “Experimental Load-Transfer Curves of Laterally Loaded Piles in Nak-Dong River Sand.” *Journal of Geotechnical and Geoenvironmental Engineering* **23** (40): 1390–92.
- Kim, and Laman. 2010. “Integral Abutment Bridge Response under Thermal Loading.” *Engineering Structures* **32** (6): 1495–1508.
- Kishida, H., Suzuki, Y., and Nakai, S. 1985. “Behavior of a Pile under Horizontal Cyclic Loading.” *Proceedings of 11th International Conference on Soil Mechanics and Foundation Engineering*, 1413–16. San Francisco. California.
- Kong, B., Cai, C.S., and Zhang, Y. 2016. “Parametric Study of an Integral Abutment Bridge Supported by Prestressed Precast Concrete Piles.” *Engineering Structures* **120**: 37–48.
- Kunin, J., and Alampalli, S. 1999. “Integral Abutment Bridges: Current Practice in the

- United States and Canada.”. New York State Department of Transportation. Albany. New York.
- Lashkaripour, G.R., and Ajalloeian, R. 2003. “Determination of Silica Sand Stiffness.” *Engineering Geology* **68** (3–4): 225–36.
- Lawver, A., French, C., and Shield, C.K. 2000. “Field Performance of Integral Abutment Bridge.” Transportation Research Record 1740. Washington, D.C.
- Matlock, H. 1970. “Correlations for Design of Laterally Loaded Piles in Soft Clay.” *Proceedings of 2nd Offshore Technology Conference*, 577–94. Houston, Texas.
- Meyer, B.J., and Reese, L.C. 1979. “Analysis of Single Piles Under Lateral Loading.” Center for Highway Research. Austin, Texas.
- Minnesota Department of Transportation. 2005. “Minnesota Trucking Regulations.” Minnesota Department of Transportation. Saint Paul, Minnesota.
- New York State Department of Transportation. 2015. *Geotechnical Engineering Manual*. GEM-26. New York Department of Transportation. New York.
- Olson, S.M., Long, J.H., Hansen, J.R., Lafave, J.M., and Renekis, D. 2009. “Modification of IDOT Integral Abutment Design Limitations and Details.” Illinois Center for Transportation. Urbana, Illinois.
- Pétursson, H. 2015. *Design of Steel Piles for Integral Abutment Bridges*. PhD Dissertation. Luleå University of Technology.
- Pétursson, H., Collin, P., Veljkovic, M., and Andersson, J. 2011. “Monitoring of a Swedish Integral Abutment Bridge.” *Journal of the International Association for Bridge and Structural Engineering* **21** (2): 175–80.
- PLAXIS BV. (2013). PLAXIS 3D 2013 Reference Manual. Delft: PLAXIS BV.
- Poulos, H.G., Chow, H.S.W., and Small, J.C. 2019. “The Use of Equivalent Circular

- Piles to Model the Behaviour of Rectangular Barrette Foundations.” *Geotechnical Engineering* **50** (3): 106–9.
- Quinn, B.H., and Civjan, S.A. 2017. “Parametric Study on Effects of Pile Orientation in Integral Abutment Bridges.” *Journal of Bridge Engineering* **22** (4): 1–14.
- Qin and Guo. 2007. “An experimental study on cyclic loading of piles in sand.” *Proceedings of the 10th Australia New Zealand Conference on Geomechanics*, Brisbane, Australia
- Randolph, M.F. 1981. “The Response of Flexible Piles to Lateral Loading.” *Geotechnique* **31** (2): 247–259.
- Reese, L.C., Welch, R.C. 1975. “Lateral Loading of Deep Foundations in Stiff Clay.” *Journal of the Geotechnical Engineering Division* **101**: 633–49.
- Reese, L.C., Cox, W.R., and Koop, F.D. 1974. “Analysis of Laterally Loaded Piles in Sand.” *Proceedings of 7th Offshore Technology Conference*, 473–83. Houston, Texas.
- Reese, L.C., and Wang. 1993. “COM624P-Laterally loaded pile analysis program for the microcomputer, Version 2.0.” *Federal Highway Administration*, Washington, D.C
- Rollins, K.M., Olsen, K.G., Jensen, D.H., Garrett, B.H., Olsen, R.J., and Egbert, J.J. 2006. “Pile Spacing Effects on Lateral Pile Group Behavior: Analysis.” *Journal of Geotechnical and Geoenvironmental Engineering* **132** (10): 1272–83.
- Russell, D.N. 2016. “The Influence of Pile Shape and Pile Sleeves on Lateral Load Resistance.” MSc. Thesis. Brigham Young University.
- She, J.L.Y. 1983. “Prediction of P-Y Curves from Finite Element Analysis.” B.A.Sc. Thesis. Univeristy of British Columbia.
- Shirato, M., Nakatani, S., Matsui, K., and Nakaura, T. 2009. “Geotechnical Criterion for Serviceability Limit State of Horizontally-Loaded Deep Foundations.” *Proceedings*

- of the 2nd International Symposium on Geotechnical Safety and Risk. Gifu, Japan.
- SIMULIA. (2010). Abaqus 6.9 theory manual, SIMULIA, Providence, RI.
- Springman, S.M., Norrish, A.R.M., and Ng, C.W.W. 1996. "Cyclic Loading of Sand Behind Integral Bridge Abutments.". Transport Research Laboratory. Crowthorne. Berkshire.
- Tabrizi, A., Clarke-Sather, A., Schumacher, T., and Healy, R. 2016. "Bridge Retrofit or Replacement Decisions: Tools to Assess Sustainability and Aid Decision-Making." University of Delaware. Newark, Delaware.
- Taly, N. 1998. *Design of Modern Highway Bridges*. McGraw-Hill: Los Angeles, USA.
- Vesic, A. 1961. "Bending of Beams Resting on Isotropic Elastic Solid." *Journal of Applied Mechanics*. **87** (2): 35–53.
- Wesselink, B.D., Murff, J.D., Randolph, M.F., Nunez, I.L., and Hyden, A.M. 1988. "Analysis of Centrifuge Model Test Data from Laterally Loaded Piles in Calcareous Sand." *Engineering for Calcareous Sediments* **1**: 261–270.
- White, H. 2007. "Integral Abutment Bridges: Comparison of Current Practice Between European Countries and the United States of America.". New York State Department of Transportation. Albany, New York.
- Yang, K., and Liang, R. 2007. "Methods for Deriving P-y Curves from Instrumented Lateral Load Tests." *Geotechnical Testing Journal* **30** (1): 31–38.

Appendix A: API Relationship

Figure A-1 illustrate the relationship between the k value in kN/m^3 and the corresponding soil friction angle and relative density. By multiplying the k value obtained from the Figure A-1 by the equivalent depth of the soil, the soil subgrade reaction modulus (kN/m^2) can be obtained.

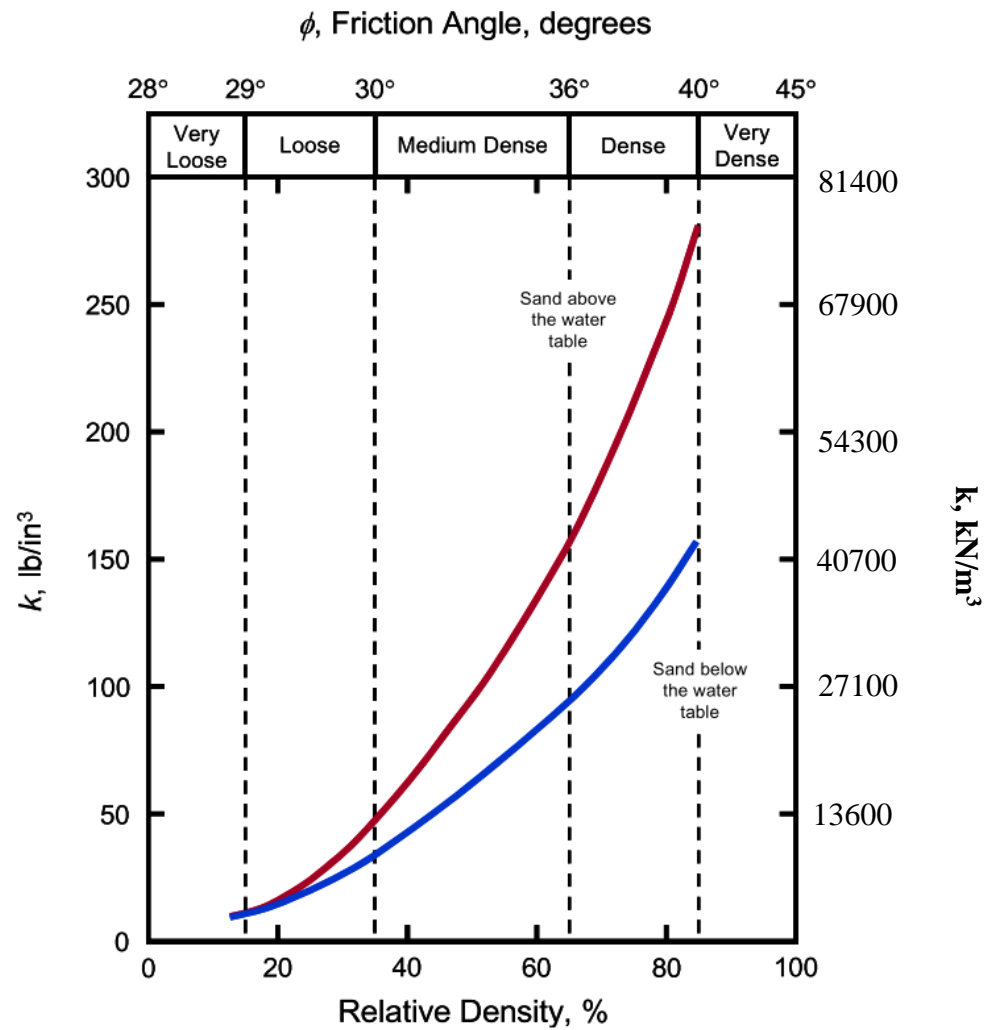


Figure A- 1: API Relationship (API 2010)

Appendix B: Maximum Pile Head Lateral Deflection Calculation

According to the report of Huang et al. (2004), the maximum temperature variation occurs on December 25th, 2000 at -40.6 °C. Based on the bridge total length (L) coefficient of thermal expansion (α) summarized in Section 4.2, the displacement at the end of the superstructure (ΔL) due to temperature variation equals:

$$\Delta L = 0.5 \times \Delta T \times \alpha \times L = (0.5)(40.6)(11.07 \times 10^{-6})(66000) = 14.8 \text{ mm} \quad [\text{A-1}]$$

Figure A-2 shows the measured strains of the superstructure measured at the slab and the top flange, web, and the bottom flange of an exterior girder at the end span (Huang et al. 2011). The abutment rotation can be estimated from these girder strains. On December 25th, 2000, the strains of the girder cross-section near the abutment are approximately -50 and -150 $\mu\epsilon$ at the top and bottom of girder flange, respectively, which corresponds to 1.1 and 3.3 mm. The locations of strain gauges measuring the strains in the top and bottom flange are shown in the figure in the bottom corner of Figure A-2. The distance between the two strain gauges is approximately 0.9 m. Assuming the abutment rotation is equal to the rotation of the girder at the end, the abutment rotation equals 0.0024 rad.

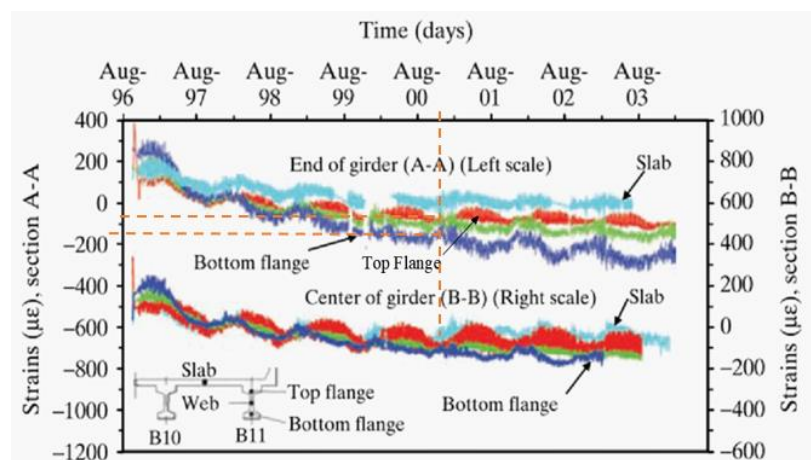


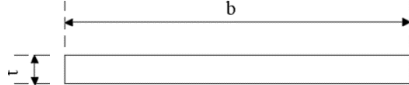
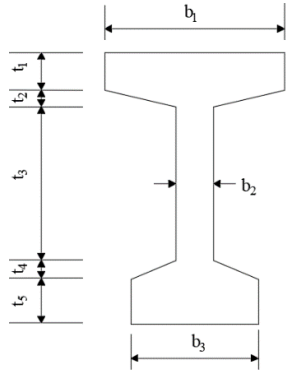
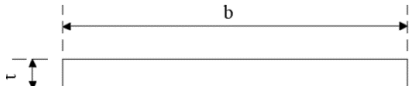
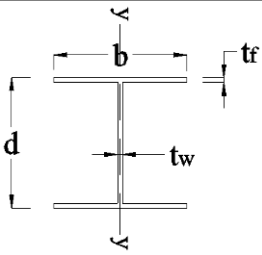
Figure A- 2: Measured Superstructure Strains (Huang et al. 2011)

From Figure 4-4, the abutment height is 3 m. Therefore, the lateral displacement at the bottom of the abutment or the pile head is approximately, 7.6 mm.

Appendix C: Member Sizes

Table A-1 listed the sizes used in the SAP 2000 models for both SAP 2000-LP and SAP2000-B analyses on Bridge #55555.

Table A - 1: Sizes of Structural Components in Bridge #55555

Structural Members	Dimensions	Sizes	Cross-Sections
Deck	b (mm)	12000	
	t (mm)	220	
	L (mm)	66000	
Type 45M Prestressed Girders	t_1 (mm)	160	
	t_2 (mm)	70	
	t_3 (mm)	650	
	t_4 (mm)	80	
	t_5 (mm)	190	
	b_1 (mm)	762	
	b_2 (mm)	160	
b_3 (mm)	660		
Abutments	b (mm)	12000	
	t (mm)	876	
	H (mm)	3000	
Abutment Piles	d (mm)	300	
	b (mm)	305	
	t_w (mm)	11	
	t_r (mm)	11	
	L (mm)	24400	

The steel reinforcement was ignored in this study because, based on numerical analyses, the influence of reinforcement on the bridge deformations, moments, and shear forces was less than 0.5%.

Appendix D: Calculation of Equivalent Loads of Temperature Gradient

This appendix shows a detailed calculation of the equivalent loads of the positive temperature gradient used in this study. As shown in Figure A-3, the temperature difference at different levels causes axial forces (F_i) and moments (M_i) about the neutral axis.

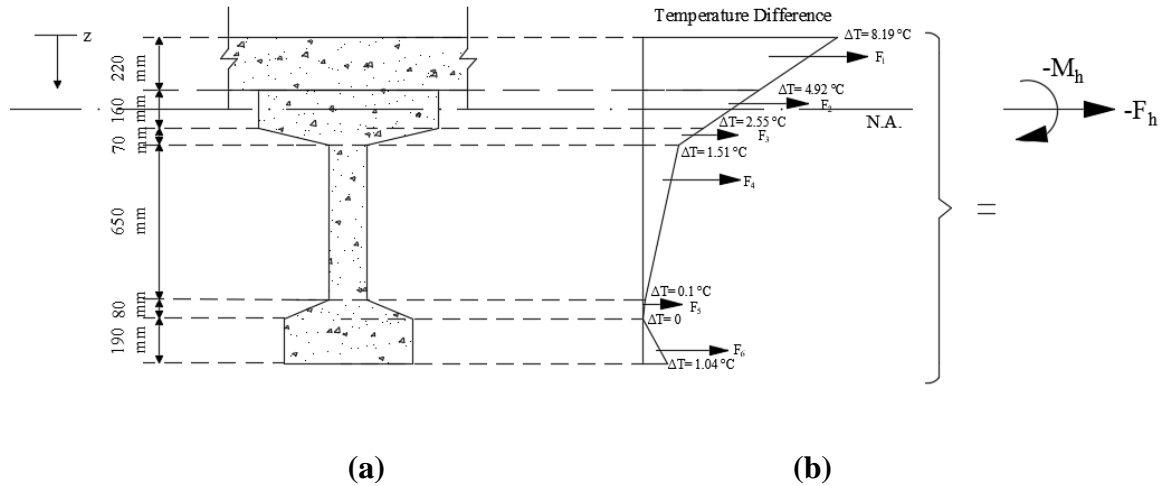


**Figure A- 3: (a) Partial Cross-Section of Bridge Superstructure;
(b) Positive Temperature Gradient and Equivalent Forces**

From Equation 4-3, the axial force (F) can be calculated as:

$$F_h = - \frac{\sum_{i=1}^6 b_{si} E_i \alpha_i (\Delta T_{top_i} + \Delta T_{bot_i}) h_i}{2} \quad [A-2]$$

where:

b_{si} is the cross-section width for segment i (m);

E_i is the Young's modulus for segment i (MPa);

α_i is the coefficient of thermal expansion of segment i ($\mu\epsilon / ^\circ\text{C}$);

ΔT_{top_i} is the temperature change at the top fiber of segment i ($^\circ\text{C}$);

ΔT_{bot_i} is the temperature change at the bottom fiber of segment i ($^\circ\text{C}$); and

h_i is the height of the cross-section of segment i (m).

Table A-2 listed the calculation of F_i for segment i:

Table A - 2: Calculations of F_i for Segment i

i	b_i (m)	E_i (MPa)	α_i ($\mu\epsilon / ^\circ\text{C}$)	h_i (m)	ΔT_{top_i} ($^\circ\text{C}$)	ΔT_{bot_i} ($^\circ\text{C}$)	F_i (kN)
1	12	30330	11.1	0.22	8.19	4.92	5810
2	3.05	34470	11.5	0.16	4.92	2.55	721
3	1.84	34470	11.5	0.07	2.55	1.51	104
4	0.64	34470	11.5	0.65	1.51	0.1	133
5	1.4	34470	11.5	0.08	0.1	0	2.22
6	2.12	34470	11.5	0.19	0	1.04	82.9
$F = -\sum_{i=1}^6 F_i = -6853 \text{ kN}$							

Therefore, F_h is approximately 6853 kN.

From Equation 4-4, the moment can be calculated as:

$$M_h = -\sum_{i=1}^6 F_i (Z_{t_i} - \bar{Z}_t) \quad [\text{A-3}]$$

where Z_{t_i} is the distance from the centroid of the temperature distribution of segment i to the top surface of the superstructure, and \bar{Z}_t is the distance from the centroid of the superstructure cross-section to the bottom surface of the superstructure.

The distance between from the centroid of the temperature distribution of segment i to the bottom surface of the superstructure for a segment with a trapezoidal temperature distribution can be calculated as:

$$Z_{t_i} = \frac{\Delta T_{\text{top}_i} + 2 \times \Delta T_{\text{bot}_i}}{3 \times (\Delta T_{\text{top}_i} + \Delta T_{\text{bot}_i})} h_i + Z_{t_{t_i}} \quad [\text{A-4}]$$

where $Z_{t_{t_i}}$ is the distance from the top of segment i to the top surface of the superstructure

Based on the calculations from SAP 2000, $\bar{Z}_t = 0.36$ m.

Table A-3 listed the calculations of M_i for segment i:

Table A - 3: Calculations of M_i for Segment i

i	F_i (kN)	Z_{t_i}(m)	$Z_{t_i} - \bar{Z}_t$ (m)	M_i (kN.m)
1	5810	0.101	-0.199	-1505
2	721	0.292	-0.008	-49.0
3	104	0.412	0.112	5.41
4	133	0.870	0.57	67.8
5	2.22	1.127	0.827	1.70
6	82.9	1.243	0.943	73.2
				$M_h = -\sum_{i=1}^6 M_i = 1406$ kN .m

Therefore, M_h is approximately 1406 kN.m.

Appendix E: Calculation of Earth Pressures

This appendix presents a detailed calculation of the magnitudes of earth pressures applied to the SAP 2000 models when the bridge expands or contracts. The calculations are based on the commentary of Canadian Highway Bridge Design Code (CSA 2019).

Highest Temperature on August 1st, 2001: $T_{high} = 45 \text{ }^\circ\text{C}$

Construction Temperature: $T_{const} = 12.78 \text{ }^\circ\text{C}$

Maximum Temperature Change (+ve): $\Delta T = 32.2 \text{ }^\circ\text{C}$

Total Span Length: 66 m

Thermal Coefficient of PC girder: $\alpha = 0.00001148 / ^\circ\text{C}$

Horizontal movement at each abutment by positive temperature change (ΔL_1):

$$\Delta L_1 = \Delta T L_s \alpha / 2 = 32.2 \times 66 \times 0.00001148 / 2 = 0.0122 \text{ m} = 12.2 \text{ mm}$$

where L_s is the total length of the bridge.

$$\text{Ratio of movement to abutment height: } \frac{\Delta L_1}{H} = \frac{0.0122 \text{ m}}{3 \text{ m}} = 0.00407$$

as shown in Figures A-4 and A-5, H is the full-height of the abutment (Figures A-4 and A-5).

Assume loose sand soil with at-rest coefficient $K_0 = 0.5$, the lateral earth pressure coefficient (K_p') is 1.15 based on the Figure A-4.

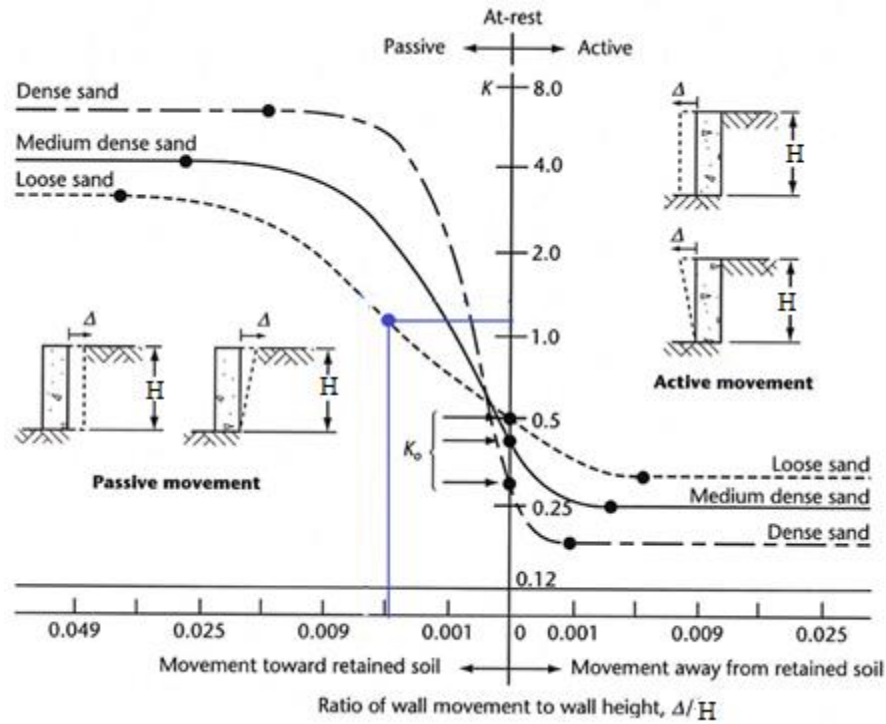


Figure A- 4: Lateral Earth Pressure Coefficients (after CSA 2019)

Therefore, as shown in Figure A-5, earth pressure force acting along the neutral axis of the superstructure when the bridge expands (P'_{p1}) is:

$$P'_{p1} = \gamma_s h_1 K'_p b_{abut} = 17.52 \times 0.36 \times 1.15 \times 12 = 87.0 \text{ kN} \quad [A-5]$$

where γ_s is the soil density, h_1 as shown in Figure A-5 is the distance between the top of the superstructure to the neutral axis of the superstructure, K'_p is the coefficient of the lateral earth pressure when bridge expands, and b_{abut} is the width of the abutment.

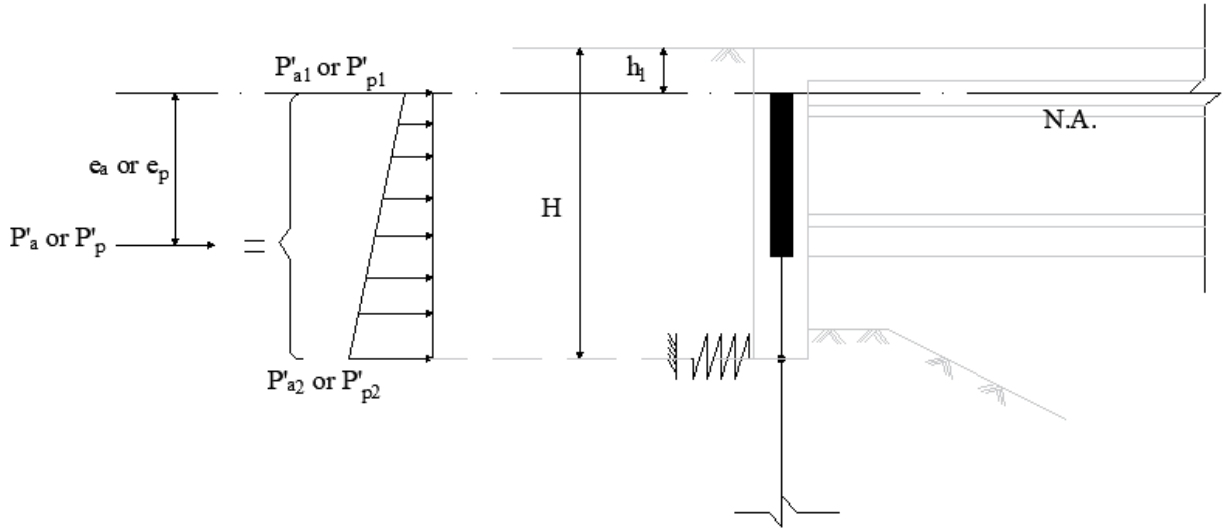


Figure A- 5: Illustration of Earth Pressure Idealization

The earth pressure at the bottom of the abutment when bridge expands (P'_{p2}) is:

$$P'_{p2} = \gamma_s H K_p 'b_{abut} = 17.52 \times 3 \times 1.15 \times 12 = 725 \text{ kN} \quad [\text{A-6}]$$

where H as shown in Figure A-5 is the full-height of the abutment from the top of the superstructure to the bottom of the abutment.

Therefore, the magnitude of the equivalent concentrated force P'_p equals:

$$P'_p = \frac{1}{2} (P'_{p1} + P'_{p2}) \times (H - h_1) = \frac{1}{2} (87 + 725) (3 - 0.36) = 1072 \text{ kN} \quad [\text{A-7}]$$

Since the equivalent concentrated force should provide the same moment as the linearly distributed load, the equivalent concentrated force should locate at the centroid of the trapezoidal linearly distributed load. Based on the geometry, the distance between the resultant force and the neutral axis (e_p) equals:

$$e_p = (H - h_1) - \frac{(H - h_1)(2P'_{p1} + P'_{p2})}{3(P'_{p1} + P'_{p2})} = 1.66 \text{ m} \quad [\text{A-8}]$$

Therefore, the earth pressure can be represented by a concentrated force with a magnitude of 1072 kN located at 1.67 m below the neutral axis of the superstructure.

Similarly, the earth pressure force acting along the neutral axis of the superstructure (P'_{a1}) and bottom (P'_{a2}) of the abutment when the bridge contracts are:

$$P'_{a1} = \gamma_s h_1 K_a' b_{abut} = 17.52 \times 0.36 \times 0.27 \times 12 = 20.5 \text{ kN} \quad [\text{A-9a}]$$

$$P'_{a2} = \gamma_s H K_a' b_{abut} = 17.52 \times 3 \times 0.27 \times 12 = 170 \text{ kN} \quad [\text{A-9b}]$$

where K_a' is the earth pressure coefficient when bridge contracts. Similar to K_p' , it is determined based on the ratio of movement to abutment height using Figure A-4.

The magnitude of the concentrated force P'_a equals:

$$P'_a = \frac{1}{2} (P'_{a1} + P'_{a2}) \times (H - h_1) = \frac{1}{2} (20.5 + 170) (3 - 0.36) = 251 \text{ kN} \quad [\text{A-10}]$$

Also, the distance between the location of the resultant force and the neutral axis (e) can be computed as:

$$e_a = (H - h_1) - \frac{(H - h_1)(2P'_{a1} + P'_{a2})}{3(P'_{a1} + P'_{a2})} = 1.67 \text{ m} \quad [\text{A-11}]$$

Appendix F: Sample Calculation of the Moments at Pile Head

Figure 4-15 shows the variation of the pile curvatures measured between August 1st, 1996 and August 1st, 2004 (Huang et al. 2011). The longitudinal pile curvature measured on August 1st, 2001 and December 25, 2000 are approximately 3.54 $\mu\epsilon/\text{mm}$ and 6.25 $\mu\epsilon/\text{mm}$, respectively.

Assuming the pile response as a Euler-Bernoulli beam, the moment at the pile head can be calculated based on the pile curvature (κ), the Young's modulus of the pile (E_p), and the moment of inertia of the pile cross-section (I_p). Hence, the moment at the pile head when the bridge expands (M_e) can be inferred from the measured pile curvature (κ_e) as:

$$M_e = \kappa_e E_p I_p = (3.54 \mu\epsilon/\text{mm})(200\text{GPa})(5.29 \times 10^7 \text{ mm}^4) = 37.5 \text{ kN.m} \quad [\text{A-12}]$$

Similarly, the moment at the pile head when the bridge contracts (M_c) can be inferred from the measured pile curvature (κ_c) as:

$$M_c = \kappa_c E_p I_p = (6.25 \mu\epsilon/\text{mm})(200\text{GPa})(5.29 \times 10^7 \text{ mm}^4) = 66.2 \text{ kN.m} \quad [\text{A-13}]$$

Appendix G: An Illustration of Instrumentations of Bridge #55555

Figure A-6 illustrates the locations of the instrumentations installed in Bridge #55555 (Huang et al. 2011). As shown in Detail A, the extensometer measuring the abutment movement was located at approximately 1.33 m above the bottom of the abutment.

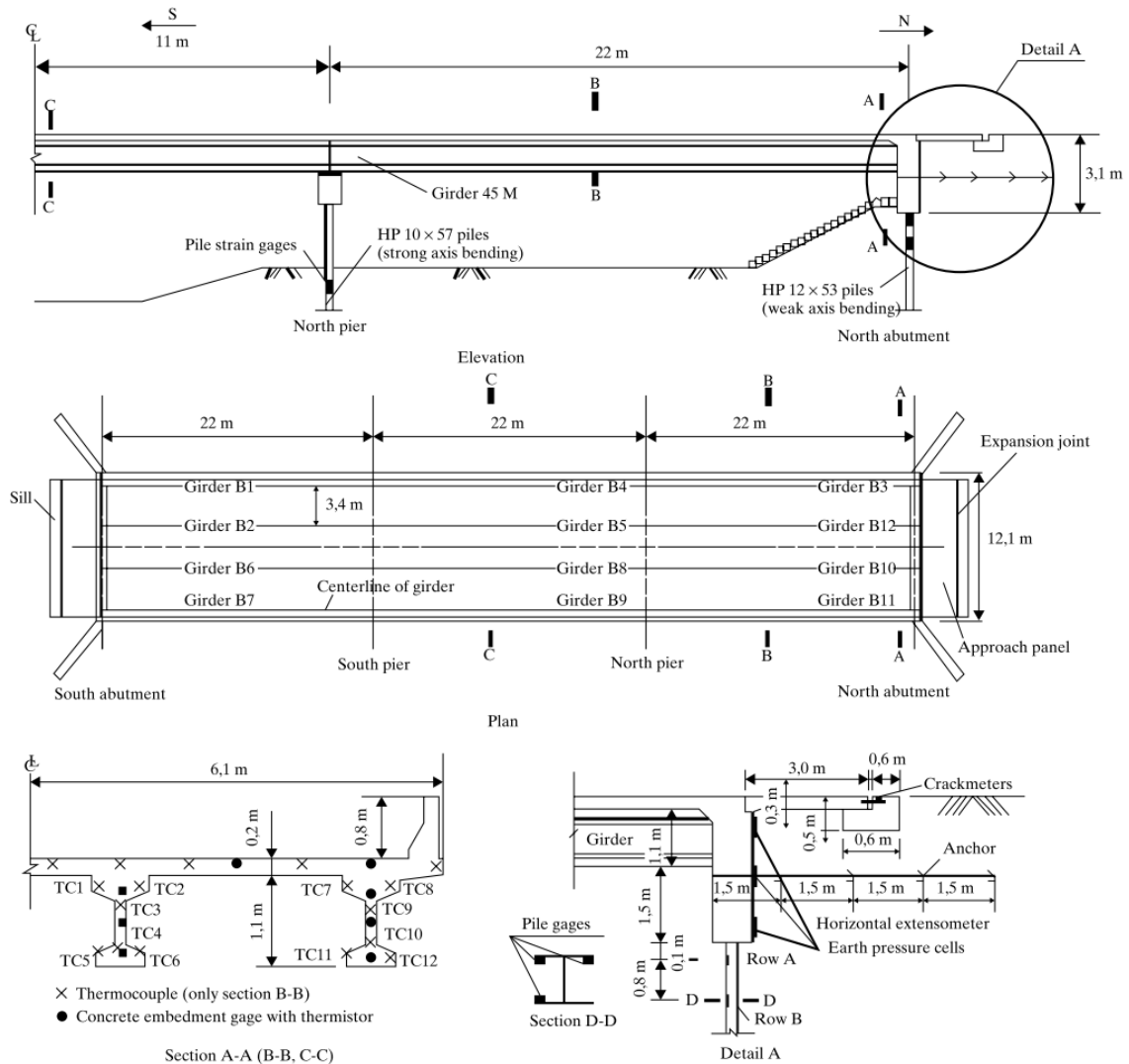


Figure A-6: Locations of the instrumentation (Huang et al. 2011)

Figure A-7 shows the nomenclature used to describe the instrumentation.

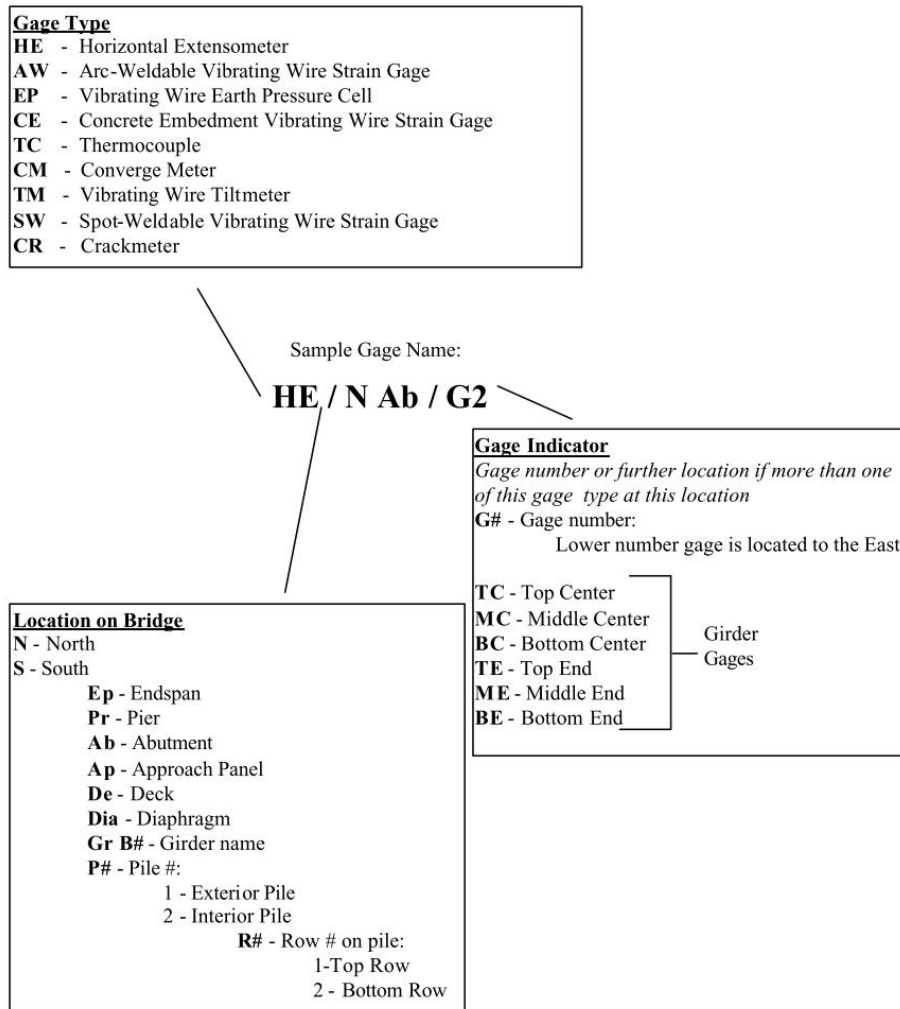


Figure A-7: Instrumentation Nomenclature System (Huang et al. 2011)

Appendix H: Bending Moment Diagrams of a Pile as Bridge Expands and Contracts

Figure A-8 shows the bending moment diagrams of a single pile when the bridge expands and contracts. The diagram was obtained from the corresponding LPILE model. As shown in the figure, the magnitude of the moment exceeds 78 kN.m in magnitude in the top 0.024 and 0.2 m of the pile as the bridge expands and contracts, respectively.

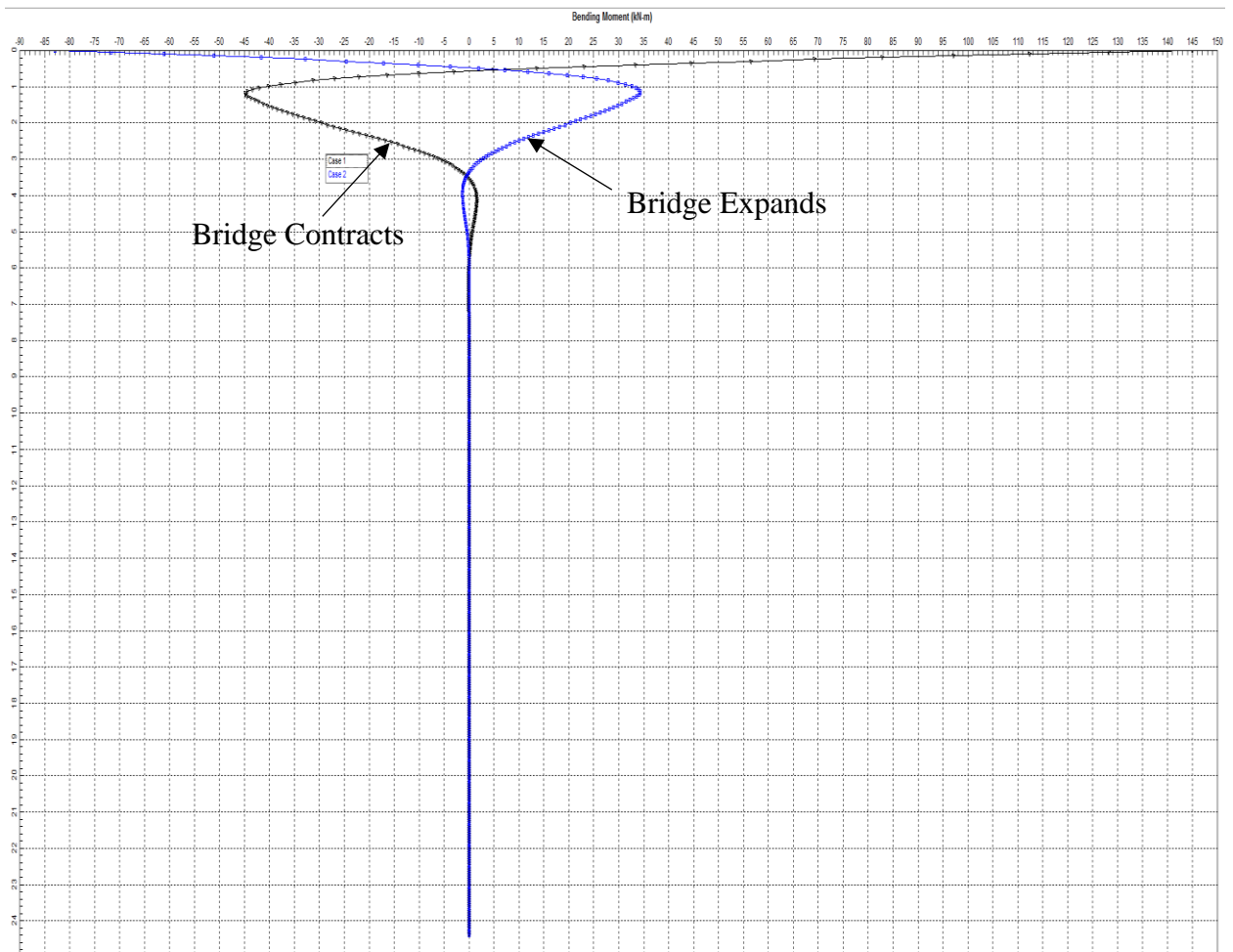


Figure A-8: Bending Moment Diagram of a Single Pile as Bridge Expands and Contracts

Appendix I: Validation of Equations 5-1 to 5-9b

Table A-4 (a) and (b) compare the deflections and force effects, respectively, obtained from Equations 5-1 to 5-9 with those obtained from the SAP-B analysis with the soil input parameters estimated using the B-relationship.

Table A-4(a): Comparison of Lateral Translations and Rotations for Cases 1 to 11

Case	SAP-B	Eq. 5-9(a)	SAP-B		Eq. 5-1
	Δ_p (mm)	Δ_p (mm)	Θ_s (rad)	Θ_p (rad)	Θ (rad)
1	4.8	4.9	0.00283	0.00301	0.00292
2	9.8	9.9	0.00480	0.00511	0.00527
3	6.7	6.8	0.00245	0.00216	0.00227
4	1.3	1.4	0.00233	0.00254	0.00248
5	-1.5	-1.3	0.00212	0.00192	0.00215
6	4.5	4.9	0.0030	0.00313	0.00299
7	5.2	5.3	0.0041	0.00291	0.00277
8	4.4	4.4	0.0030	0.00318	0.00307
9	3.0	3.0	0.0035	0.00367	0.00356
10	4.7	4.7	0.00291	0.00308	0.00295
11	2.7	2.7	0.00358	0.00377	0.00360

Table A-4(b): Comparison of Force Effects for Cases 1 to 11

Case	ΣM_p (kN.m)		ΣV_p (kN)		M_s (kN.m)		N_s (kN)	
	SAP-B	Eq. 5-7	SAP-B	Eq. 5-8	SAP-B	Eq. 5-6	SAP-B	Eq. 5-5
1	-453	-469	2013	2036	-7554	-7630	3086	3108
2	-1030	-1067	4240	4289	-14556	-14721	5640	5688
3	-906	-938	3144	3189	-10990	-11148	4216	4261
4	142	139	229	225	-6001	-6147	1929	1924
5	567	629	-1114	-1229	-5347	-4522	1968	1853
6	-372	-414	2244	2271	-7979	-8195	3338	3343
7	-444	-503	1967	2029	-7332	-7647	3061	3102
8	-421	-439	2273	2289	-8102	-8268	3366	3362
9	-298	-316	2875	2890	-9540	-9733	3968	3963
10	-468	-483	2142	2159	-7799	-7968	3232	3231
11	-230	-261	3018	3051	-9840	-10102	4110	4132

Appendix J: Maximum Stresses at Pile Head

Table A-5 summarizes the maximum stresses at the pile head, computed using the largest moment at the pile head from the SAP-LP and three SAP-B analyses. The axial forces are computed as the sum of the reaction at the end of the superstructure and the abutment weight, divided by the number of piles. The area of the pile cross section is 9800 mm² except for Case 7, when it increases to 14700 mm², and the elastic section modulus is 5.24×10⁷ mm⁴ except for Case 6, when it increases to 16.3×10⁷ mm⁴ and Case 7, when it increases to 23.7×10⁷. The “Maximum Moment Before Yield” is the moment that causes the stress in the extreme compression fibre to equal the yield stress, 250 MPa. The depth of the yielded region is determined using the pile head shear force, which reduces the pile moment below the pile head. The maximum depth of the yielded region is only 0.25 m for the 11 cases considered., Therefore, the equivalent secant rigidity of the pile is likely close to the product of the elastic modulus of steel and weak-axis moment of inertia and the assumption of linear-elastic pile stands.

Table A-5: Maximum Stresses at Pile Head

Case	Axial Force (kN)	Axial Stress (MPa)	Moment (kN.m)	Flexural Stress (MPa)	Total Stress (MPa)	Maximum Moment Before Yield (kN.m)	Depth of Yield Region (m)
1	-261	-26.8	-80.7	-231	-258	-78	0.024
2	-261	-26.8	-189	-542	-568	-78	0.22
3	-261	-26.8	-151	-432	-459	-78	0.25
4	-347	-35.6	16.6	-68	-103	-75	-
5	-428	-43.9	102	-291	-335	-72	0.20
6	-376	-25.6	-88.3	-81	-107	-78	-
7	-250	-27.0	-135	-86	-113	-78	-
8	-250	-25.6	-83.5	-239	-265	-78	0.021
9	-250	-25.6	-87.3	-250	-276	-78	0.018
10	-250	-25.6	-85.0	-243	-269	-78	0.021
11	-250	-25.6	-81.8	-234	-260	-78	0.018

Appendix K: Soil Properties and Young's Moduli for Cases 8 and 9

Tables A-6(a) and (b) summarizes the soil properties and Young's moduli used for the analyses of Cases 8 and 9, respectively.

Table A-6(a): Estimated Soil Poisson's Ratios and Young's moduli for Case 8 (Uniform Loose Sand)

Layer	Soil Type	Thickness (mm)	Depth Below Pile Head (m)	v_s'	k (MPa)	Υ' (kN/m ³)	σ'_v (kPa)	ϕ' (deg)	K_G (kPa)	E_s' (MPa)		
										B-	K-	L-
1	Loose Sand	6.10	3.05	0.2	75.9	17.5	107	30	313	101	71.3	63.4
2			9.14		152		214			188	135	89.6
3			15.2		228		320			271	197	110
4			21.3		304		427			352	257	127

Table A-6 (b): Estimated Soil Poisson's Ratios and Young's moduli for Case 9 (Uniform Dense Sand)

Layer	Soil Type	Thickness (mm)	Depth Below Pile Head (m)	v_s'	k (MPa)	Υ' (kN/m ³)	σ'_v (kPa)	ϕ' (deg)	K_G (kPa)	E_s' (MPa)		
										B-	K-	L-
1	Dense Sand	6.10	3.05	0.4	243	20	64.6	36	516	251	184	120
2			9.14		493		568			476	355	173
3			15.2		724		105			674	506	213
4			21.3		981		158			887	670	247

Appendix L: Consideration of the Water Table

Table A-7 summarizes the soil properties and Young's moduli for Case 8b where the soil is uniform sand with water table located at 5.55 m below the pile head. Compared to the values in Table A-6(a), including the water table reduces the soil Young's moduli for all four layers.

Table A-7: Estimated Soil Poisson's Ratios and Young's moduli for Case 8b (Uniform Loose Sand with Water Table)

Layer	Soil Type	Thickness (mm)	Depth Below Pile Head (m)	ν_s'	k (MPa)	γ' (kN/m ³)	σ'_v (kPa)	ϕ' (deg)	K_G (kPa)	E_s' (MPa)		
										B-	K-	L-
1	Loose Sand	5.5	2.75	0.2	75.9	17.5	107	30	313	96	68.1	61.8
2		6.3	8.65		152	7.5	214			167	120	81.8
3		6.3	15.0		228	7.5	320			251	182	92
4		6.3	21.3		304	7.5	427			239	173	101

Tables A-8 (a) and (b) summarize the displacements and rotations, respectively, at the pile head and at the end of the superstructure for Case 8, where the water table is neglected, and Case 8b, where the water table is considered. The deformations are the same between the two analyses.

Table A-8(a): Displacements at the Pile Head and at the End of the Superstructure Obtained from SAP 2000 Analyses for Cases 8 and 8b

Case	Δ_p (mm)				Δ_s (mm)			
	LP	B-	K-	L-	LP	B-	K-	L-
8	6.3	4.4	5.0	5.2	12.6	12.4	12.5	12.5
8b	6.3	4.4	5.0	5.2	12.6	12.4	12.5	12.5

Table A-8(b): Rotations at the Pile Head and the End of the Superstructure Obtained from SAP 2000 Analyses for Cases 8 and 8b

Case	Θ_p (rad)				Θ_s (rad)			
	LP	B-	K-	L-	LP	B-	K-	L-
8	0.0025	0.0032	0.0030	0.0029	0.0024	0.0030	0.0028	0.0027
8b	0.0025	0.0032	0.0030	0.0029	0.0024	0.0030	0.0028	0.0027

Tables A-9(a) and (b) summarize the load effects at the pile head and at the end of the superstructure, respectively, for Case 8, where the water table is neglected, and Case 8b, where the water table is considered. The maximum difference in the load effects between the two analyses is approximately 2.8% (M_p for SAP-B analysis (B-relationship)). This is likely because the pile lateral deflection below the water table is minimal, hence the reduction in the soil stiffness due to the consideration of the water table has negligible effect on the pile and bridge response. Therefore, for simplicity, the water table is neglected in Cases 8-11.

Table A-9(a): Moments and Shear Forces at the Head of Each Pile Obtained from SAP 2000 Analyses for Cases 8 and 8b

Case	M_p per pile (kN.m/pile)				V_p per pile (kN/pile)			
	LP	B-	K-	L-	LP	B-	K-	L-
8	-83.5	-70.2	-76.8	-75.2	232	379	336	321
8b	-83.5	-68.2	-74.3	-74.3	232	379	336	322

**Table A-9 (b): Moments and Axial Forces at the End of the Superstructure
Obtained from SAP 2000 Cases 8 and 8b**

Case	M _s (kN.m)				N _s (kN)			
	LP	B-	K-	L-	LP	B-	K-	L-
8	-5964	-8102	-7479	-7251	-2464	-3366	-3111	-3026
8b	-5969	-8089	-7466	-7235	-2466	-3366	-3111	-3022

Appendix M: Soil Properties and Young's Moduli for Cases 10 and 11

Tables A-10(a) and (b) summarize the soil properties and Young's moduli used for the analyses of Cases 10 and 11, respectively.

Table A-10: (a): Estimated Soil Poisson's Ratios and Young's moduli for Case 10 (Sleeve Filled with Loose Sand)

Layer	Soil Type	Thickness (mm)	Depth Below Pile Head (m)	v_s'	k (MPa)	γ' (kN/m ³)	σ'_v (kPa)	ϕ' (deg)	K_G (kPa)	E_s' (MPa)		
										B-	K-	L-
1	Loose Sand	3	1.50	0.2	61.0	15	79.7	30	313	82.6	58.3	53.4
2	Medium to Dense Sand	3.46	4.73	0.2	111	15.43	133	31	313	141	101	68.1
3	Dense Sand	18.0	15.4	0.35	730	10.30	259	37	516	709	531	168

Table A-10 (b): Estimated Soil Poisson's Ratios and Young's moduli for Case 11 (Sleeve Filled with Dense Sand)

Layer	Soil Type	Thickness (mm)	Depth Below Pile Head (m)	v_s'	k (MPa)	γ' (kN/m ³)	σ'_v (kPa)	ϕ' (deg)	K_G (kPa)	E_s' (MPa)		
										B-	K-	L-
1	Dense Sand	3	1.50	0.4	370	22	83.4	40	516	368	272	102
2	Medium to Dense Sand	3.46	4.73	0.2	119	15.43	140	31	313	151	108	73.6
3	Dense Sand	18.0	15.4	0.35	899	10.30	259	37	516	856	643	176

Curriculum Vitae

Name: Biyi (Lindsey) Li

Post-secondary Education and Degrees: University of Alberta
Edmonton, Alberta, Canada
2013-2018 B.Sc

Western University
London, Ontario, Canada
2018-2020 M.E.Sc

Related Work Experience Teaching Assistant
Western University
2019-2020

Publications:

Li, B., Bartlett, F. M., Newson, T. (2021). Integral Abutment Bridges: Modelling and Predictive Approaches for Temperature Movements. Proceedings of the 2021 CSCE Annual Conference, Niagara Falls, Ontario, Canada.